Enhanced Crystallization of Amorphous Silicon Thin Films by Nano-crystallite Seeding

A DISSERTATION
SUBMITTED TO THE FACULTY OF THE GRADUATE SCHOOL
OF THE UNIVERSITY OF MINNESOTA
BY

Jason Trask

IN PARTIAL FULFILLMENT OF THE REQUIREMENTS
FOR THE DEGREE OF
Doctor of Philosophy

Prof. Uwe Kortshagen

December, 2013

Acknowledgements

I owe the department of mechanical engineering at the University of Minnesota a tremendous debt of gratitude, for the Bachelor's degree they granted me in 2005, the friends I acquired along the way through agonizingly long nights in the computer lab, and the job opportunity that it afforded after graduation. I also owe the department for agreeing to take me back for a graduate tour of duty after I contracted a severe case of apathy for that job in 2007.

I decided to go back to graduate school for a Master's degree for what I had thought would just be two years. Six years later I left after completing this third and final revision of the document you now hold in your hands. A document which you are about to either a) selectively skim (in which case I must thank you -again- for agreeing to be on my committee) b) put back on the shelves of Walter library after glancing at a few figures, which I can't blame you for (FYI the ones in chapter 6 are the prettiest; they're fancy microscope images of crystals), or c) put back on the shelves in Eckert library and get back to grading final exams after an instructor-purchased lunch.

If by some chance you are the lucky successor to the project this document was concerned with, and if I am still alive at the time of your reading this, feel free to contact me by any means necessary and I'll be happy to trouble-shoot apparatus issues with you. Specifically, I'll let you know exactly the size of blunt object needed, and where to hit said apparatus. If that doesn't manage to solve the problem, relying on the skill of the brilliant minds around you is the best route. I surely couldn't have survived without the assistance of colleagues such as David Rowe, Lee Weinkes, Rick Liptak, Curtis Anderson, Rebecca Anthony, Andrew Wagner, Ariel Chatman, Lin Cui, Jeslin Wu, Ting Chen, and Brian Merritt.

In regards to non-equipment based support, including data analysis, assessing the

sanity of a hypothesis, or just navigating the psychological rollercoaster that is the graduate experience, your fellow graduate students and staff are the most valuable resource there is. For this, in addition to those previously mentioned, I must also thank Benjamin Adams, Derek Obereit, Ranganathan Gopalakrishnan, Barry Mutlu, Adam Boise, Lance Wheeler, Vince Wheeler, Daniel Rave, Dominic Triana, Geek Cinema, The Velvet Rope Club, Luke Franklin and the GENS network, and last but certainly not least, the grad-father himself John Gardner. If he's still working in the department at the time of your reading this, make sure to pay your respects.

From a much needed happy hour after a rough group meeting, to 1 a.m. meals at the village wok while waiting for an experiment to finish, to 3 a.m. meals at a conference in a strange city, if there's anything graduate research will teach you, it's that the people you meet along the way, in the moments between data sets, are by far and away the most significant variables in the entire parameter space. So make sure to leave the lab from time to time, and keep your coffee mug full, because even a sleepless grad-student can still dream.

Dedication

To Randall Trask, a good man that I was fortunate enough to know as a father. And to his grandfather Everett Cincoski: a true engineer if there ever was one.

Abstract

Polycrystalline silicon (poly-Si) has become popular in recent years as a candidate for low cost, high efficiency thin film solar cells. The possibility to combine the stability against light degradation and electronic properties approaching melt-grown, wafer-based crystallline silicon, with the cost advantage of Silicon thin films is highly attractive. To fully realize this goal, efforts have been focused on maximizing grain size while reducing the thermal input involved in a critical "annealing" step. Of the variety of processes involved in this effort, studies have shown that poly-Si films obtained from solid-phase-crystallization (SPC) of hydrogenated amorphous silicon (a-Si:H), grown from non-thermal plasma-enhanced chemical vapor deposition (PECVD), exhibit the potential to achieve the highest quality grain structures. However, reproducible control of grain size has proven difficult, with larger grains typically requiring longer annealing times.

In this work, a novel technique is demonstrated for more effectively controlling the final grain structure of SPC-processed films while simultaneously reducing annealing times. The process utilized involves SPC of a-Si:H thin films containing embedded nanocrystallites, intended to serve as predetermined grain-growth sites, or grain-growth "seeds", during the annealing process. Films were produced by PECVD with a system in which two plasmas were operated to produce crystallites and amorphous films separately. This approach allows crystallite synthesis conditions to be tuned independently from a-Si:H film synthesis conditions, providing a large parameter space available for process optimization, including the effects of particle size, shape, quantity, and location within the film.

The work contained here-in outlines the effects of select parameters on the both grain size control and thermal budget. Reproducible control of both grain size and crystallization rate were demonstrated through varying initial seed crystal concentrations. Significant reductions in annealing times were demonstrated to occur in seeded films relative to unseeded films, with both seed crystal concentration and seed crystal geometry demonstrating significant effects on crystallization rate. Furthermore, the development of this technique has resulted in potentially new insights on the material system involved, with the observation of a potentially unique phase-transformation mechanism.

Contents

List of Tables

List of Figures

Chapter 1

Introduction

The work contained herein consists of a collection of studies on a material with potential uses in photo-voltaic energy conversion. Specifically, these studies focus on semiconducting silicon-based films that are poly-crystalline in structure with thicknesses less than one micron. Similar materials have already been studied extensively elsewhere, for this intended purpose. However, the following body of work presents a relatively novel processing technique with measurable advantages over traditional techniques. Furthermore, the development of this technique has resulted in potentially new observations on the material system involved. Chapters 2 and 3 describe the context for application and the basic experimental techniques used in material processing. Chapters 4-7 each demonstrate the effect of varying a different key processing component on the behavior of the material system. The effects of each of these components on synthesis and performance are identified.

- **Chapter 2** provides the context and intended application of the material system that is the focus of this work: poly-crystalline silicon (poly-Si) thin films. The chapter begins with a brief summary of the global energy landscape, followed by the motivation for progress in photo-voltaics. It proceeds to a brief synopsis of the most relevant photo-voltaic technologies to date, and the challenges faced by each in achieving large-scale viability. A more extensive synopsis is given of poly-Si thin film technologies; specifically common crystal growth techniques. The chapter concludes with a brief outline of the poly-Si synthesis process used in this work, and the potential it has for solving the challenges faced by current methods.

- **Chapter 3** outlines the apparatus and techniques used in synthesis of poly-Si thin films in this work, and it explains the novel aspects. The chapter also outlines basic processing parameters and relevant properties of the materials synthesized. These parameters are compared to common parameters found in industry and literature.
- **Chapter 4** analyzes the effect of varying annealing temperature on the basic crystallization behavior of the proposed material system. Comparisons are made to traditional material systems, and advantages are outlined. The underlying thermodynamics and kinetics of the crystallization process are also characterized.
- **Chapter 5** demonstrates the effect of varying a parameter that will be defined as "seed crystal density". Three primary film properties will be characterized as a result of varying seed density; crystallization rate, film disorder, and final grain structure.
- **Chapter 6** demonstrates the effect of varying seed crystal shape on crystallization rate. Synthesis conditions are also outlined for which a potentially novel phase transformation mechanism occurs. The additional processing advantages of these conditions are quantified.
- **Chapter 7** demonstrates the effect of varying amorphous film deposition properties. Specifically, a parameter space is studied in which relatively higher deposition rates are achieved. Several significant film parameters are observed to change concurrently, and their effects on crystallization rate are measured. An optimal processing window is identified.
- **Chapter 8** summarizes the main conclusions of each study, and quantitatively compares the performance of the processing technique used with those found in industry and literature.

Chapter 2

Background

2.1 The Current Energy Landscape

One of the most formidable challenges currently facing the globe is that of securing a sustainable energy supply. Aside from the potential environmental detriments, the current global energy infrastructure operates primarily on resources of increasingly limited supply. As of 2009, total world energy consumption reached approximately 17 Terawatt-years ($TWyr$) [1] with over 85% of this demand being satisfied by oil, coal, natural gas, and nuclear energy resources. Surveys covering the same year estimate there to be approximately 3000 $TWyr$ combined of remaining supply of these four main resources [2]. Greater than half of this remaining supply either consists of more environmentally detrimental versions of currently used forms, exists in locations requiring more complicated acquisition processes, or requires technologies not yet developed enough to make acquisition economically viable. With global consumption projected to rise to approximately 23 $TWyr$ by 2030 [2], excluding acquisition difficulties, these estimates forecast a diminishing amount of usable energy with the current hierarchy of usage and available technologies.

2.2 The Potential Role of Solar Energy

It is interesting to note that if we were to use up every last joule of the estimated remaining 3000 TWyr of these four primary resources, we would have used the energy equivalent of the sun hitting the earth over the course of approximately nine days. The amount of sunlight arriving at the earths surface in one hour is enough to satisfy global energy needs for an entire year. In fact, the combined surface area of roads paved by humankind in the last 100 years, if covered in photo-voltaic (PV) panels at current efficiencies, could provide enough energy to supply a global population of 10 billion [3]. With this magnitude of available renewable resource it is evident that solar energy has tremendous potential to rectify the looming energy challenge.

Currently, solar energy provides less than 1% of the total resources used to satisfy global energy demands due to the inability of traditional solar cell technologies to be cost competitive with a primarily coal dominated electricity market [4]. In order to compete with current utility sources, new PV technologies must be able to consistently produce modules that can operate at peak performance for under $\$1/W$. Achievement of this goal demands lower manufacturing costs, higher stable efficiency, and higher process yields than current standards. Furthermore, due to the large scale of material resources required, such solar cells must consist of readily abundant and non-harmful components.

It is easy to understand then why over 80% of annual PV module production continues to be dominated by silicon based technologies [5]. Silicon, being the second most abundant element in the earths crust, is also non-toxic, has electronic properties suitable for photo-voltaic conversion, and has already been extensively studied and developed for industrial application, due to its central role in the integrated circuit industry.

2.3 The Current Industry Leader: Wafer-based Technologies

Within the global solar market, as of 2012, over 89% of PV technologies consist of what is known as crystalline silicon (c-Si) based modules [6]. c-Si modules have relatively high stable efficiencies due to the exceptional electronic transport that a material with a large-grain crystal structure provides. However, the process required to consistently reproduce high purity materials of this nature is relatively costly and energy intensive. Most c-Si technologies involve very high temperatures (greater than 1400 °C), and highly sensitive procedures to generate large single crystal or multi-crystalline “ingots” that crystal wafers are cut from. These processing parameters are cost effective for a microelectronics industry in which several hundred high-value processor chips can be made per wafer. However, a complete photo-voltaic system requires several full wafers in order to generate a viable quantity of electricity in even the smallest-scale applications.

Material waste is also significant in most c-Si processes, as most wafers must be cut to thicknesses several times larger than is needed for device performance due to their brittle and fragile structure. Taking into consideration that over half of the usable material is lost in the wafer sawing process, it is easy to see how a substantial part (40% to 50%) of c-Si module costs typically arise from wafer production [7,8]. Furthermore, since wafers can only be successfully manufactured with limited surface area sizes (typically less than 450 mm in diameter), scaling up to large area devices requires additional processes to link cells together in order to produce a viable module. Despite the numerous difficulties with wafer production, these melt-grown, c-Si based modules comprise a majority of the global PV market. However, cost improvements are relatively limited, due to the fact that these processes are cost-optimized primarily for much more developed, non-solar industries. In order for photo-voltaics to occupy a significant portion of the global energy demand, new processes, catered specifically to photo-voltaic cost optimization, must be explored.

2.4 Second Generation Solar Cells: Thin Film Technologies

2.4.1 Advantages

In recent decades, due to advances in nanometer-scale characterization and manufacturing, a new paradigm of "thin-film" technologies has emerged, which shows tremendous promise for providing significant cost reductions over current c-Si standards. Unlike the high temperature melting used in wafer processing, thin films are typically synthesized from semiconductors contained in the gas phase, with processes rarely exceeding temperatures of 600 °C. The primary performance advantage of thin film processing, aside from a significantly reduced material requirement, is that these thinner cells require photo-generated carriers to travel much smaller distances in order to be collected. Since longer distances increase the probability of a carrier being lost to defects within the material, thinner cells are not required to have the same high level of purification, which is one of the largest expenses in c-Si processing [7].

A more significant industrial advantage of thin film manufacturing is the ability to deposit material uniformly over much larger areas. This allows for the manufacture of full-sized modules directly rather than having to process, cut, and connect individual wafers into modules as with traditional c-Si based processes. Furthermore, the lower temperatures offered by these techniques are conducive to fabrication on a variety of inexpensive substrates, and thus are more amenable to large-scale integration with common building materials.

2.4.2 Challenges

The main disadvantage of thin film materials stems from the large number of structural defects they contain relative to c-Si technologies. Structurally, they are either polycrystalline/microcrystalline (composed of several different crystalline regions of various orientation) or amorphous (having no long-range atomic order). As such, they contain defects such as grain boundaries, strained or broken bonds, and atomic vacancies. These defects substantially lower device efficiency by hindering electronic transport [9–12].

Furthermore, although the dramatically reduced processing costs make thin films more effective in cost/Watt (essentially cost/panel) terms, the lower efficiencies they exhibit require more panel surface area to achieve the same total power output as a c-Si system. This subsequently increases installation and other external or “base-of-system” (BOS) costs, which generally scale with system sizes. Much of the difficulties associated with optimizing thin film quality results from the technology’s youth. Whereas the c-Si PV industry inherited a significant knowledge-base from the mature microprocessor industry, thin film material processing is still relatively young, leaving much to be optimized.

The fundamental challenge of thin film PV technologies is to combine the efficiency and stability of c-Si wafer-based materials, with the cost advantage of thin film materials. Although this goal has yet to be realized to the extent necessary, tremendous work toward this effort has ushered in what has arguably become a thin film era for the PV industry. From 2003 to 2008 alone, thin film global market share nearly doubled from 7% to 13%, and is expected to experience continued growth; putting it on track to increase from a market worth of $44 billion in 2017, to $1 trillion by 2021 [13].

2.4.3 Current Thin Film Market Leaders: Cadmium Telluride and Copper Indium di-Selenide

Of the five primary constituents of this market, the highest performing technologies with stable module efficiencies above 10% and module costs below $\$1/W$, are currently comprised of cadmium telluride (CdTe), or copper indium diselenide (CIS) based materials [14–16]. Although these two materials combined currently occupy a significant share of the thin film market, with efficiencies climbing at a steady pace, there are justified concerns about their ability to meet all of the criteria necessary for a long term solar solution. CIS devices have not only exhibited significant difficulties in uniform process scaling, but rely on the increasingly scarce elements Indium and Selenium, which originate primarily as minor byproducts of other, expensive, rare-earth metal productions [9, 16]. CdTe devices suffer from similar resource limitations with tellurium, as well as additional concerns regarding the high toxicity of cadmium. For these reasons, great efforts in recent years have been put toward developing silicon-based thin films that can compete with CdTe, CIS, and eventually c-Si performance.

2.5 The Primary Alternatives: Silicon Thin Film Technologies

2.5.1 Amorphous Silicon Thin Films

The earliest example of thin film technology, and possibly the most heavily studied, has been hydrogenated amorphous silicon (a-Si:H). Having been successfully deposited using a plasma discharge for the first time over 45 years ago [17], a-Si:H has been extensively characterized and used within several areas of the micro-electronics industry, mainly for its relatively simple deposition and easily doped electronic structure [18, 19]. Although several alternative deposition methods have emerged in the last few decades, including hot-wire deposition [20, 21] and electron-beam evaporation [22–24], a-Si:H is still overwhelmingly grown from plasma dissociation of a silicon containing gas, silane, in a method known as plasma enhanced chemical vapor deposition (PECVD). This is due to the fact that PECVD processes lend themselves more easily to larger area depositions with fewer issues regarding uniformity and equipment scaling. Furthermore, PECVD a-Si:H films can be reproducibly deposited at thicknesses well below 1 μm and at temperatures amenable to inexpensive substrates [7, 25, 26].

Although these exceptional cost advantages have made a-Si:H the global leader in the thin film solar cell market in years past, its progress has recently begun to plateau. This is due mainly to the inherent disorder of the amorphous bond structure, which contains a significantly larger number of strained or broken bonds relative to c-Si materials. These defects result in sub-bandgap energy states that act as recombination centers for charge carriers [25]. For this reason a-Si:H based devices exhibit much poorer electronic transport than its microcrystalline and polycrystalline counterparts [26–28]. Furthermore, these properties degrade even further under extended light exposure, due to a phenomenon known as the Staebler Wronski Effect (SWE) [10, 29, 30]. With the exception of a few recent efforts utilizing novel light-trapping schemes, little progress has been made to prevent this degradation. Subsequently, the average stabilized efficiency [1] for single-junction a-Si:H based production modules has stayed below 7%. [7, 15].

---

[1] Stabilized efficiency refers to the efficiency measured under light exposure, after the observed degradation with time has plateaued

2.5.2 Mixed-phase Silicon Thin Films

Recent efforts in silicon thin films have thus been focused on developing materials that negotiate a middle-ground between the manufacturing simplicity of amorphous silicon and the performance and stability of crystalline silicon. This has led to the study of several "mixed-phase" materials consisting of various combinations of amorphous and crystalline silicon regions. These films are classified primarily by average grain size and volume fraction of the crystalline phase present. Materials commmonly referred to as either proto-crystalline, poly-morphous (pm-Si:H) or nano-crystalline (nc-Si:H) consist of a predominantly amorphous structure containing a disperse population of nano-scale crystalline grains. Devices based on these materials have been shown to exhibit novel transport behavior and enhanced stability over traditional a-Si:H devices [10, 27, 31–35]. Materials such as micro-crystalline silicon (μc-Si:H) consist predominantly of crystalline-phase material tightly spaced in grains several tens of nm in diameter. These materials have shown promising results when layered with traditional amorphous films to make tandem "micro-morph" devices [11, 36–40]. A phase diagram illustrating each material is shown in figure 2.1 below.

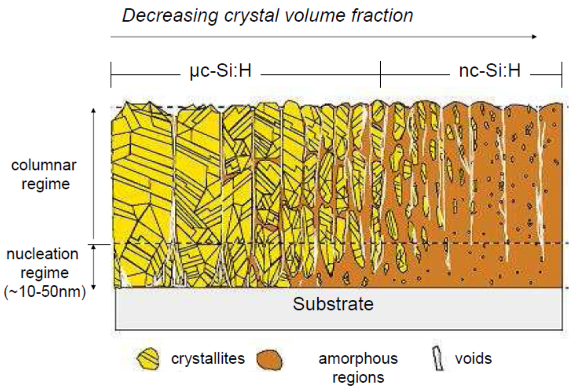

Figure 2.1: Phase diagram illustrating the various amorphous and crystalline contributions associated with mixed-phase silicon thin films. The progression of film growth beyond the nucleation layer illustrates the columnar growth typical of many mixed films; each column being separated by porous, defect rich regions. [41]

These materials have provided interesting and cost-effective improvements over traditional a-Si:H films, with several companies reporting stabilized efficiencies above 10% for factory-scale, multi-junction modules [7, 40, 42]. However, with deposition of mixed-phase layers, complications with scaling often result due to difficulties with maintaining precise phase proportions and uniformity over large thicknesses and areas [10, 43]. Furthermore, additional complications arise in multi-junction devices due to issues with current matching between layers of different phase [7]. Furthermore, the limited grain sizes and defects that remain in the more disordered film regions nc-Si:H and μc-Si:H provide limited room for further progress [7, 11, 44].

2.5.3 Poly-crystalline Silicon: The material system of study in this work

One of the more promising materials investigated in recent years is poly-crystalline silicon (poly-Si). Similar to the structural characteristics of CdTe and CIS materials, poly-Si films are comprised of a network of crystal grains much larger than nc-Si:H and μc-Si:H films, typically on the order of 1 μm to 100 μm (figure 2.2). These grains form naturally when a-Si:H films are heated at temperatures above 550 °C for extended periods of time in an annealing process step referred to as "solid-phase crystallization" (SPC) [45–47]. The resulting film structure has superior electronic transport and stability relative to amorphous and mixed-phase materials, with the same scalable processing as traditional a-Si:H PECVD [26, 48].

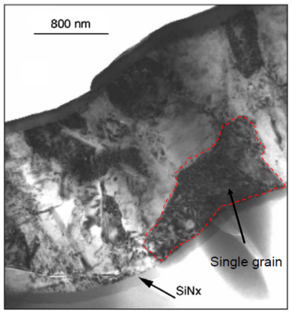

Figure 2.2: Cross-sectional TEM image of a poly-Si film after completion of annealing. An example of a singular grain is outlined in red [49].

Recent results include a device based on SPC of a 2.2 μm thick a-Si:H film capable of achieving a stable efficiency over 10% in large-scale, 600 cm^2, pilot line modules with an average cost near \$1.50/W [50, 51]. Furthermore, since the thin film poly-Si market is relatively new, there is still much opportunity for improvement on both material processing and device performance fronts.

Solid Phase Crystallization

In the area of process improvement, one of the primary costs arises from the thermal budget associated with the annealing step, which is carried out at temperatures between 550 °C to 1000 °C for periods of time ranging between 3 hrs to 70 hrs [45–47, 52, 53]. In this process step, the actual emergence of crystal grain growth is usually preceded by a time interval known as the incubation period. This period is attributed to the time required for hydrogen to effuse from the film, and highly strained Si-Si bonds to restructure [54].

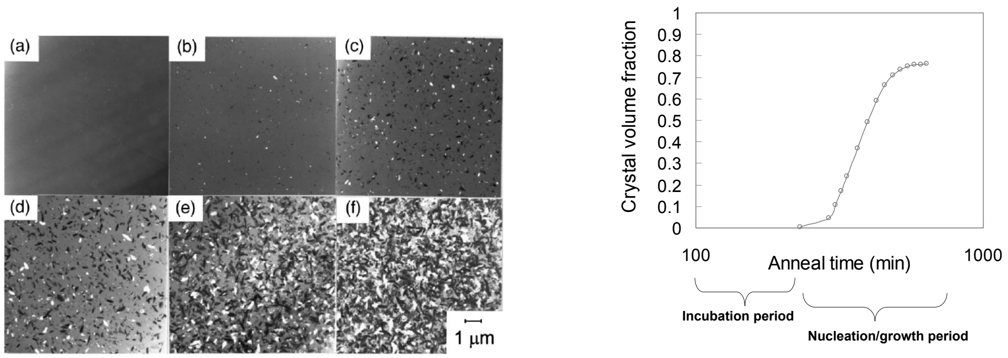

(a)

(b)

Figure 2.3: (a) TEM images showing the evolution of native nucleation during annealing of an amorphous silicon film [46]. (b) Typical plot depiction of the primary stages of crystal growth in an amorphous film during annealing. Crystal growth typically plateaus at volume fractions below 1 due to the small fraction of remaining non-crystalline material that constitutes the grain boundary regions.

Following the incubation period, the amorphous to crystalline phase transformation is believed to follow a classical nucleation model [45,46], wherein the formation or "native nucleation" of crystalline regions occurs after sufficient energy is available to generate crystalline clusters of a stable size. Following a brief transient period, crystallites will then emerge at a constant "nucleation rate" and grain growth proceeds, irreversibly, until grains coalesce as shown in figure 2.3.

Grain Size Effects

At the conclusion of an SPC process, the final film structure is comprised of multiple crystal grains of various orientations with interfaces or grain boundaries comprised of strained or broken bonds. These defects are the primary cause for reduced electronic performances of poly-Si devices relative to c-Si counterparts [55–58]. The PV performance parameter most heavily reflective of grain structure quality is referred to as the "open circuit voltage" (V_{oc}). V_{oc} is defined as the maximum voltage that a solar cell is capable of acquiring across its thickness under conditions of zero current flow. It is clear from figure 2.4 that V_{oc} exhibits the strongest grain size dependence within the 1 μm to 1 mm grain size regime (dotted line). It is worth noting that this regime -specifically the closed circle data- represents devices having thicknesses beyond typical thin film classification; ranging from 30 μm to 500 μm or more. Furthermore, they are deposited by relatively high temperature processes such as zone melting and epitaxy and are therefore incompatible with inexpensive substrates such as glass. Subsequently, these processes typically require more costly, higher melting point, alumina and graphite composite substrates [26, 48]. As a result, many of these technologies have yet to see developments beyond laboratory stages.

It is interesting to note that several thinner devices ($< 12\mu m$) such as the "CSG" and "Sanyo" devices, in the 1 μm grain regime, exhibit open circuit voltages similar to those obtained by the thicker, high-temperature processed devices in the millimeter grain size regime. Since the power output in a thin film device depends largely on the ability of light generated charge carriers to reach circuit-connected contacts on the front and back surfaces, the main goal of grain engineering is to achieve grains consistently as thick as the device. An example of this optimal grain structure is shown in figure 2.4b, where a cross-sectional TEM image of the Sanyo cell is shown to exhibit single grains extending through its entire 5 μm device thickness. It should be noted that both CSG and Sanyo devices were produced from 600 °C SPC of a-Si:H films having thicknesses below 5 μm. Although CSG devices remain in production, Sanyo has discontinued the development of this particular device due to the excessive annealing times (10hrs at 600 °C) required by its SPC process.

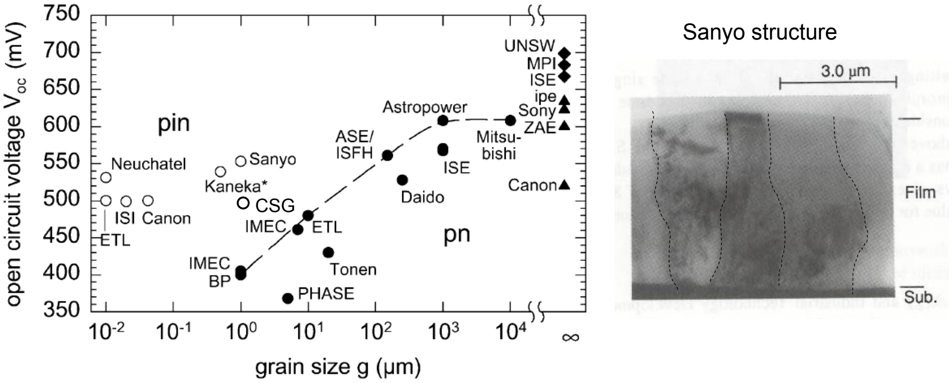

(a) (b)

Figure 2.4: (a) Open circuit voltages (V_{oc}) of crystalline Si thin film solar cells shown as a function of grain size "g". For poly-Si pn junction thin film cells 30 μm to 500 μm thick (solid circles), V_{oc} increases with grain size for 1 μm to 1 mm, and saturates for $g > 1$ mm (dashed line). Devices < 12 μm thick are shown in open circles. Figure and caption descriptions taken from [59], adapted to include CSG data from [26]. (b) Cross-sectional TEM image of the absorber layer used by Sanyo in the cell compared in a). Individual grains are outlined in black, and extend from substrate to film surface. [60].

The Fundamental Challenges of Solid-phase Crystallization

Subsequently, efforts in poly-Si film development have been focused on both increasing grain sizes while reducing required annealing times. However, numerous studies have found these outcomes to be mutually exclusive. Specifically, increasing grain size entails suppressing the rate of grain nucleation rate during SPC. Several studies have been able to successfully suppress nucleation rate through adjusting deposition conditions to increase hydrogen content and/or disorder within films. However, due to the incubation period required for film re-ordering prior to nucleation onset, this also typically results in a longer annealing time [20,45,46,52,54,61–67]. Since an increased incubation period begets additional annealing time and thus processing costs, more unique avenues of grain growth control must be explored in order make significant improvements to both film quality and process cost.

Externally Induced Grain Growth

To date, new efforts to improve these areas have focused on de-coupling film properties from grain growth behavior by artificially producing growth sites from means other than native nucleation. The most commonly explored of these processes include excimer laser induced crystallization (ELA) [68–70] and metal induced crystallization (MIC) [71–75]. These processes are typically used to generate a thin poly-crystalline "seed layer" by generating nucleation sites artificially from crystallization of an a-Si:H base-layer film. These base layer grains are then epitaxially "thickened" through either a low pressure chemical vapor deposition (LPCVD) or electron beam (e-beam) evaporation growth on the seed layer. Although these methods have been successful in eliminating the incubation period and controlling grain size to a certain degree, very few processes were capable of surpassing laboratory efficiencies of 6%. Furthermore, they introduce additional equipment, relatively high temperature processing steps, and performance hindering contamination.

Seed-Induced Grain Growth

A relatively small body of work has been devoted to investigating the effects of embedding an initial population of crystallites in a-Si:H film prior to annealing to serve as "seed" material for grain growth during annealing. This seed-induced process eliminates the grain-control complications associated with native nucleation, including lengthy incubation periods and nucleation rates, and avoids the intentional introduction of impurities commonly associated with MIC processes. Of the small number of works that have attempted a variation of seed-induced crystallization techniques, significant promise has already been shown in reduced annealing times and enhanced grain structure control relative to native nucleation based processes [60,62,76–78].

For instance, work in [76] and [62] measured significantly reduced thermal budgets by annealing a-Si:H films deposited on top of substrates initially coated with a relatively thinner, mixed-phase layer. Similarly, work in [60, 78, 79] measured reductions in annealing times and enhanced grain sizes by annealing a-Si:H films having mixed phase layers. These mixed-phase seed layers were formed at intermediate positions in the film thickness by careful tuning of plasma conditions. Furthermore, work in [77] and [80] showed similar advantages by annealing films consisting of a-Si:H film grown on top of substrates coated in nano-crystallites that were grown in a separate process.

Although promising reductions in annealing times have been achieved in each of these techniques, little else has been done to explore the basic parameter spaces surrounding seed-induced crystallization, including the effects of varying basic seed crystal properties such as size, shape and concentration, or the effects of varying basic properties of the surrounding amorphous film. This is most likely on account of complications commonly associated with controlling the properties of seed crystal synthesis independently from amorphous film synthesis. In many of the techniques discussed above, seed material is deposited in tandem with the amorphous film, by careful plasma tuning, nucleating crystalline regions within the depositing amorphous film. Subsequently, the properties of the surrounding amorphous film are inherently linked to the conditions favorable for seed material formation.

A select few cases, such as in Kim *et al.*, have synthesized seed crystals independently from amorphous film using an external process such as liquid dispersion. However, such techniques require etching procedures, or exposure to air contamination before crystallites are finally included in a-Si:H film [80]. Ultimately, both plasma-tuned and externally synthesized techniques for seed material formation have yet to demonstrate reproducible control over basic seed crystal properties, including size distribution, and concentration within the film. The work herein demonstrates a process that addresses the issues commonly involved with seed-induced crystallization, mainly, the independent control of amorphous and seed crystal components. Furthermore, this process was utilized to perform a series of studies outlining the effects of varying such basic parameters as seed crystal concentration, seed crystal shape, and amorphous film deposition conditions, on the crystallization behavior and final grain quality of seed-crystallized films.

Chapter 3

Experiment

3.1 Dual Plasma Deposition System

This work outlines a novel approach to synthesizing poly-Si thin films from the solid-phase crystallization (SPC) of a-Si:H thin films containing embedded nanocrystallites. As previously outlined, these nanocrystallites are to serve as predetermined grain-growth sites, or grain-growth "seeds", during the annealing process. This technique is intended to eliminate the complications associated with native nucleation, such as lengthy incubation times and grain density control. As outlined in Chapter 1, this method has been largely unexplored in silicon thin-film research, due primarily to the complexities involved with independent synthesis of high quality seed material.

The technique utilized in this work attempts to provide a solution to the common difficulties of seed material synthesis, by the development of a "dual-plasma" deposition system shown in figure 3.1. With this configuration, two separate plasmas are operated within the same vacuum chamber, but separated by an orifice to maintain a pressure differential. This allows for one plasma to be operated at conditions optimal for high quality a-Si:H film deposition, while the second plasma is operated at conditions optimal for producing high quality nanocrystals.

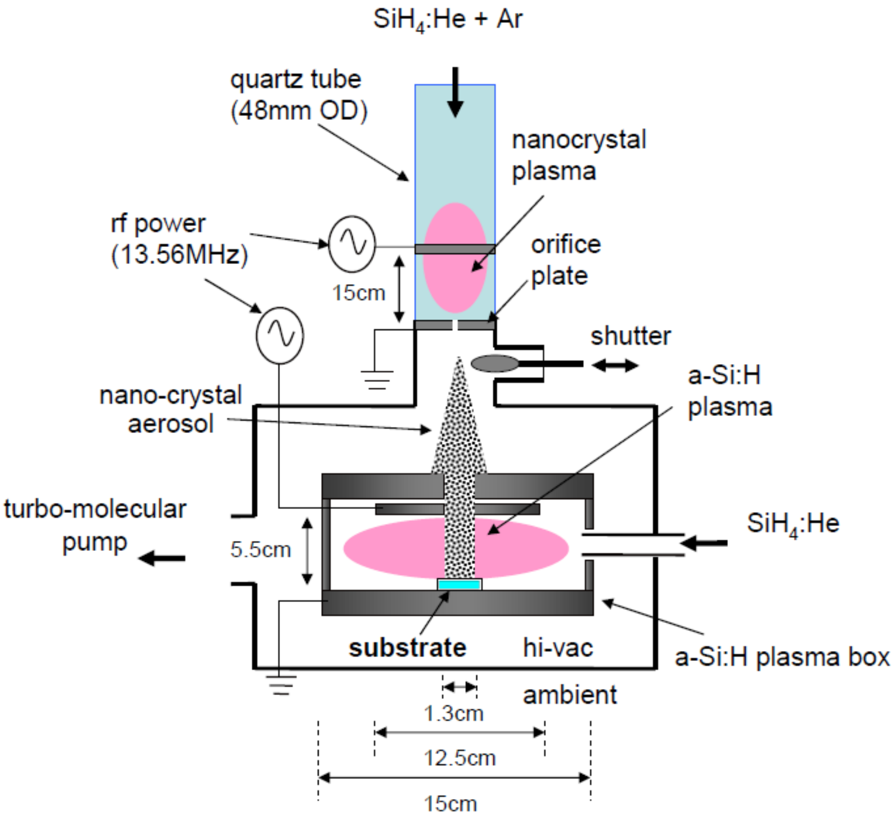

Figure 3.1: Schematic of dual plasma deposition system.

3.1.1 Seeded Film Structure

The film structure used as the basis of study for this work, was synthesized in a three-stage deposition process illustrated in figure 3.2, and then annealed to create a poly-crystalline film. The first stage involves depositing an amorphous film "base layer", 50 *nm* to 100 *nm* thick, from the downstream a-Si:H film plasma. In the second stage, the film growth discharge is turned off and the upstream nanocrystal discharge, in the quartz tube region, is turned on. A shutter blocking the orifice between each region is then manually withdrawn, allowing particles synthesized in the upstream quartz tube to deposit in a "mono-layer" on top of the a-Si:H film base layer. The third step involves deposition of an additional amorphous film "top layer" from the downstream a-Si:H film plasma. The resulting film is composed of a planar layer of seed crystallites "sandwiched" between two layers of a-Si:H film. Due to the monolayer arrangement of seed crystallites, film seed concentrations can be quantified in terms of aerial "seed densities", having units of nanocrystals per unit area. Figure 3.3 below shows the relationship between duration of shutter withdrawal and the resulting seed density. Films are then annealed at temperatures between 550 °C to 650 °C with the intention that grain growth will proceed exclusively from the embedded seeds and eventually encompass the extent of the film.

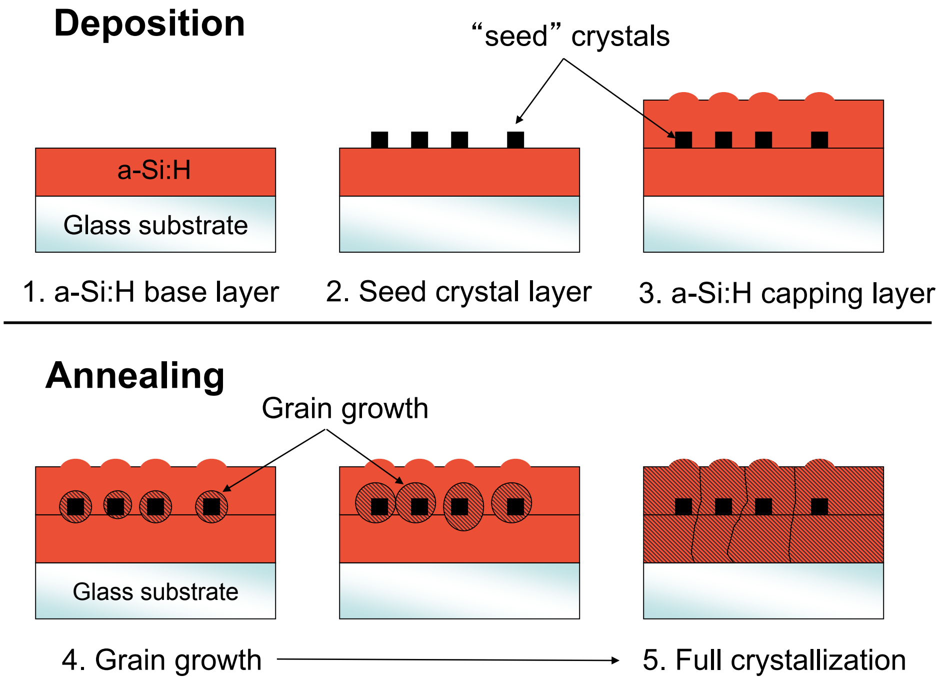

Figure 3.2: Top: Schematic of three-stage seeded film deposition. Bottom: Depiction of seeded grain growth during film annealing, following deposition.

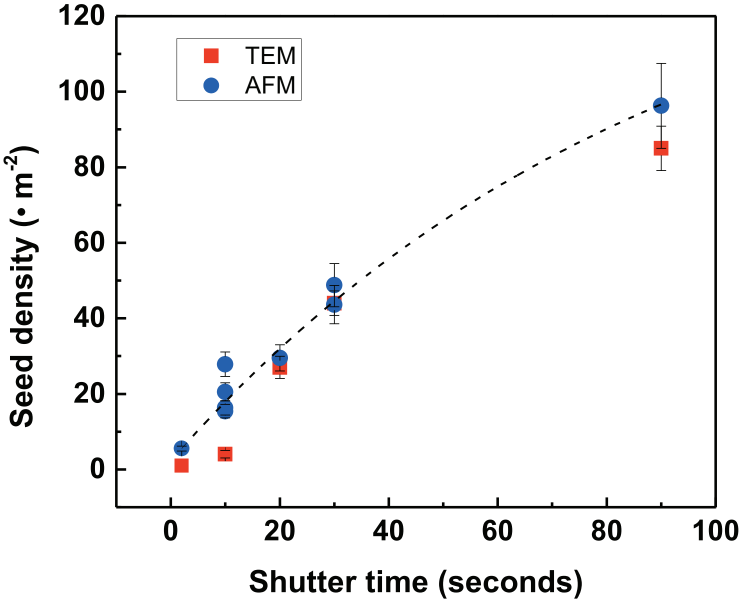

Figure 3.3: Aerial seed density versus duration of shutter withdrawal during seed particle deposition. AFM data was taken using surface topography measurements on several 200 nm seeded films. TEM data was taken by Curtis Anderson [81]

.

3.1.2 a-Si:H Film Growth

Deposition Parameters

The a-Si:H component of each seeded film is deposited from 5% silane diluted in helium, using a capacitively-coupled RF discharge operating at a frequency of 13.56 MHz, nominal powers ranging from 2 W to 25 W, and pressures ranging from 100 mTorr to 400 $mTorr$. Films are grown in a chamber evacuated to a base pressure between 10^{-8} $Torr$ and 10^{-7} $Torr$ by a turbo molecular pump, with the a-Si:H discharge confined to a cylindrical "plasma box" configuration, having the critical dimensions shown in figure 3.1. Table 3.1 provides a summary of the ranges of deposition parameters used in a-Si:H film growth for this work, as compared to common values reported in literature.

Table 3.1: Summary of basic a-Si:H film deposition parameters used for the studies in this work. Values are compared to common literature ranges taken from [25, 26]

.

deposition parameter	power density (W/cm^2)	dep. rate (nm/min)	dep. temp. (°C)	dep. Pressure ($mTorr$)
literature values	10-100	1-50	25-500	200-1000
dual plasma system	40-200	1-12	250	100-400

It should be noted that, with the exception of the powered electrode plate (denoted by the 12.5 *cm* dimension in figure 3.1), the entire plasma box is at ground potential. The powered electrode plate is electrically insulated from the grounded portions of the plasma box by means of ceramic screws, which secure it to the roof of the plasma box while maintaining a 3 *mm* vertical spacing from the grounded plasma box.

This plasma box geometry results in a ratio of grounded area to powered electrode area to be approximately 4. According to equation 3.1, this results in a voltage drop between the plasma bulk and substrate that is reduced from the delivered RF potential by a factor of over 250 [82, 83]. The intention of this design is to improve the quality of the deposited a-Si:H film by reducing the ion bombardment energy on the growing film surface.

$$\frac{V_{grounded}}{V_{powered}} \approx \left(\frac{A_{powered}}{A_{grounded}}\right)^4 \tag{3.1}$$

Film Properties

In validating the quality of the a-Si:H film deposition process, a few common film parameters were characterized and compared to typical values found in literature. Specifically, the content and nature of hydrogen bonding within the film is of primary significance, as incorporated hydrogen serves to terminate dangling bond defects in the amorphous matrix.

Numerous studies have determined that typical device grade [1] a-Si:H films have a hydrogen content in the range of 8% to 11%(at.), with lower concentrations leading to films with significant populations of unterminated dangling bonds [25, 26, 84, 85]. Conversely, excessive hydrogen content can often result in films having porous, vacancy-rich, regions stabilized by clustered silicon-hydrogen bonds. [25,84,86–89]. Subsequently, the ratio of clustered to isolated hydrogen bonding within an a-Si:H film (also known as "microstructure" or "R*") is a parameter of interest in assessing film quality. Typical R* values for device-grade PECVD a-Si:H vary between 0.05 to 0.2 [25]. Measured values for hydrogen content and microstructure of as-deposited films grown for this work are shown listed in table 3.2 along with typical values found in literature. Hydrogen content was measured using a "forward recoil scattering" (FReS) mode of Rutherford backscattering. Microstructure was measured by Fourier transformed infrared (FTIR) spectroscopy, using the techniques and correction factors developed in the works by Brodsky [90] and Langford [91].

Since crystallization kinetics have been measured to be influenced by impurity concentrations on the order of 10^{18} cm^{-3} or higher [92], a basic characterization of the impurity presence resulting in the a-Si:H film growth process is also of interest. This was conducted by performing opto-electronic measurements on as-grown, un-annealed, films. Since common impurities such as oxygen and nitrogen can shift the Fermi level of a-Si:H by several hundred milli-electron volts (meV) if present in amounts greater than 10^{17} cm^{-3} [25], dark conductivity and dark conductivity activation energy are a simple means of inferring film purity within the sensitivity required for SPC studies. For instance, device-grade films with impurity populations below these concentrations, and with hydrogen contents within the ranges shown in table 3.2, should exhibit dark conductivity values of 10^{-10} S/cm or lower, with an activation energy near 800 meV to 900 meV (roughly half the mobility gap) [25, 85, 93].

---

[1] Device grade refers to films having sufficient structural and electronic quality to be utilized in device application. Typically, this refers to uniformity, lack of surface roughness, and reasonable defect and impurity levels

Table 3.2: Summary of a-Si:H film properties measured from test case films grown in the plasma box shown in figure 3.1. Values are compared to common literature ranges taken from [25, 26]

film property	σ_{dark}	E_A	$\left(\frac{\sigma_{photo}}{\sigma_{dark}}\right)$	H%	R^*
–	(S/cm)	(eV)	–	–	–
literature values	$\sim 10^{-10}$	~ 0.9	$> 10^5$	8-11%	< 0.2
dual plasma system	$10^{-12} - 10^{-9}$	$0.9 - 1$	$10^4 - 10^6$	7-13%	0.02 - 0.15

Furthermore, since other electronically active defects, such as metallic impurities from chamber materials, can limit the current produced under film illumination, photo-conductivity was was also measured. Typical values for device grade a-Si:H film exhibit a ratio of photo-conductivity to dark conductivity near 10^5 or higher [25]. Dark conductivity and its activation energy were measured using a film device structure consisting of 2 mm wide chromium contacts evaporated to form 1 mm channels. Conductivity was characterized from current-voltage (I-V) sweeps from -100 V to +100 V. Activation energies were approximated from similar (I-V) sweeps repeated over a temperature range of 300 K to 450 K, measured in 1 K increments. As table 3.2 shows, the properties of films grown from the plasma box discharge in the dual plasma system are within acceptable ranges found in literature.

3.1.3 Seed Crystal Synthesis

Nanocrystal seeds were synthesized in the capacitively-coupled, quartz tube flow-through reactor shown in the upstream portion of figure 3.1. Similar to the a-Si:H film plasma, the nanocrystal plasma was operated at 13.56 MHz, but at a relatively higher pressure of 2.2 $Torr$, and a power of 140 W or greater. Precursor gases used for nanocrystal synthesis consisted of the same 5% silane:helium precursor used in film growth, with the addition of pure argon. A respective mass-flow ratio of 3:4 was typically used for silane and argon precursors. As previously discussed, the nanocrystal reactor tube is connected to the main film growth chamber through a 1 mm diameter orifice. Aside from allowing plasma conditions in the reactor to operate at higher pressures more conducive for large particle growth, the orifice also serves as the ground electrode for the reactor discharge, as well as the passageway for nanocrystals from the reactor to the substrate in the main chamber.

Previous studies have determined that nano-crystallite properties such as shape, size, and quality can be carefully controlled by several key parameters such as pressure, gas flow rate, RF power, and plasma discharge mode [94–98]. The crystallites studied as candidates for grain seeding in this work were synthesized according to the methods of Bapat et al. [94, 95].

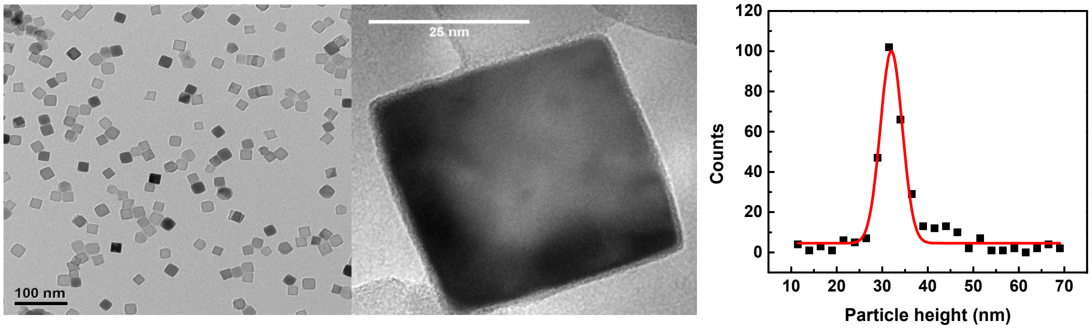

Figure 3.4: Left: TEM images of cubic seed crystals synthesized in the quartz tube reactor shown in figure 3.1. Right: Size distribution of cubic seed crystals as measured using AFM topography data of the surface of a 200 nm seeded film. The average particle size is approximately 32 nm ± 2.5 nm. TEM images were taken by Andrew J. Wagner.

In this method, single crystals, cubic in shape, are synthesized using a precursor combination consisting of 3 standard cubic centimeters per minute (*sccm*) of 5% silane:helium and 4 *sccm* of argon, with a nominal RF power of 140 W. As figure 3.4 shows, this synthesis method results in seed crystallites highly uniform in shape, with a relatively narrow size distribution. The average seed crystal edge length according to this size distribution is approximately 32 $nm \pm 2.4$ nm. The plasma discharge mode associated with yielding cubic shaped crystals is characterized as "filamentary". Unlike a common, uniform capacitive glow discharge, termed as "diffuse", the filamentary plasma mode is characterized by a rotating arrangement of small, relatively high density discharge regions which rotate between the ring and grounded electrodes.

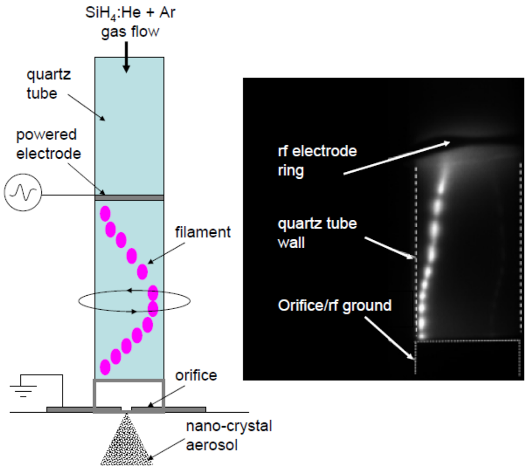

Figure 3.5: Left: Illustration of filamentary plasma mode. Right: High-speed digital camera image of filamentary mode taken from [95].

As figure 3.5 shows, high-speed photography has revealed that this filamentary discharge is composed of a string of 15 to 20 globular discharges with 3 mm to 5 mm length, separated by 1 mm to 2 mm dark regions, rotating with a frequency about 150 Hz [95]. Earlier TEM work has shown the faces of each cube to be terminated by (100) lattice planes. Simulations in ref. [99] argue this (100) termination and cubic shape to be the lowest energy surface for silicon crystallite having hydrogen terminated surface bonds.

Chapter 4

Crystallization Kinetics

4.1 Introduction: Motivation for Studies in Crystallization Kinetics

As outlined in chapter 3, following deposition, films are annealed at temperatures above 550 °C to induce grain growth from the embedded population of seed crystals. The objective is to have grain growth originate exclusively from the embedded population of seed crystals, proceeding until grains coalesce to form a device-grade poly-Si film. Ideally, the resulting grain structure should have an average grain size dictated by the initial seed spacing. For these requirements to occur, it is necessary that seeded grain growth be completed in a time interval smaller than the incubation period of the surrounding a-Si:H film. Regions of the film that are not crystallized within this time interval will nucleate native grains, subsequently limiting control over the final grain size of the film. Therefore, it is necessary to characterize the grain growth rate of seeded films relative to similar unseeded films in order to determine the time frame available for grain growth. The studies outlined in this chapter compare crystallization rates, and relevant annealing times of films of a single, test-case seed density over a range of common annealing temperatures.

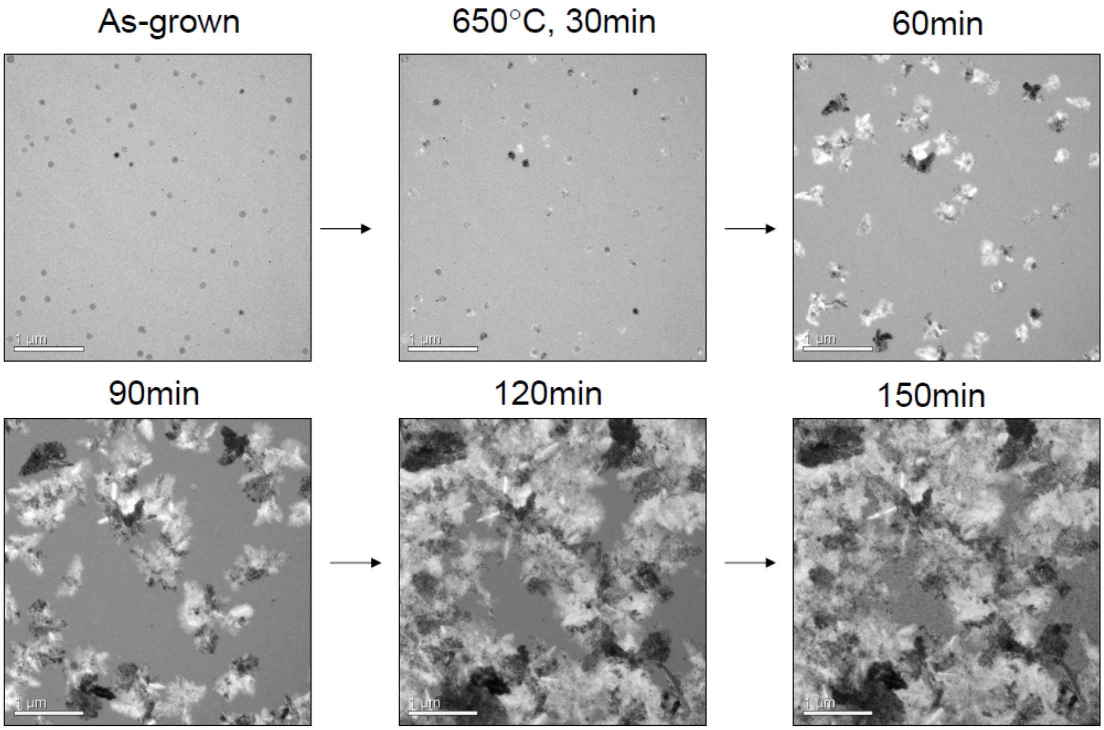

Figure 4.1: In-situ heated stage TEM images of a seeded film during annealing at 650 °C. Taken by Curtis Anderson [81].

An example of the desired “seeded” growth behavior is shown in figure 7.6, displaying time lapse images of a seeded film taken by transmission electron microscopy (TEM), in-situ, during annealing at 650 °C. The ”as-grown” image shows an aerial view of the film with the embedded seed population, prior to annealing. Successive views show the film’s behavior over several minutes at 650 °C, with grain growth originating exclusively from the seed crystals, and encompassing most of the viewed area by 150 min. The resulting grain sizes are subsequently on the order of the initial seed separation; roughly 4 μm^2 in this case. The film consists of a single seed layer deposited between a 20 nm a-Si:H base layer and 80 nm top layer. The observed lack of native nucleation suggests films of this structure require less annealing time than a commensurate film without an initial seed crystal population.

4.2 Raman Crystal Fraction

In-situ TEM characterizations are useful for assessments of grain growth geometry and behavior on relatively small, μm, length scales. However, in order to more quantitatively assess the annealing behavior of seeded films over larger sample areas, Raman spectroscopy was used to monitor the progression of grain growth over centimeter length scales. In the Raman spectra of silicon, the peak shape, and location are distinctly different for amorphous and crystalline phases. This allows for the volume fraction of crystalline phase present, in a particular film, to be estimated from relative peak contributions [100–103]. For the studies outlined in this chapter, Raman spectra were taken at regular intervals during annealing, averaged over sample areas of 150 mm^2, and used to generate plots of crystal fraction with respect to anneal time. An example fit of a sample annealed to a crystal fraction of approximately 34% is shown in figure 4.2.

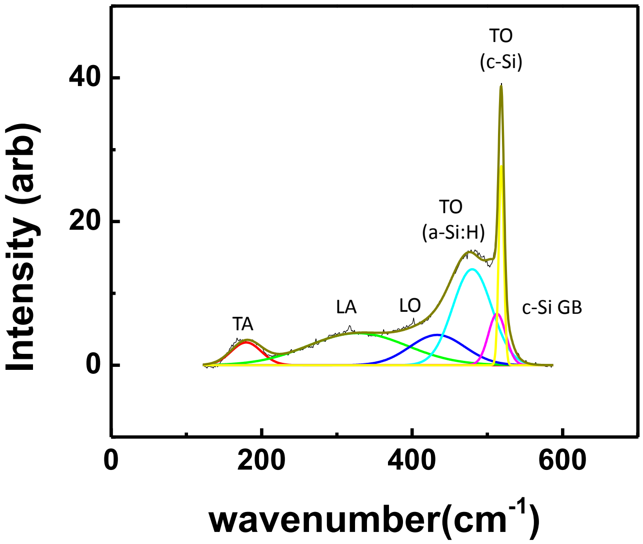

Figure 4.2: Raman spectra and peak fitting of an amorphous silicon sample, partially annealed at 625°C. The crystal fraction at this state was calculated to be approximately 34%, using equation 4.1 along with the fitting technique outlined in ref. [103]. The two highest wavenumber peaks labeled TO (c-Si) and c-Si GB (yellow and pink, respectively), represent the crystalline portions of the Raman spectra.

Spectra peaks were fit according to the technique outlined in the work of Smit et al. [103] Crystal fraction (“X_c”) was estimated using equation 4.1 below. I_{aSi-TO} corresponds to the integrated peak intensity of the transverse optical (TO) peak associated with the present amorphous phase, typically found near 480 cm^{-1}. I_{cSi-TO} corresponds to the integrated peak intensity of the transverse optical (TO) peak associated with the present crystalline grains, typically found between 515 cm^{-1} to 521 cm^{-1}. I_{cSi-gb} corresponds to the integrated peak intensity of the peak associated with strained bonds and grain boundaries at the grain surfaces; typically found between 500 cm^{-1} to 510 cm^{-1}. Due to the difference in scattering cross-sections for amorphous and crystalline phases, a correction factor, β, of approximately 0.8 was used based on previous reports [100, 101, 103].

$$X_c = \frac{I_{cSi-TO} + I_{cSi-gb}}{I_{cSi-TO} + I_{cSi-gb} + \beta I_{aSi-TO}} \tag{4.1}$$

4.3 Raman Crystal Fraction Study 1: The Effect of Varying Anneal Temperature on Similar Films

In an initial study of seeded grain growth rates, the progression of Raman crystal fraction during annealing was measured for several seeded films and compared to films of equal thickness consisting only of a-Si:H material (“unseeded” films). Four pairs of similar samples (4 seeded and 4 unseeded) were deposited on 2.5 cm x 2.5 cm square Eagle XG glass subsrates. Total film thicknesses were 180 nm to 200 nm. Seeded films consisted of a single seed layer, with aerial seed density of $\sim 16/\mu m^2$, deposited between two 90 nm to 100 nm a-Si:H layers. All a-Si:H layers were grown at 100 $mTorr$ with a nominal RF power of 5 W and a substrate temperature of 250 °C. Samples were annealed in a quartz tube furnace, in nitrogen ambient to mitigate oxide growth. At regular time intervals, ex-situ Raman spectra were averaged from 5 locations on each sample, using a Witec alpha 300R confocal microscope, which resolved scattering from a 514.5 nm Argon laser source. A 10x aperture having spot size of $\sim$250 μm was used to focus the incident laser signal, and laser power was kept below 5 milliwatts to avoid inducing crystallization during measurement. This was repeated for four separate annealing temperatures: 600 °C, 625 °C, 650 °C, and and 675 °C. The evolution of crystal volume fraction with anneal time was then plotted for each sample pair, shown in figure 4.3 below.

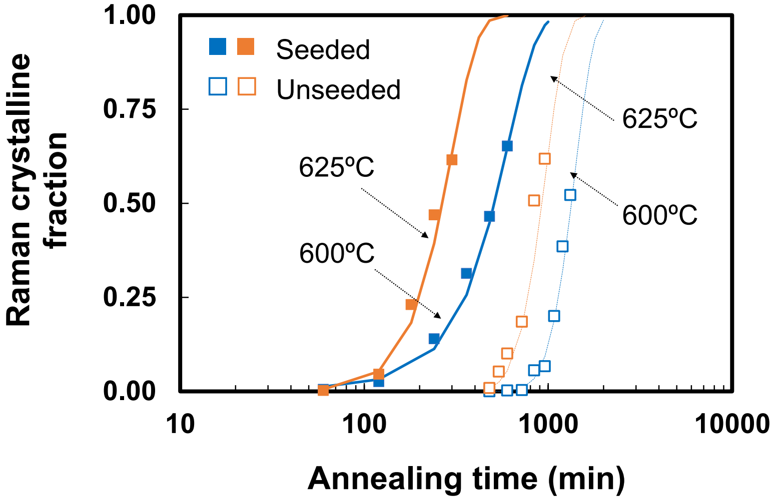

(a)

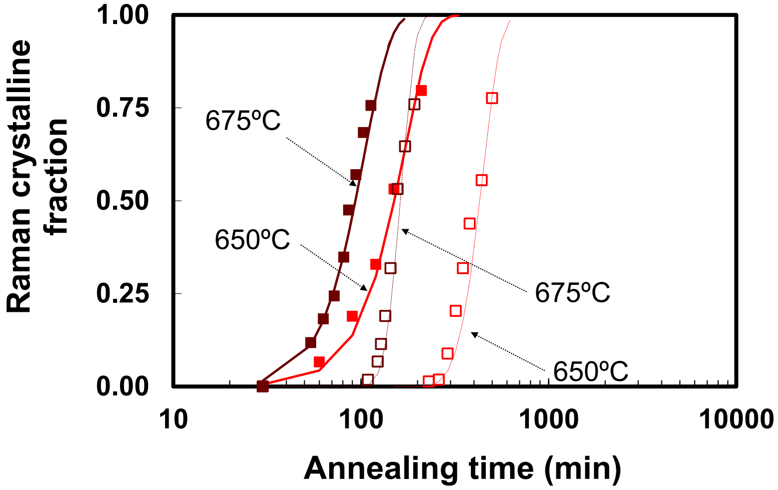

(b)

Figure 4.3: Progression of Raman crystal fraction with annealing for seeded and unseeded films annealed at four different temperatures. Figure (a) shows 600 °C and 625 °C results as measured in ref [81]. Figure (b) shows 650 °C and 675 °C results. Arbitrary fit lines were included as a guide for the eye.

4.3.1 Crystallization Time

It is clear from figure 4.3 that the time required to crystallize a seeded film is significantly reduced relative to similar unseeded films. This reduction can be quantified by using a common metric known as the crystallization time, which is equivalent to the time at which $\sim 63\%$ of the film volume is measured to be crystalline by Raman spectroscopy estimates. As figure 4.4(a) shows, the most significant reduction in crystallization time occurs at lower annealing temperatures, with seeded crystallization times occuring almost 800 *min* earlier at an anneal temperature of 600 °C. It is interesting that this reduction window shrinks with increasing anneal temperature; a trend which suggests that the kinetics governing seeded growth rate have a lower temperature sensitivity than the kinetics governing native nucleation.

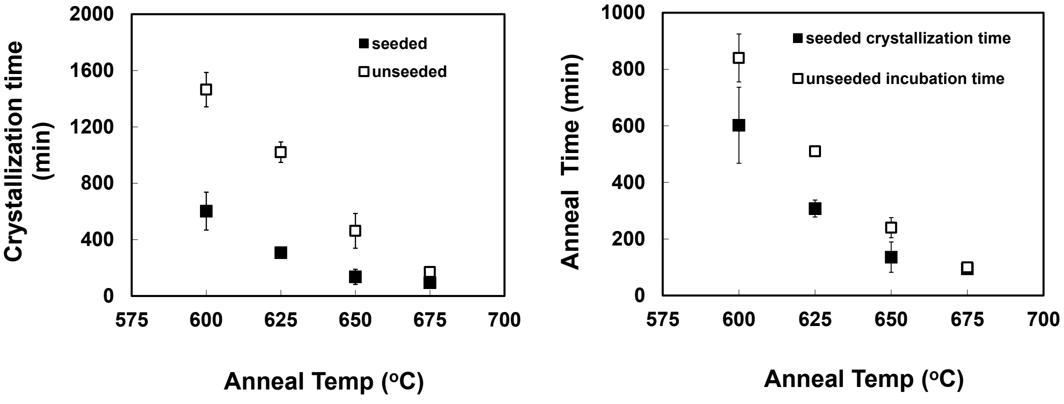

(a) (b)

Figure 4.4: (a) Comparison of crystallization times for the seeded and unseeded film data from figure 4.3. (b) Comparison of seeded crystallization times to unseeded incubation times. Incubation times were measured as the average of the measurement times between first measured onset of crystallization and the time of the measurement previous to first onset. Error bars are taken as the time interval between the two corresponding onset measurements.

A similar trend is shown in figure 4.4 b), where the crystallization time of seeded films is compared to the incubation time of unseeded films for each annealing temperature. This shows that seeded films are mostly crystalline before the onset of native nucleation, suggesting that the measured grain growth in seeded films results primarily from the embedded population of seed crystals, for the anneal temperatures used.

4.3.2 Seeded Grain Growth Rate

The temperature sensitivity of seeded grain growth can be quantitatively assessed by plotting grain growth rate with respect to annealing temperature. Grain growth rates for seeded films were found by fitting crystal fraction curves with a modified version of the "site-saturated" Kolmogrov-Johnson-Mehl-Avrami (KJMA) model of phase transformation [104–108], shown in equation 4.2. With the film thickness L, and the aerial seed density N_s known, crystallization curves can be fit using the radial, one-dimensional grain growth rate v_g as the only fit parameter. Fit lines were established by varying v_g to minimize the sum of the square error.

$$X_c = X_{c_{max}} \left(1 - exp \left(-4\pi \frac{N_s}{L} {v_g}^2 t^n \right) \right) \tag{4.2}$$

A power-law time dependence with exponent "n" of 3 was used based on the assumption of three-dimensional, isotropic grain growth from a fixed initial population of growth sites. These assumptions define the site-saturated version of the KJMA model. With the population density of seed crystals used in this particular study, average seed spacing (estimated by AFM and TEM) is large enough that adjacent grains should theoretically reach the limitations of the film (substrate or surface interfaces) before overlapping with each other, and reducing the dimension of growth. Furthermore, since it is known from TEM observations that grain growth from seed crystals is not precisely isotropic, resulting growth rates are taken as an approximation of an equivalent, isotropic, radial grain growth rate. Figure 4.5 (a) shows the fit quality of equation 4.2. The maximum of each crystallization curve occurs below a fraction of 100% due to regions of amorphous tissue which remain within the grain boundaries of the final poly-Si film. Fit lines were subsequently adjusted using the correction factor $X_{c_{max}}$, which is the crystal fraction measured at the plateau, or "complete crystalliation" of each curve.

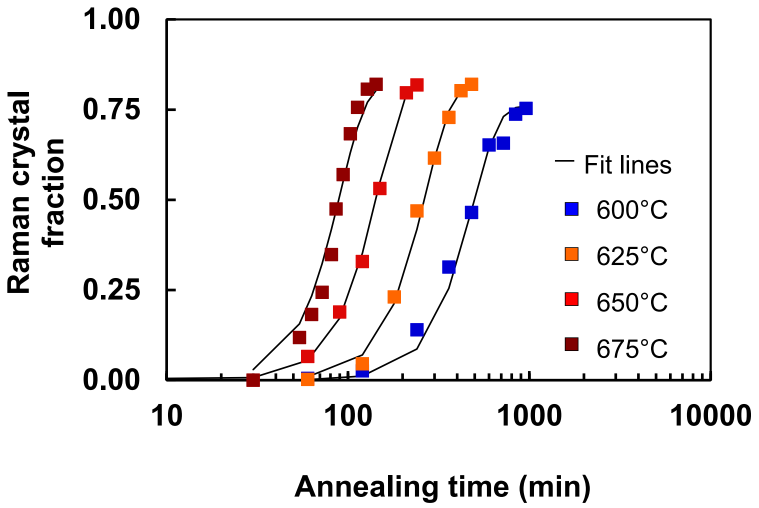

(a)

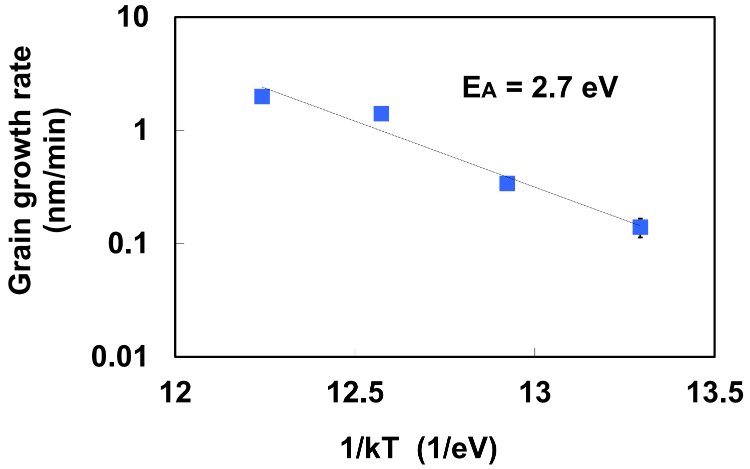

(b)

Figure 4.5: (a) Fit quality of the site saturated KJMA model to the seeded crystallization data originally shown in figure 4.3. Fit model lines are depicted in solid black, with data in colored symbols. The fit model is outlined in equation 4.2, with growth rate v_g being the only fit parameter. Figure (b) shows the subsequent growth rates extracted from the fit lines in (a), plotted in Arrhenius form. A growth rate activation energy of 2.7 eV was subsequently found.

The activation energy for seeded grain growth for this set of films was subsequently found to be $\sim 2.7\ eV$. This shows good agreement with literature results for epitaxial grain growth of a-Si:H deposited and annealed on (100) c-Si wafer substrates, which has been found to be $\sim 2.68\ eV \pm 0.05\ eV$ [46]. If grain growth were to proceed due to native nucleation, growth rates would exhibit a much higher activation energy, measured in literature to be $\sim 5\ eV \pm 0.1\ eV$ [45, 46, 54, 109]. The much higher energy barrier measured for native nucleation is due to the sum of two, concurrent, thermodynamic barriers: 1) the energy required to form stable grain clusters from an existing amorphous matrix ($\sim 2.0\ eV$ to $2.1\ eV$ [110]), and 2) the energy required to induce growth from stable clusters once they are formed ($\sim 2.2\ eV$ to $3.1\ eV$ [45,111,112]). It is subsequently intuitive that the growth-rate activation energy of seeded films should fall within the latter range, due to the average seed crystal size of over 30 nm, which is well above the theoretical stable cluster diameter of approximately 2 nm [46]. Furthermore, these findings are consistent with the decreasing gap in seeded and unseeded crystallization times shown in figure 4.4(b).

4.3.3 Avrami Slope

The assumption of three-dimensional growth can be more quantitatively validated by evaluating the time dependence corresponding to each crystallization curve [107, 109]. This was done by replotting the data in figure 4.3 in a logarithmic scaling with the quantity $ln(ln(1 - X_c))$ as the ordinate, and the natural log of time as the abcissa. As is shown in figure 4.6 (a), when crystal fraction data is displayed in this log-log fashion, a linear regime can be observed at the beginning of each crystallization curve. This regime can be assigned a slope value, referred to as the “Avrami slope”, equivalent to “n” in equation 4.2. The Avrami slope indicates the order of the time dependence of the crystallization, and subsequently can be associated with the dimension of growth. Slope values below 4 are typically associated with grain growth occuring in 3 dimensions or less, from a fixed or ”site-saturated” population of growth sites. Conversely, Avrami slopes greater than 4 are associated with grain growth from an increasing number of sites, such as with native nucleation [107, 108, 113]. Ideally, an Avrami slope near 3 would be expected for seeded crystallization curves if grain growth proceeded as three-dimensional, unobstructed, radial grain expansion from a fixed number of growth sites.

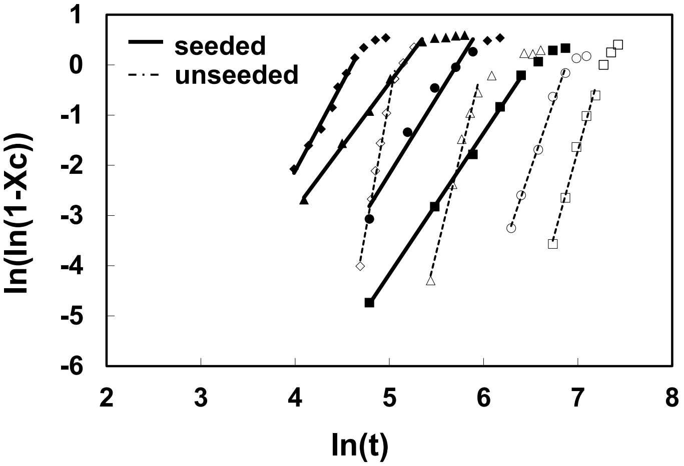

(a)

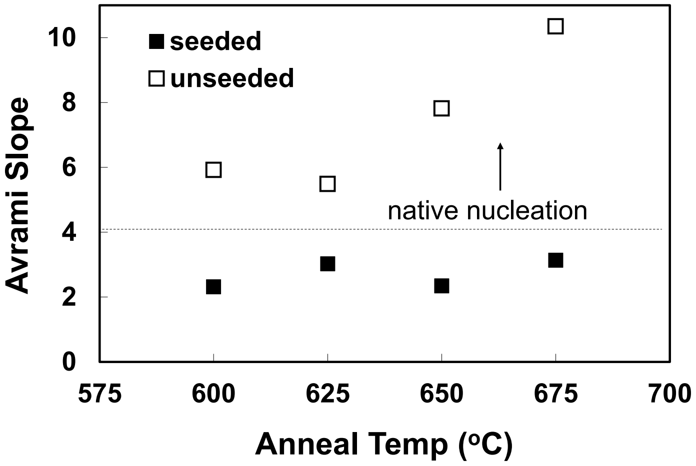

(b)

Figure 4.6: a): logarithmic (Avrami) plot of the crystallization curves from figure 4.3. The linear regimes revealed for each line provide a slope associated with the time-dependence of grain growth. A slope of 4 or greater is indicative of native nucleation. Seeded samples (solid lines) subsequently exhibit mildler slopes than unseeded samples (dotted lines). For each sample set, annealing temperature increases monotonically from right to left, between 600 °C to 675 °C in 25 °C intervals. b): Comparison of the Avrami slopes of each curve from figure a).

The Avrami slopes of unseeded films fall between 5-10 for each anneal temperature, suggesting growth behavior indicative of native nucleation. Seeded films exhibit much more uniform behavior with temperature, with slopes falling within a much narrower range of 2.3 to 3. This is expected behavior for grain growth originating from a fixed population of growth sites, suggesting that a site-saturated KJMA model can be used to estimate seeded grain growth rates for each temperature.

4.4 Conclusions

Grain growth has been demonstrated from seed clusters pre-implanted in amorphous silicon thin film layers by method of a dual-plasma deposition. Grain growth was quantitatively confirmed to originate exclusively from the initial population of seed crystals by analysis of Raman crystal fraction curves. A measurable reduction in required anneal time was observed for seeded films relative to unseeded films of similar thickness. Grain growth rates were found to be approximated effectively by a modified version of the KJMA transformation model. The corresponding thermodynamic barrier to grain growth from seed crystals was subsequently measured, and found to be in agreement with studies on epitaxial growth rates.

Chapter 5

The Effect of Varying Seed Density

5.1 Introduction

5.2 The Effect of Varying Seed Density on Grain Growth Rate

The results discussed in the previous chapter compare the crystallization kinetics of unseeded films to one particular seeded film structure; specifically, 200 nm thick films, having seed densities of approximately 16 μm^2. The following section summarizes the results of similar studies, on films consisting of various initial seed concentrations, herein referred to as "seed densities", on account of the planar distribution of the seed layer. Figure 5.1 below shows the progression of Raman crystal fraction with anneal time at 650 °C for three samples deposited with different initial seed densities, along with a fourth unseeded sample of similar thickness. Each film was approximately 180 nm to 200 nm in thickness, with seeded films consisting of a single seed layer at mid-depth. Aerial seed crystal densities of each film were measured by AFM (shown in figure 5.1 (a)) to be $\sim 6/\mu m^2$, $\sim 15/\mu m^2$, and $\sim 32/\mu m^2$.

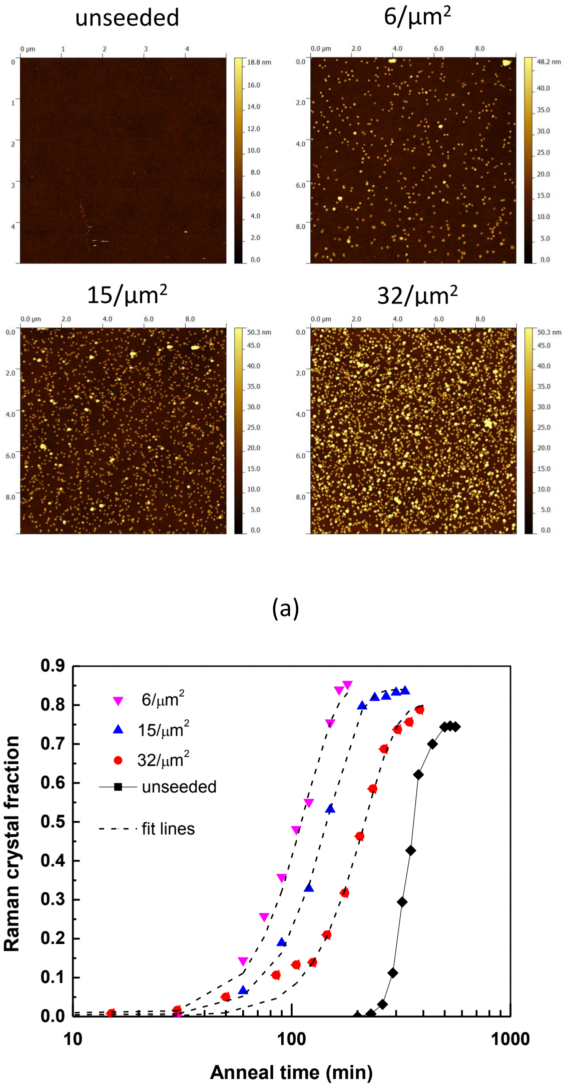

(a)

(b)

Figure 5.1: (a) AFM surface topography of four samples of varying initial seed density, prior to annealing. Seeded samples labeled low, medium and high were measured to have average seed densities of $\sim 6/\mu m^2$, $\sim 15/\mu m^2$, and $\sim 32/\mu m^2$, respectively. (b) Resulting crystallization curves of the samples shown in figure a), during annealing at 650 °C. Results show samples with lower initial seed densities crystallize faster than more heavily seeded samples.

The resulting crystallization curves are shown in figure 5.1 (b). Each seeded sample exhibits an almost immediate onset of crystallization, while no crystallization is observed for the unseeded sample before the completion of an incubation period of approximately 300 min. At the conclusion of the unseeded film incubation period, crystallization for the seeded samples is mainly complete, suggesting the absence of native nucleation. A more interesting observation, however, is that samples having lower initial seed density exhibit relatively faster crystallization rates than more heavily seeded samples.

In order to examine this effect over a larger range of seed densities, crystallization rates were compared over a series of 10 samples having initial seed densities ranging from $5/\mu m^2$ to $100/\mu m^2$. Each sample was annealed at 650 °C to complete crystallization, and grain growth rates were subsequently extracted from each crystallization curve by fitting with equation 4.2. It should be noted that each sample achieved complete crystallization prior to the time that onset of native grain growth was measured in similar unseeded films, indicating an absence of native nucleation. Figure 5.2 shows the resulting variation of grain growth rate with respect to seed density for the measured samples. It is clear from the observed trend that, within this range of seed densities, grain growth rate decreases for films with larger seed crystal populations.

It is intuitive to infer that the effects observed in figure 5.2 are perhaps the result of a competitive effect between adjacent seed crystals. For instance, if each seed acts as a multi-directional growth site, neighboring seeds may encounter resistance from one another in higher seed density films, due to competition for amorphous ad-atoms. However, such an effect is difficult to empirically quantify beyond the trends of crystallization curves already shown. Another explanation is that the inclusion of additional seed crystals may have a disordering effect on the structure of the host film. As the AFM images of figure 5.1 (a) show, the seed plane significantly increases the surface roughness relative to unseeded films. It is possible that the texture of the seed plane affects the depositing top a-Si:H layer in a manner that inhibits the bond re-arrangement necessary to promote grain growth.

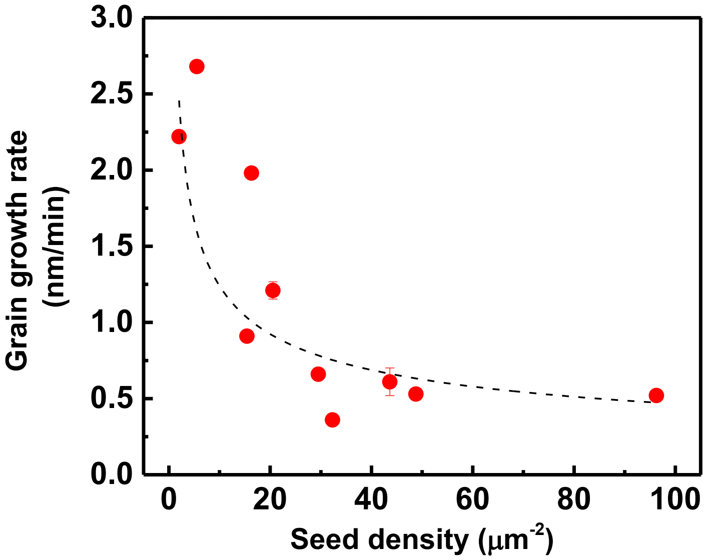

Figure 5.2: Grain growth rate for several samples of varying intital seed density, during annealing at 650 °C. Results indicate that growth rate is inhibited by relatively large seed densities.

Numerous studies have demonstrated a link between film disorder and suppressed crystallization rate in SPC of a-Si:H films [46, 47, 54, 62, 67, 92]. Specifically, studies by Brahim *et al.* have shown that a-Si:H films grown at higher deposition rates exhibit suppressed nucleation and grain growth rates [47, 92]. This was attributed to a greater degree of defects within the bond matrix, inherent to higher deposition rate films. Furthermore, studies by Wu *et al.* [67] have shown that ion implantation of amorphous films prior to annealing can reduce nucleation and grain growth rate, due to the “unrelaxed” state produced in the film by ion bombardment. These results have been argued to be due to the additional energy required to restructure strained amorphous bonds during the native incubation period [54, 110].

In seeded films, the depositing top layer of amorphous silicon may contain a similar disorder from deposition over the surfaces of the cubic seed crystallites. However, since the population of grain nuclei are present prior to annealing, an incubation period is non-existent. Subsequently, for seeded films, any relaxation of the disorder in the surrounding amorphous matrix must occur during grain growth, rather than prior to grain growth as in native nucleation. For this reason, film disorder may play an even more influential role in the crystallization of seeded films. Hence, it is interesting to study the disorder introduced in the surrounding a-Si:H film, for various seed densities, as this may explain the observed decrease in grain growth rate with seed concentration.

5.3 The Effect of Film Disorder

Disorder in amorphous silicon is characterized as structural deviations from an FCC crystalline configuration. Typically, disorder is divided into two main categories according to the length-scale of deviations within the bond matrix. Short-range disorder is associated with defects affecting the film on the order of 1 Å to 3 Å, consisting mainly of strained or twisted bonds, affecting up to 2 nearest-neighbor atoms. Medium-range disorder is associated with defects on length- scales of 3 Å to 25 Å, consisting mainly of atomic vacancies or porous regions affecting a volume of film equivalent to 3 to 10 atoms in diameter.

5.3.1 Short range disorder

The amorphous Raman signature is commonly used to characterize the degree of short range disorder within as-deposited a-Si:H films. Specifically, the full width at half maximum (FWHM) of the transverse optical (TO) peak is most commonly correlated with the average distribution of bond angles within the film [114, 115]. Figure 5.3 shows the FWHM of the TO Raman peak for 100 *nm* and 200 *nm* as-grown films of varying seed density. The seed plane of each film was deposited at mid-thickness: 50 *nm* and 100 *nm* below sample surface, for 100 *nm* and 200 *nm* films, respectively. The increase in TO width with seed density indicates that the inclusion of seed crystals in the amorphous film provides a measurable degree of short-range disorder.

Due to the strong optical absorption of a-Si:H at a wavelength of 514 *nm*, a majority of the incident light used for this Raman study is absorbed in the top 100 *nm* of film. For this reason, the similarity of TO FWHM trends for 100 *nm* and 200 *nm* seeded films indicates that the observed short-range disordering extends above the immediate seed plane region.

This disordering likely originates within the a-Si:H top-layer, due to a lack of conformal deposition over the textured surface created by the seed plane. Reports in literature support the hypothesis that disorder of this nature, on the short-range scale, can result in a suppression of crystallization rate during annealing. Similar behavior was observed by Matsuyama *et al.*, where it was demonstrated that a-Si:H films deposited on textured glass substrates exhibited a greater degree of short-range disorder, measured by an increase in TO FWHM [66]. In the same study, it was demonstrated that these textured substrate films exhibited lower crystallization rates than films grown on untextured substrates. Furthermore, Park *et al.*, observed that amorphous films deposited and annealed on top of pre-existing microcrystalline layers, showed measurably slower crystallization when the amorphous layer consisted of material with relatively larger Raman TO width [62].

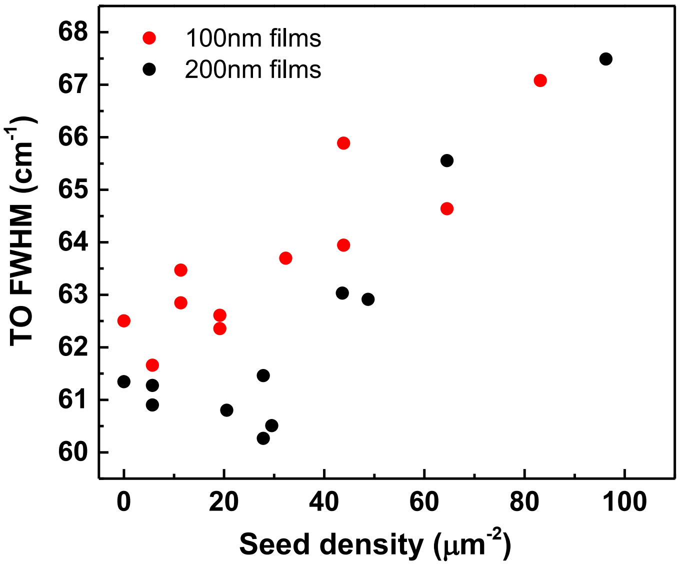

Figure 5.3: Full-width at half-maximum (FWHM) of the amorphous Raman TO peak signature of as-grown samples of various seed crystal concentrations. TO FWHM is correlated strongly with short-range disorder in a-Si:H films. Results indicate an increase the short-range disorder induced by the inclusion of seed crystals. 100 nm thick films were compared to 200 nm thick films to show the prevalence of the short-range disordering effects through the film thickness.

5.3.2 Medium Range Disorder

Microstructure

In order to characterize the full extent of the film disorder induced by the seed layer, the effect of varying seed density on medium range order was also measured. A common metric for characterizing film disorder on a medium range length-scale is the microstructure parameter ("R*"). As discussed in Chapter 3, microstructure is calculated from the FTIR spectra of an as-deposited film, and classified as the fraction of total bonded hydrogen that exists in a clustered formation. Since clustered hydrogen has been shown to reside in vacancy-rich regions of the film, microstructure is typically used as an indication of film porosity [89, 116]. Figure 5.4 shows the variation of microstructure with seed density for the films shown in figure 5.3. R* is relatively unaffected up to seed densities of 30 $/\mu m^2$, above which, increasing steadily from approximately 0.05 to values above 0.10.

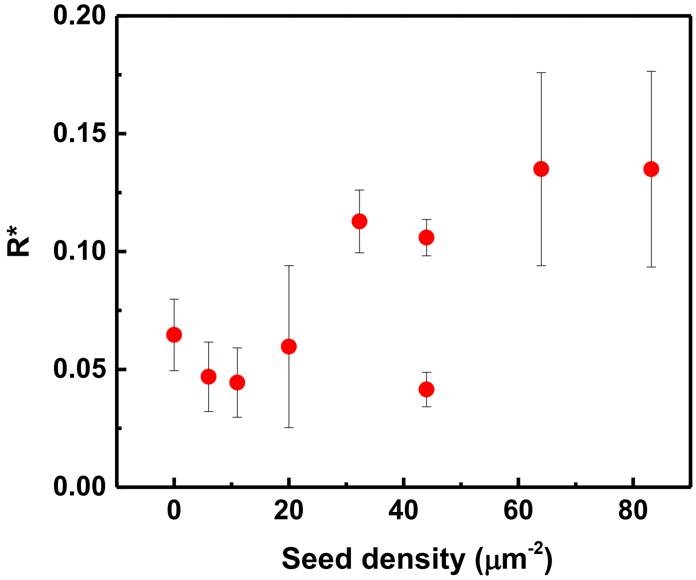

Figure 5.4: Microstructure vs. seed density for the several 100 nm thick films. Relative to unseeded films, microstructure increases by a factor of 2 for films containing seed concentrations greater than $30/\mu m^2$, indicating that a measurable degree of porosity is introduced by seed inclusions. Each data point reflects the average of FTIR spectra taken at three film locations.

Hydrogen Content

This increase in microstructure is likely, also, a consequence of non-conformal deposition of the a-Si:H top layer. In instances where increases in microstructure result in a uniform increase porosity throughout the film volume, typically a measurable increase in hydrogen content is observed [89, 117, 118]. Figure 5.5 shows the hydrogen content for the seeded films shown in figure 5.4, as measured by FReS. Hydrogen content is relatively constant at ∼12% for the range of seed concentrations over which R* is shown to increase. These observations suggest that the medium range disorder induced is a localized effect, likely concentrated near the seed plane.

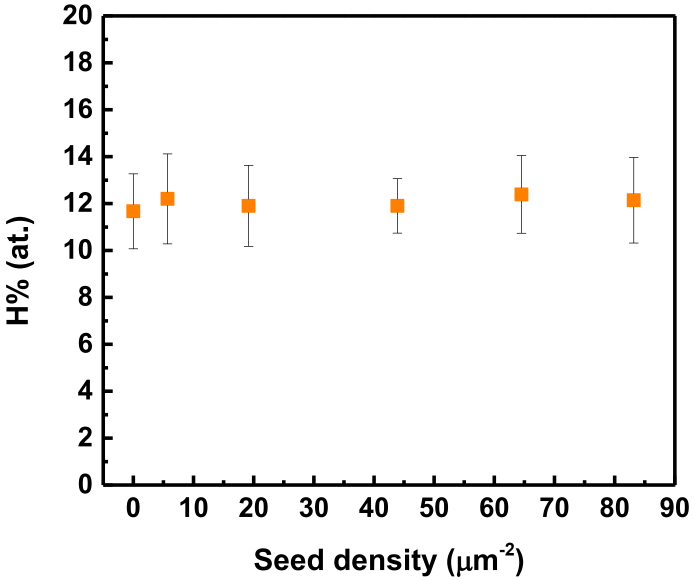

Figure 5.5: Hydrogen content vs. seed density for the 100 *nm* films shown in figure 5.4, as measured by forward recoil spectroscopy (FReS). Hydrogen content is relatively constant over the range of seed densities that microstructure was observed to increase. This suggest the observed increases in microstructure is a consequence of the local geometry of the seed plane, and not a change in film stoicheometry.

Porosity at the Seed Plane

Figure 5.6 (a) shows cross-sectional SEM image of the seed plane region of a 100 nm thick film containing a single seed layer, with a concentration of approximately 6 $/\mu m^2$. The top layer of a-Si:H film is seen to form a "conical" region that extends upward from the base of each seed crystal, indicating the region of influence of the seed plane layer on the top layer layer of film. Figure 5.6 (b) shows a closer, cross-sectional TEM image of the top layer region surrounding a seed crystal. Near the base of the conical region (outlined in red), nano-scale cavities can be seen, indicative of the microstructural defects concentrated near the seed plane.

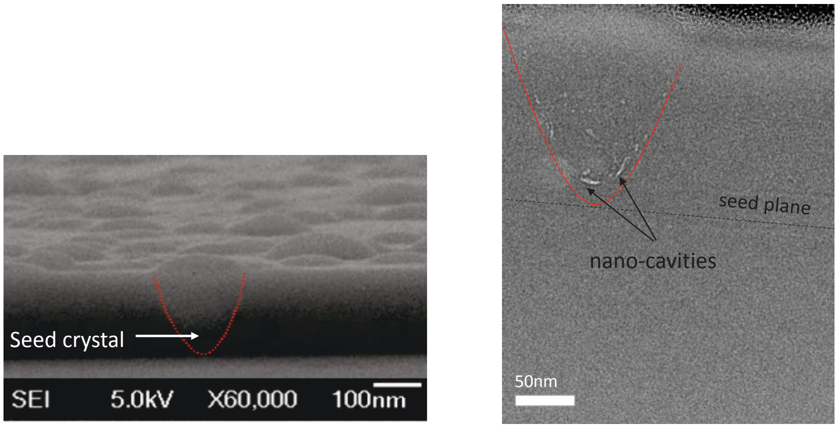

(a) (b)

Figure 5.6: (a) Cross-sectional SEM image of the a-Si:H top-layer of an as-grown film containing a plane of seed crystallites. The dome regions on the film surface indicate the top-layer a-Si:H film deposited over individual seed crystals. The red line indicates the region of disorder influence the seed crystal exhibits on the deposition of the top film layer. (b) Cross-sectional TEM image of an as-grown seeded film containing two layers of seed crystals. Porous, nano-cavity rich regions can be seen adjacent to the base of each conical regime (red), where seed crystals are located. Images taken by Andrew J. Wagner.

5.3.3 Textured substrates

The observed increases in structural disorder with seed concentration, in as-deposited films, can possibly explain the resulting decreases in grain growth rate during annealing shown in 5.2. The topography of the seed plane is capable of generating defects on the short and medium range scale that have been linked to suppression of crystallization in other reports. In order to explore this hypothesis further, equivalent 100 *nm* seeded samples were deposited on substrates "textured" to various degrees to simulate the topography (and thus the disorder) of the seed plane. Samples were then annealed at 625 °C and crystallization rates were compared by Raman crystal fraction measurements.

Textured Substrate Deposition Process

In order to simulate the topography provided by the seed plane, substrate texture was generated by depositing various concentrations of seed crystals directly onto the substrate surface, prior to film deposition. These "texture-layer" crystals were then coated with 10 *nm* of silicon dioxide grown from PECVD at 150 °C. Since SiO2 is stable for temperatures up to 1100 °C, this barrier layer prevents seed crystals in the texture layer from crystallizing the top layer film during annealing. Top layer films consisted of a seeded film consisting of 100 *nm* of a-Si:H deposited at 5 W, 100 $mTorr$ and 250 °C, with a single seed layer, 50 *nm* below film surface, having a seed concentration of $\sim 6/\mu m^2$. Three separate samples were deposited, distinguished by "low", "moderate", and "high" levels of substrate texturing. Figure 5.7 shows a schematic of the substrate texturing and film deposition process, along with AFM images of each substrate texture prior to film deposition.

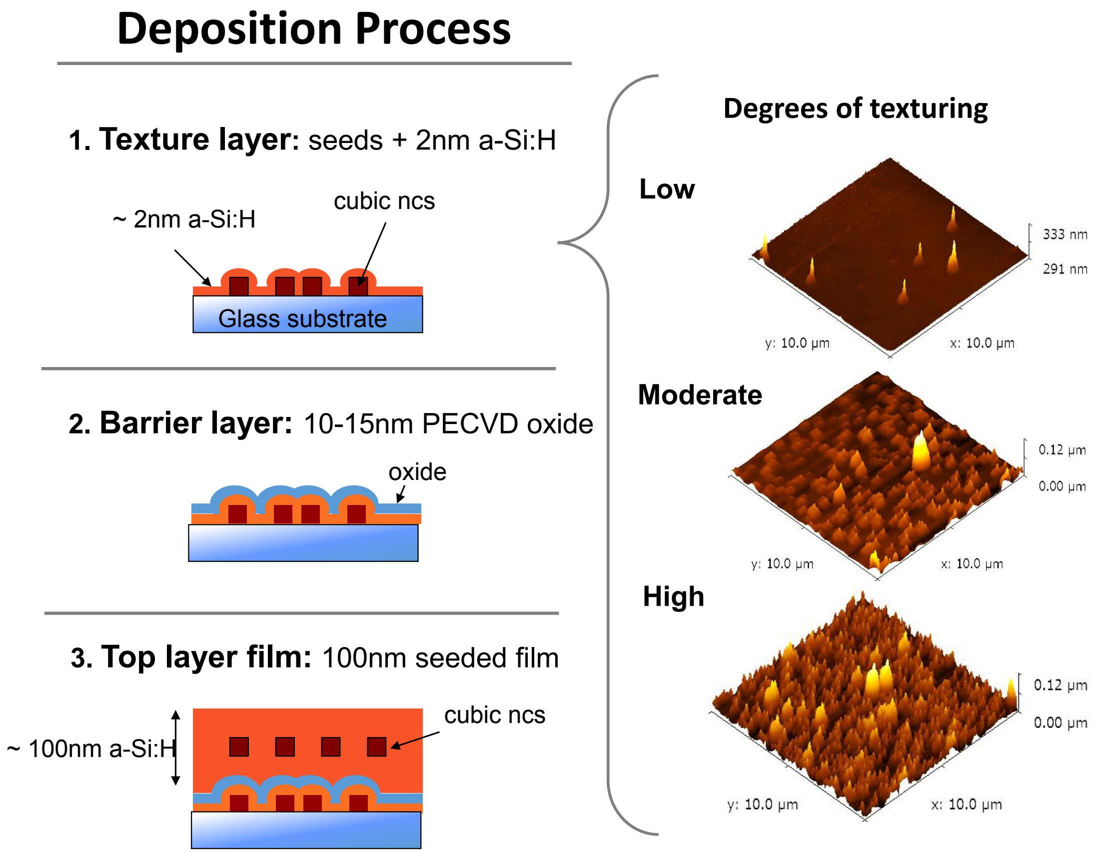

Figure 5.7: Schematic representation of the deposition process used to study the effect of film disorder on crystallization rate in seeded films. Step 1: Corning glass substrates were coated with seed crystals to achieve one of three degrees of texture: “low”, “moderate” or “high”. AFM images of each type of texture layer are shown on the right. 2: Texture layer is coated with a 10 nm to 15 nm barrier layer of PECVD grown oxide to prevent crystallization from the texture layer. 3: A single, 100 nm, seeded film is deposited with seed density of $\sim 6/\mu m^2$.

Textured Substrate Crystallization Kinetics

Films were subsequently annealed at 625 °C in a quartz furnace under nitrogen ambient. Crystal fractions calculated at regular time intervals by Raman spectroscopy using the techniques outlined in Chapter 4. Figure 5.8 shows the resulting progression of crystal fraction with anneal time for each substrate texturing. Crystallization curves are observed to monotonically shift to later times with increasing substrate texturing. It is clear from this result that the disorder generated by the seed-plane topography hinders the crystallization rate of the surrounding film in a manner consistent with the trend observed in figure 5.1. This suggests that the observed decrease in crystallization rate with increasing seed density is a result of film disorder, likely due to defects associated with top-layer deposition over the topography of the seed layer.

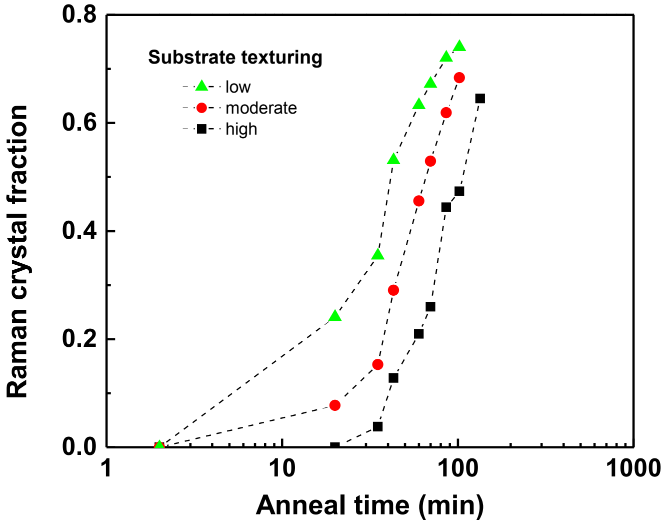

Figure 5.8: Crystallization curves of 3 seeded films of equivalent structure, grown on substrates having different degrees of texturing, and annealed at 625 °C. Films were grown by the process outlined in figure 5.7 on top of substrates exhibiting either “low”, “moderate”, or “high” degrees of texturing. Results show a reduction in crystallization rate with substrate texturing.

5.4 The Effect of Varying Seed Density on Final Grain Structure

In order to quantify the ability of seed crystals to modify the final grain structure of resulting poly-crystalline (poly-Si) films, comparisons of relative grain sizes were conducted following annealing. Grain size comparisons were made by analysis of the poly-crystalline Raman signature, along with electronic transport properties. Comparisons were made for several films of varying seed density, after films achieved “complete crystallization”, defined as the annealing stage at which a crystal fraction maximum is achieved.

5.4.1 Relative Grain Size

The transverse optical (TO) component of the Raman signature of poly-crystalline silicon is a common method of providing information on relative grain size of poly-crystalline films. The width of the crystalline TO Raman peak between 515 cm^{-1} to 520 cm^{-1} has been demonstrated to have a direct correlation to grain size [119]. Specifically, relatively smaller grain sizes have been demonstrated to exhibit larger TO peak widths due to a progessive relaxation in momentum conservation. Figure 5.9 shows c-Si TO widths for several of the 200 nm thick samples shown in figure 5.2, following annealing to complete crystallization at 650 °C. Spectra were taken at five locations across the surface of each film. The dashed reference lines corresponds to the range of average TO widths measured for three unseeded films, following complete crystallization at the same temperature.

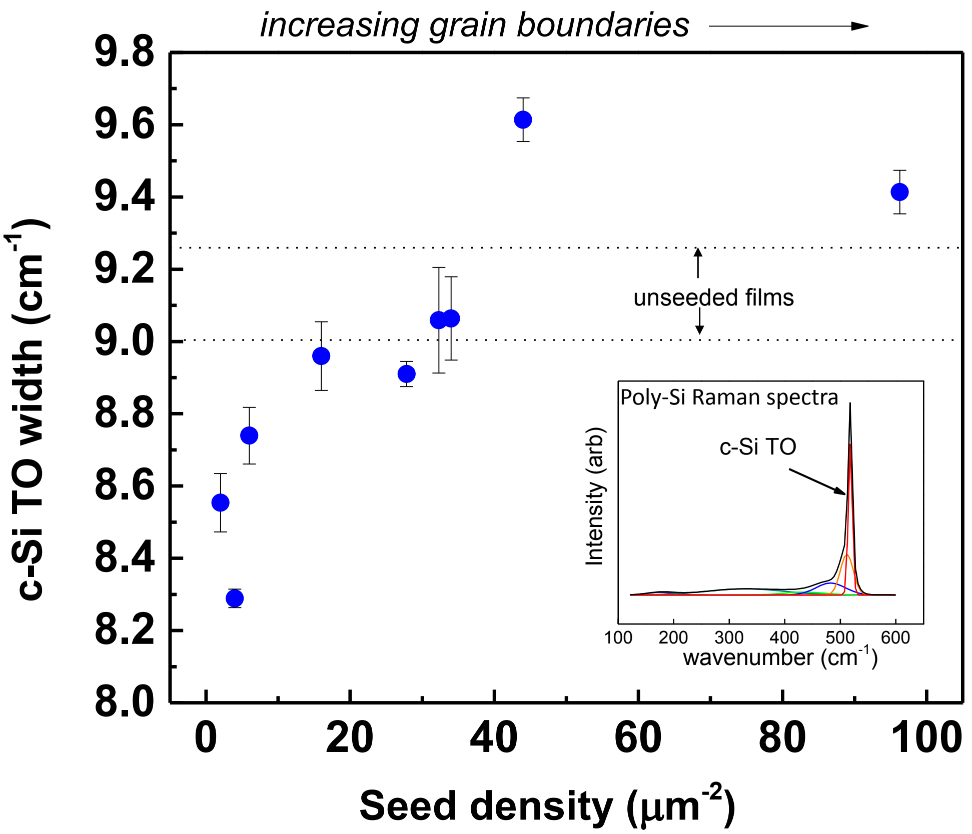

Figure 5.9: Raman c-Si TO peak width of several 200 nm thick seeded films after complete crystallization at 650 °C. Peak width increases with initial seed density, indicating a decrease in average grain size. An example Raman spectra of a fully crystallized, poly-Si sample is shown in the inset.

The increase in peak-width with seed density indicates a shrinking grain size, consistent with the intention of controlling final grain structure by seed population. It is interesting to note that seed densities greater than $\sim 20/\mu m^2$ result in relatively larger TO widths than films crystallized from unseeded material. This suggests a necessary upper limit to initial seed density, beyond which the grain size of the resulting, fully-crystallized, film decreases below the average grain size achievable by an unseeded film.

5.4.2 Electronic Transport

To analyze how these final grain structure variations translate into device performance, electronic transport measurements were performed on fully crystallized samples of various initial seed concentrations. Descriptions of electronic transport in poly-Si differ from those used to characterize wafer-based silicon materials, due to the necessary consideration of grain boundary regions. Poly-Si grain boundaries are comprised mainly of amorphous-like regions composed of strained and dangling bonds. These defect-rich regions translate into electronic states residing between the valence and conduction bands. Charge accumulation at grain boundary trap states results in a potential barrier between adjacent grains on the order of a 50 meV to 500 meV [120–122]. The depletion width of an inter-grain potential barrier extends into the adjacent grains, effectively reducing the amount of free carriers available for intergrain transport. This results in the occurrence of one of three primary modes of electrical conduction in un-doped poly-Si, depending on grain size, and grain boundary trap density. Figure 5.10 illustrates the band diagram associated with each mode, along with corresponding conduction formulas.

Figure 5.10(a) depicts barrier-limited transport, which occurs in films with small enough trap density and/or large enough grain sizes that a significant free carrier population exists within grain regions. Partial depletion occurs for relatively smaller grain sizes and/or higher trap densities, resulting in a majority of carriers residing in mid-gap trap states (Figure 5.10(b)). Complete depletion occurs in films with relatively small grain sizes or large grain boundary trap densities, when the grain boundary depletion width extends to dimensions on the order of the average grain size, thus depleting grain regions of free carriers (Figure 5.10(c)).

For both complete and partial depletion conditions, the Fermi level is fixed near mid-gap due to the large density of trap states. Conduction is subsequently limited by thermionic emmission of carriers from trap states, resulting in an conductivity activation energy of approximately half the mobility gap (E_g). For barrier limited transport, a significant population of free carriers resides in extended states of the grain region, and the activation energy for conduction is reduced to the barrier height imposed by the grain boundaries.

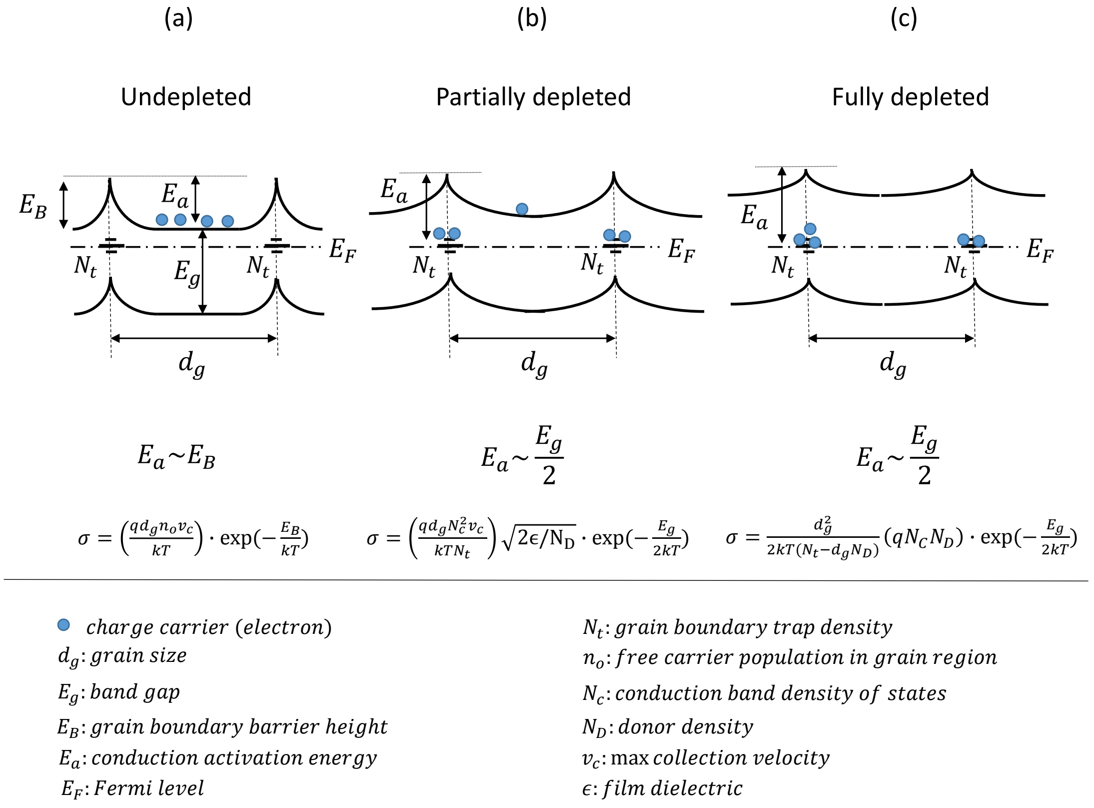

Figure 5.10: Energy band diagram depiction of three primary modes of conduction in poly-Si, after [120]. (a) Barrier limited transport. (b) Partially depleted transport. (c) Fully depleted transport. Corresponding conductivity relationships are also shown, after [122].

It is important to note that each mode of conduction also shows a prefactor dependence on grain size, with partially depleted and barrier limited showing a positive, linear correlation with grain size. Subsequently, the mode of conduction for a set of samples with differing grain size can be inferred from the conductivity activation energy (E_A), the mobility gap (E_g), and the relative scaling of room-temperature conductivity with grain size. Measurements of each of these parameters were performed on several fully crystallized films in order to determine the effects of varying seed density on the mode of transport.

Dark Conductivity

The electronic transport properties of fully crystallized films were compared on the basis of dark (un-illuminated) electrical conductivity for samples annealed to complete crystallization from varying initial seed concentrations. Measurements were performed on 200 *nm* thick samples deposited with seed layers 100 *nm* below surface, having concentrations of approximately $\sim 6/\mu m^2$, $\sim 21/\mu m^2$, and $\sim 44/\mu m^2$. Following complete re-crystallization at 650 °C, 150 *nm* thick chromium contacts were evaporated onto the surface of each sample at several locations to form the device structure shown in the inset of figure 5.11.

The contact pattern formed consisted of 24 channels total, providing information on the uniformity of the transport properties across the entire sample. Each channel was 2 *mm* wide and 1 *mm* long to prevent the influence of small-channel contact effects. To reduce Schottky barrier effects on the current-voltage (I-V) characteristics, contacts were annealed at 450 °C for 30 *min* as suggested in [123]. Conductivity was first measured for each sample across all 24 channels, at room temperature, and used to compute a sample average. Activation energies were then estimated from temperature dependent conductivity measurements taken on a single channel near sample center. Conductivity was measured in the temperature range from 300 K to 450 K, in 1 K increments.

Figure 5.11 (a) shows the average room-temperature conductivity for each sample. Figure 5.11 (b) shows Arrhenius plots of conductivity with temperature for each sample, with corresponding activation energies. The average measured room-temperature dark conductivity is observed to decrease with increasing initial seed density, suggesting a reduction in grain size consistent with the results shown in Figure 5.9. Conduction activation energies were observed to be relatively constant, $\sim 0.63\ eV$ for all samples. These values are consistent with literature values for poly-Si and micro-crystalline silicon films [124,125]. However, measurements of the mobility gap were required to make more accurate assessments of the mode of conduction present.

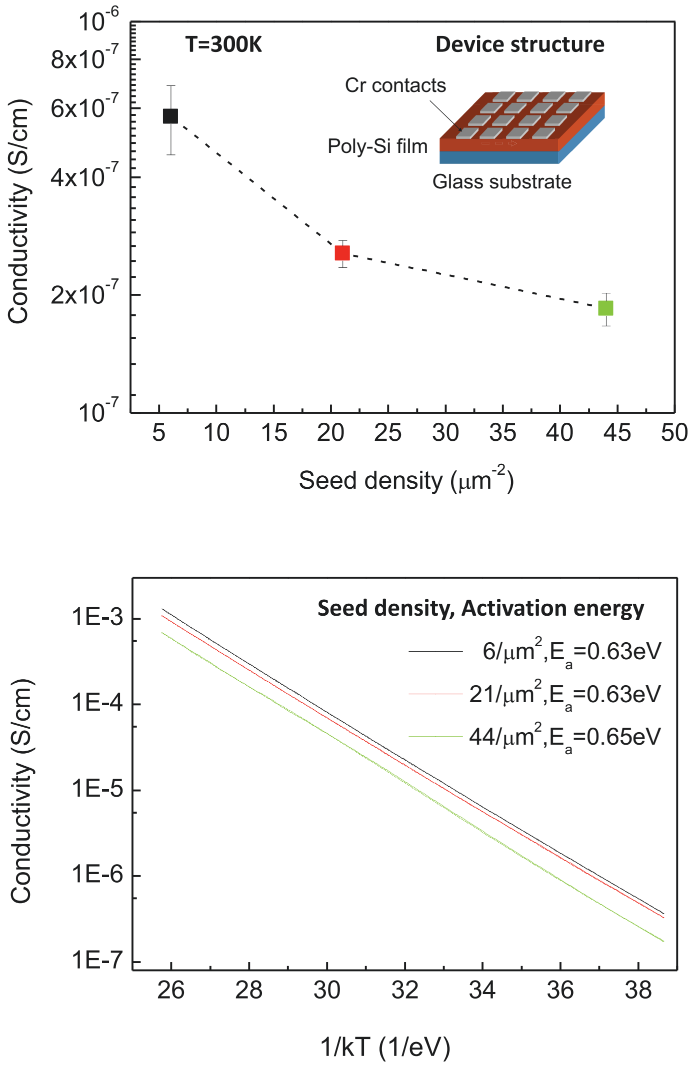

Figure 5.11: (a) Room temperature conductivity (un-illuminated) of three fully crystallized samples with as-deposited seed densities of $\sim 6/\mu m^2$, $\sim 21/\mu m^2$, and $\sim 44/\mu m^2$. Conductivity values and error bars reflect the average and standard error measured over all 24 conduction channels of the device structure shown in the inset. (b) Conductivity of each sample as measured from a single, centrally located device channel, over the temperature range from 300 K to 450 K. Corresponding activation energies are shown in the legend.

Mobility Gap

The mobility gap for fully crystallized films was found to be relatively constant over a wide range of initial seed densities, with an average value of $\sim 1.14\ eV \pm 0.07\ eV$, roughly twice the conduction activation energies measured in figure 5.11. Mobility gaps were approximated using "Tauc" plots of photo-absorption characteristics, shown in Figure 5.12, a method commonly used as an approximation of the band gap in semiconducting materials where the density of states is shaped by defect states [85, 93, 126]. Absorption data for each film was taken by the constant photo-current method (CPM), in the range of 1320 nm to 800 nm ($\sim 0.9\ eV$ to $1.5\ eV$). Band gap values for fully crystalline materials are reported to be $\sim 1.1\ eV$ in literature [127].

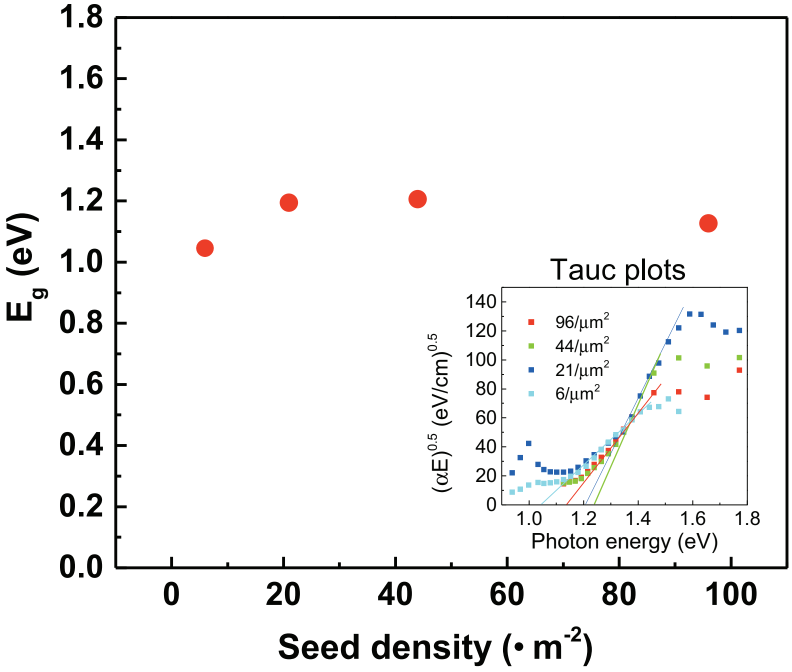

Figure 5.12: Mobility gap (E_g), for 200 nm thick, fully crystallized films annealed from various initial seed densities. Values were approximated as equivalent to the Tauc gap, estimated from Tauc plots of CPM photo-absorption, shown in the inset. The Tauc gap was taken as the x-intercept of the linear portion of the plot shown, for absorption coefficients above $10^3\ cm^{-1}$ [85].

Table 5.1: Summary of electronic transport properties of fully crystallized films of varying initial seed density. $\sigma(300K)$ is dark conductivity averaged over 24 device channels, taken at room temperature. E_a is dark conductivity activation energy taken over a temperature range from 300 K to 450 K. E_g is mobility gap estimated from CPM measurements. Grain diameter values were estimated from seed density.

seed density (μm^{-2})	estimated grain diameter (nm)	$\sigma(300K)$ (S/cm)	E_a (eV)	E_g (eV)
6	426	5.7×10^{-7}	0.63	1.04
21	220	2.6×10^{-7}	0.63	1.19
44	151	1.85×10^{-7}	0.65	1.2

Table 5.1 summarizes the results of figures 5.11 and 5.12. In determining the mode of conduction present, it is necessary to note the relative conductivity between samples is approximately equal in scaling as the relative grain sizes estimated by initial seed density. Specifically, the ratio of room temperature conductivity between $\sim 6/\mu m^2$ and $\sim 21/\mu m^2$ seed density samples is approximately 1.9, and the ratio of estimated grain sizes between the same samples is roughly 2.2. Similarly, comparing the same values for $\sim 6/\mu m^2$ and $\sim 44/\mu m^2$ samples yields ratios of 2.8 and 3.1, respectively.

This scaling suggests a linear dependence between conductivity and average grain size, indicative of either the partially-depleted or barrier-limited transport modes shown in figure 5.10. However, the activation energy of conduction was observed to be approximately 0.64 eV ± 0.01 eV for all samples, which is roughly half the average mobility gap values observed in figure 5.12. This suggests the observed mode of conduction to be partially-depleted, meaning conduction in fully crystallized seeded films is limited primarily by trap states near the Fermi level. An increase in conductivity can subsequently be achieved by reducing the concentration of trap states in fully crystallized films. Reduction in trap density requires elimination of the primary grain boundary states responsible for increasing the depletion width.

The shape of the grain boundary density of states has been experimentally observed to be similar to that of amorphous silicon [120, 121], with an exponential tail of defect states diminishing toward mid-gap. However, unlike amorphous silicon, the limited long range order of the poly-Si grain structure results in a de-localization of many of the states residing near the band-tail regions [120]. Subsequently, charge carrier trapping is primarily associated with the localized, or dangling bond states residing near mid-gap. For this reason, a description of the grain boundary region consisting of a δ-shaped distribution of trapping states, centered near mid-gap, has been shown to reasonably approximate experimental conductivity results [122]. Thus, a reduction of carrier charge-trapping in fully crystallized films requires measures focused on a reduction of dangling bonds within grain boundary regions.

Hydrogen Treatment

The most common method of reducing dangling bond defects in poly-Si films is by injection of hydrogen into grain boundaries after crystallization. This is typically performed by exposing fully crystallized films to a hydrogen plasma at substrate temperatures between 25 °C to 450 °C [57, 128–130]. Hydrogen treatment was performed on the films shown in Figure 5.11 by exposing them to an argon and hydrogen discharge at a pressure of 400 millitorr and a substrate temperature of 200 °C. A 2:1 ratio of hydrogen to argon flow rates was used (40 *sccm*:20 *sccm*) and exposure time was 30 *min*. The addition of argon was found to be necessary to promote ionization of the hydrogen precursor. In order to prevent ion bombardment damage to existing device contacts, additional samples from the depositions of the devices shown in figure 5.11 were used to acquire "post-treatment", conductivity values. These samples were fully crystallized at 650 °C, exposed to the hydrogen discharge treatment, and Cr contacts were evaporated to make devices of the same structure shown in Figure 5.11.

Figure 5.13 shows the resulting hydrogen content of each film before and after undergoing hydrogen plasma treatment. The non-zero signal measured prior to plasma treatment is attributed to hydrocarbons adsorbed onto the film surface and into the surface oxide. For each film measured, the hydrogen content increases from below 2%, to values between 6% to 7% (at.).

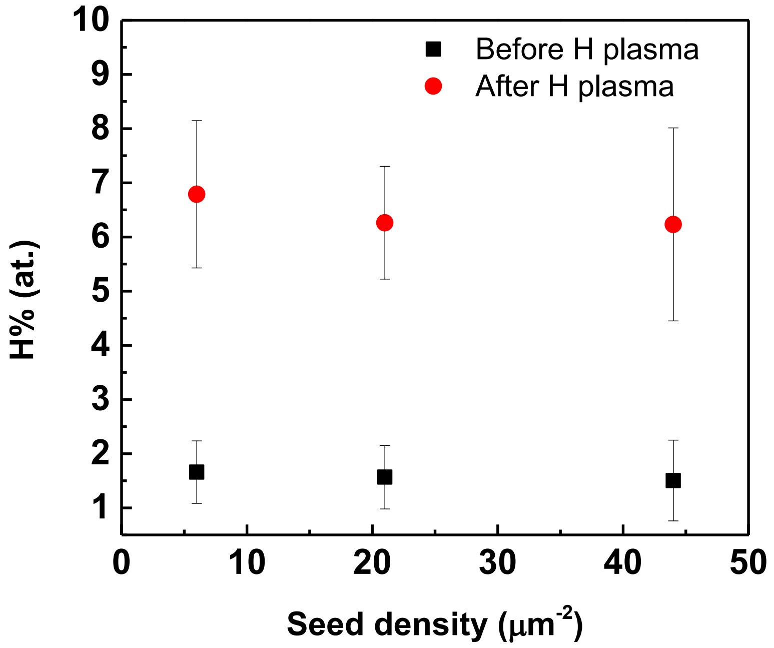

Figure 5.13: Hydrogen content (% at.) as measured by forward recoil spectroscopy (FReS) of fully crystallized samples before and after hydrogen plasma treatment. Samples were 200 nm thick, with initial seed densities of $\sim 6/\mu m^2$, $\sim 21/\mu m^2$ and $\sim 44/\mu m^2$.

These values are reasonable considering the final crystal fractions measured for each film by Raman were measured to be approximately 81%, 80%, and 78% for $\sim 6/\mu m^2$, $\sim 21/\mu m^2$ and $\sim 44/\mu m^2$, respectively. This suggests remaining quantities of amorphous grain boundary phase to occupy roughly 20% of the final film. The solubility limit of amorphous silicon has been reported to be near 40%-50% (at.), due to spinodal decomposition [131]. Assuming completely, amorphous grain boundary regions, this suggests hydrogen solubility limits between 7% to 9% (at.) for the films treated here. Following hydrogen treatment, room temperature dark conductivity and temperature-dependent conductivity were measured. Figure 5.14 shows the resulting conductivity measurements for fully crystallized films with ("H treated") and without ("untreated") hydrogen plasma treatment.

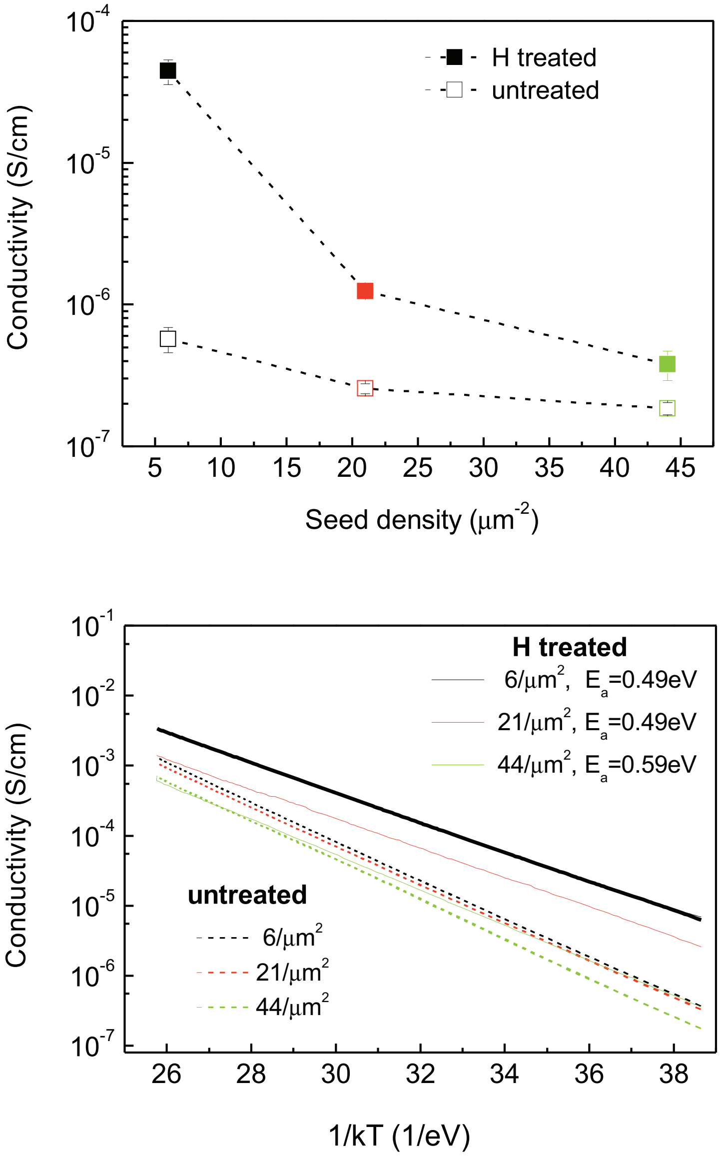

Figure 5.14: (a) Room temperature dark conductivity of fully crystallized films having seed densities of $\sim 6/\mu m^2$, $\sim 21/\mu m^2$, and $\sim 44/\mu m^2$. Hydrogen treated films are shown as solid symbols, with untreated films shown as open symbols. (b) Temperature-dependent conductivity for untreated (dashed lines) and H treated (solid lines) samples. Corresponding activation energies for H treated samples are shown in the legend.

The results indicate a clear improvement in conductivity following hydrogen plasma treatment. Table 5.2 provides a summary of the conductivity parameters from figure 5.2. It's interesting that this improvement is more significant for films crystallized from lower initial seed densities. This is likely due to a larger average grain size and a subsequently smaller number of grain boundaries. Since each film was exposed for equivalent time intervals, longer exposure times are likely required to saturate the relatively larger quantity of grain boundary defects in higher seed density films. This is further evidenced by the observed changes in conduction activation energy between untreated and treated samples. Activation energy is reduced below mid-gap levels to approximately 0.49 eV for $\sim 6/\mu m^2$ and $\sim 22/\mu m^2$ density films following H treatment, while the $\sim 44/\mu m^2$ film exhibited a minor reduction to 0.59 eV. For $\sim 6/\mu m^2$ and $\sim 22/\mu m^2$ samples, this suggests it is likely that trap density was reduced to a significant enough degree to transition from partially depleted, toward barrier limited transport.

Table 5.2: Summary of electronic transport properties of fully crystallized films of varying initial seed density, with (H treated) and without (untreated) hydrogen plasma treatment.

seed density (μm^{-2})	$\sigma(300K)$ untreated (S/cm)	$\sigma(300K)$ H treated (S/cm)	$\frac{\sigma(300K)Htreated}{\sigma(300K)untreated}$ — —	E_a untreated (eV)	E_a H treated (eV)
6	5.7×10^{-7}	4.42×10^{-5}	77.4	0.63	0.49
21	2.6×10^{-7}	1.24×10^{-6}	4.9	0.63	0.49
44	1.85×10^{-7}	3.78×10^{-7}	2.1	0.65	0.59

5.5 conclusions

The effect of varying initial seed crystal concentration, or “seed density”, has been demonstrated on both crystallization kinetics, and final grain structure quality. Specifically, crystallization rate was observed to decrease with increasing initial seed concentration. This is believed to be due to an increase in film disorder, induced by the geometry of the incorporated seed crystals, resulting from a-Si:H top layer deposition over the texture of the seed plane. Crystallization studies of intentionally textured substrates support this hypothesis. The final grain size of seeded films following annealing was seen to decrease with increasing seed density, as measured by the TO width of fully crystallized Raman spectra. Electrical conductivity measurements reflect a similar trend, indicating final grain structure can be tuned by initial seed concentration to a degree that translates into beneficial device properties. The mode of electrical conductivity in fully crystallized films was identified, and a method for improving transport properties to a more favorable mode was outlined, through a post-anneal hydrogen plasma treatment process.

Chapter 6

The Effect of Seed Crystal Shape on Crystallization Kinetics

6.1 Introduction

The effect of seed crystal shape on crystallization kinetics was studied by varying plasma conditions within the seed crystal reactor tube. Specifically, a parameter space of varying RF power was explored, due to observations of a potentially novel crystallization mechanism occurring in films containing seed crystals grown at powers higher than 140 W. These observations are believed to be associated with changes in seed crystal shape that occur at relatively higher synthesis powers, and were found to demonstrate further enhancements in crystallization rate relative to cubic seed crystal films.

6.2 Void-induced Crystallization

It was observed in heated stage TEM that films containing seed crystals synthesized at powers greater than 140 W or under conditions with more effective power matching, exhibited significantly different mechanisms of crystallization. Figure 6.1 shows images of 150 W seeded films during annealing at 640 °C. Void-like structures, elliptical in shape, and roughly 10 nm to 30 nm in long axis dimension, can be seen to form at the interface of the seed crystals. After a period of time, these void regions proceed to travel through the film, leaving a crystalline wake.

Several HSTEM observations have shown void motion to exceed radial grain growth rate from seed crystals by a factor of 2 or more for anneal temperatures between 600 °C-650 °C [81].

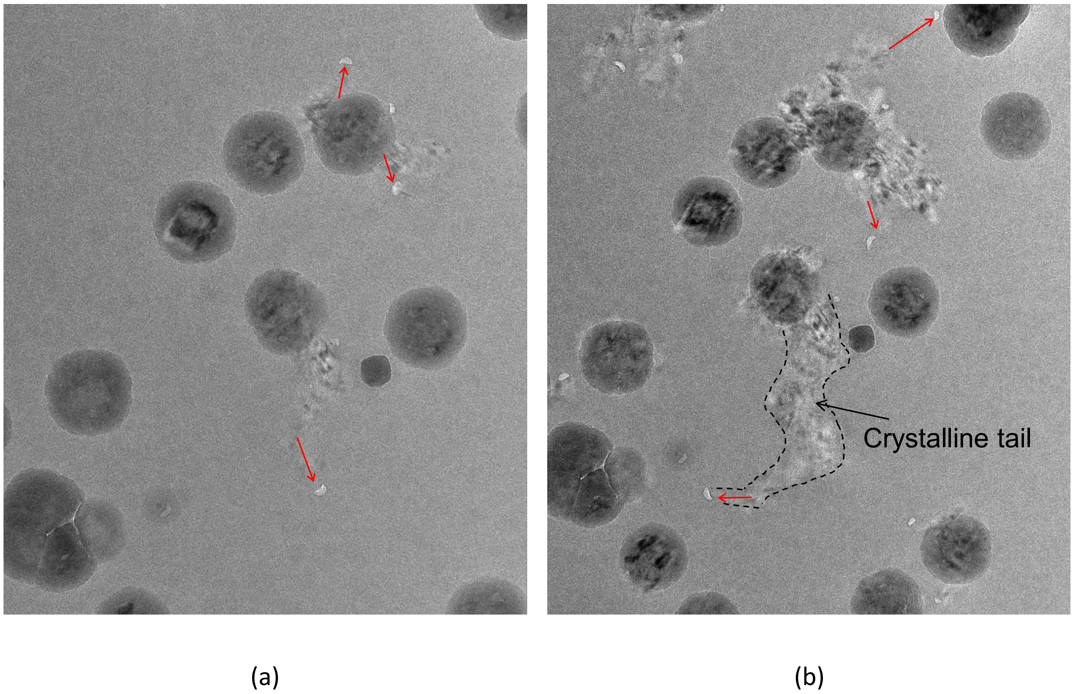

Figure 6.1: TEM images taken in-situ, during annealing of a 100 *nm* seeded film at 640 °C at (a) ∼7 *min* and (b) ∼15 *min*. Seed crystals were synthesized at an RF power of 150 *W*. Void regions (red arrows) are seen to propagate from most seed crystals, each leaving a crystalline wake. After ref [81].

6.2.1 Void Kinetics

Previous studies by Anderson [81] determined void-induced crystallization (VIC) to be driven by surface diffusion of amorphous silicon atoms from the frontal amorphous region to the crystalline tail region along the inner void surface. Figure 6.2 shows an illustration of the mechanism of void propagation proposed by Anderson. The activation energy associated with diffusion along free surfaces in amorphous silicon was measured by Smets *et al.* to be approximately 0.77 eV to 1.05 eV [88]. The lower activation energy of surface diffusion, relative to the activation energy from grain growth from the seed crystals of 2.7 eV, was originally thought to facilitate the higher rate of void motion. However, recent investigations by Wagner *et al.* [132] observed the rate of void propagation to increase with void size, an effect attributed to the development of twin-defects at the crystalline boundary of larger voids. Twin-enhanced grain growth

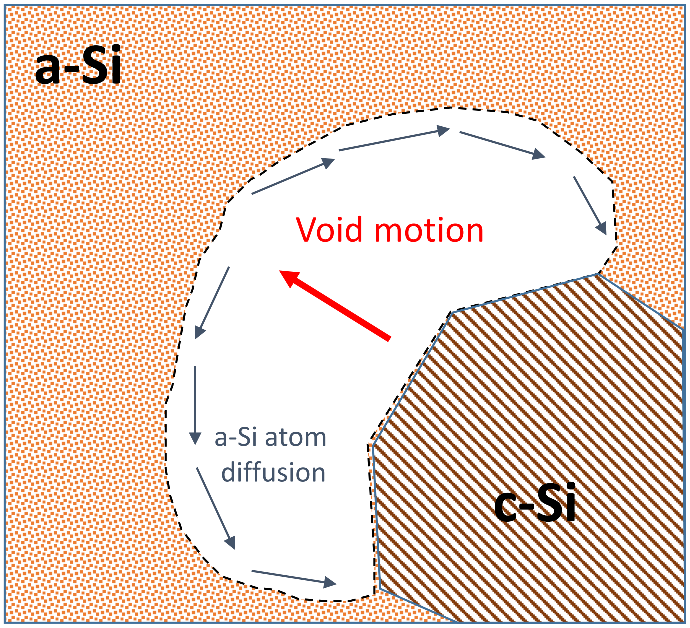

Figure 6.2: Visual of the surface diffusion-driven mechanism of void propagation originally proposed by Anderson [81]. Blue arrows represent diffusion of silicon atoms from the amorphous frontal region to the crystalline tail, along the inner void surface. The resultant void motion is indicated by the red arrow.

6.2.2 Void formation

Deposition Shadowing

These mobile void regions are believed to be formed by a coalescence of smaller, porous regions near the seed plane, occurring during early anneal stages. These smaller, nanoscale vacancies likely originate from the shadowing effect discussed in chapter 5. As was shown in Figures 5.6 and 5.4, a significant degree of porosity was observed to occur near the seed plane, even for films containing seed crystals synthesized at an RF power of 140 W. However, this shadowing effect is much more pronounced for films containing seeds synthesized at RF powers of 150 W, an effect believed to be due to a modification of seed crystal geometry. Figure 6.3 (a) shows TEM image comparisons of seed crystals grown at 140 W and 150 W, demonstrating the observed change in seed crystal geometry toward a higher-faceted, octahedral structure.

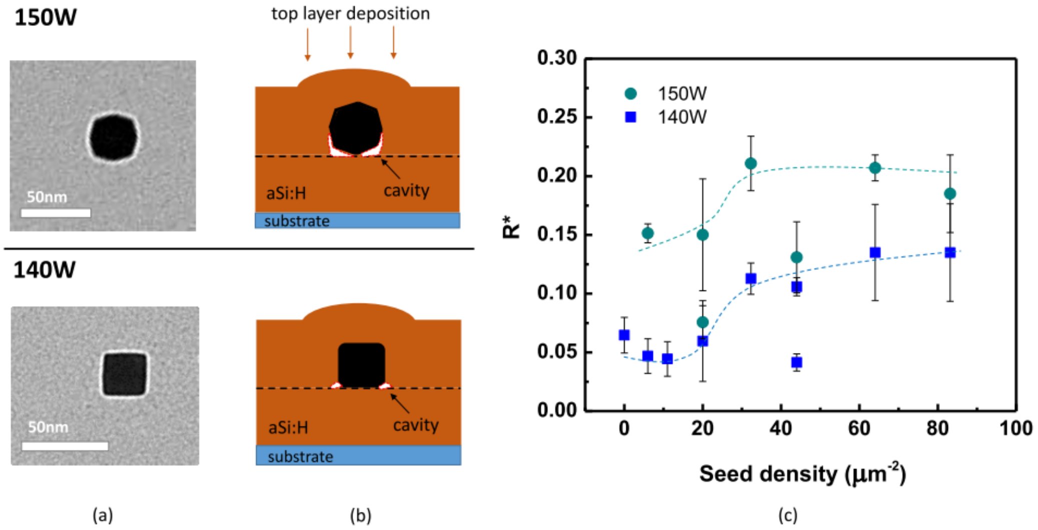

Figure 6.3: (a) TEM images of seed crystals synthesized at RF powers of 140 W and 150 W. (b) Visual depiction of film cross-section and shadowing following top-layer deposition over each seed shape. (c) Comparison of microstructure with varying seed density for films containing seed crystals grown at each power.

Figure 6.3 (b) shows a schematic representation of the shadowing effect proposed to occur during deposition over seed crystals grown at 140 *W* and 150 *W*. The higher faceting of 150 *W* seed crystals results in a lower area of surface contact with the underlying a-Si:H base-layer, resulting in the formation of cavities during top-layer deposition. These cavities result in a greater degree of porosity near the seed plane, as is reflected by an the observed increase in microstructure shown in Figure 6.3 (c). For most of the seed densities compared, microstructure of films containing 150 *W* seed crystals is nearly double that of films containing 140 *W* seed crystals.

Cavity Coalescence

For all samples in which VIC was observed, voids were observed to appear near the seed perimeter during early anneal stages, prior to the emergence of observable grain growth. Figure 6.4 shows a comparison of cross-sectional TEM images of films in both the as-deposited state, and following a 15 *min* anneal at 650 °C. A void is seen to appear on the right side of the conical perimeter of the annealed sample, indicative of the cavity coalescence believed to occur in this region. It is believed that the time scales associated with void formation correspond to the time required for smaller vacancies to coalesce into larger cavities. Similar effects have been reported in hydrogen effusion experiments, where nano-vacancies have been shown to coalesce and propagate from a-Si:H films at temperatures between 450 °C to 600 °C, in time scales of 15 *min* to 60 *min* [134–136]. This coalescence can be potentially explained in the context of free energy minimization, due to the lower energy associated with internal surfaces of low radius of curvature. The relatively higher curvature of smaller vacancies results in higher energy, meta-stable regions of film capable of collecting into larger cavities with lower curvature [137].

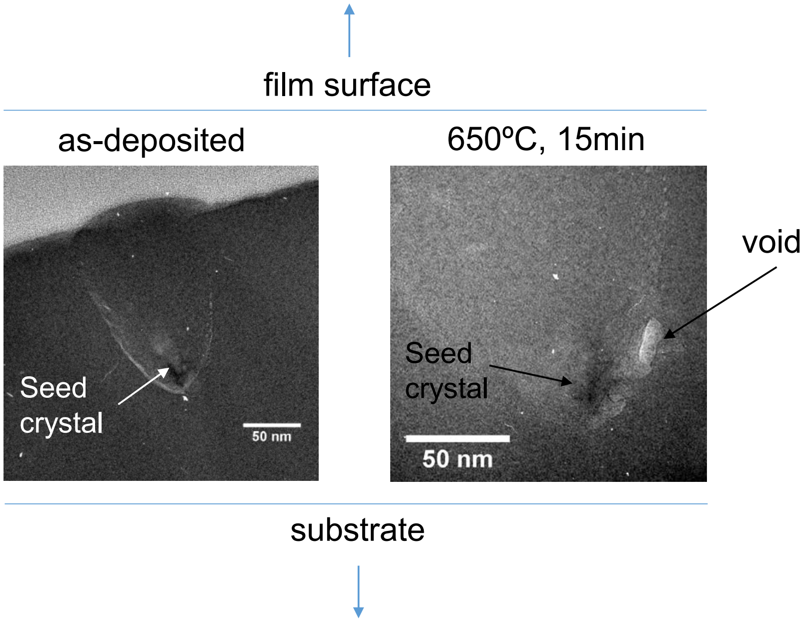

Figure 6.4: Cross-sectional TEM image of a 100 *nm* thick seeded film as-deposited (left) and after 15 *min* of annealing at 650 °C (right). The embedded seed crystal is identified by the dark region at the base of the conical regime. Following annealing, a large void is seen to appear on the right side of the conical perimeter.

6.3 The Effect of Particle Synthesis Power on Film Crystallization Kinetics

In order to further investigate the effect of particle shape on crystallization kinetics, several films were annealed containing seed crystals synthesized at various RF powers. Specifically, powers above 140 W were utilized with the intention of producing shape modifications that would potentially translate into measurable changes in crystallization rate. Each sample was deposited with a single mono-layer of seed crystals synthesized using the procedure outline in 3.1.3, with varying RF powers of 140 W, 150 W, 160 W, and 170 W. Surrounding a-Si:H films were 100 nm thick, deposited at an RF power of 5 W, a pressure of 100 $mTorr$, and a substrate temperature of 250 °C.

6.3.1 Seed Crystal Shape

Figure 6.5 shows TEM images of the resulting seed crystals for each RF power, with various shape profiles labeled for clarity. A distinct transformation from cubic (type I) to a higher faceted, rounded cubic (type II) profile occurs when synthesis power is increased from 140 W to 150 W. Similar shapes are observed at powers of 160 W and 170 W, with the additional presence of larger cubic-like particles, and several particles exhibiting hexagonal profiles (type III).

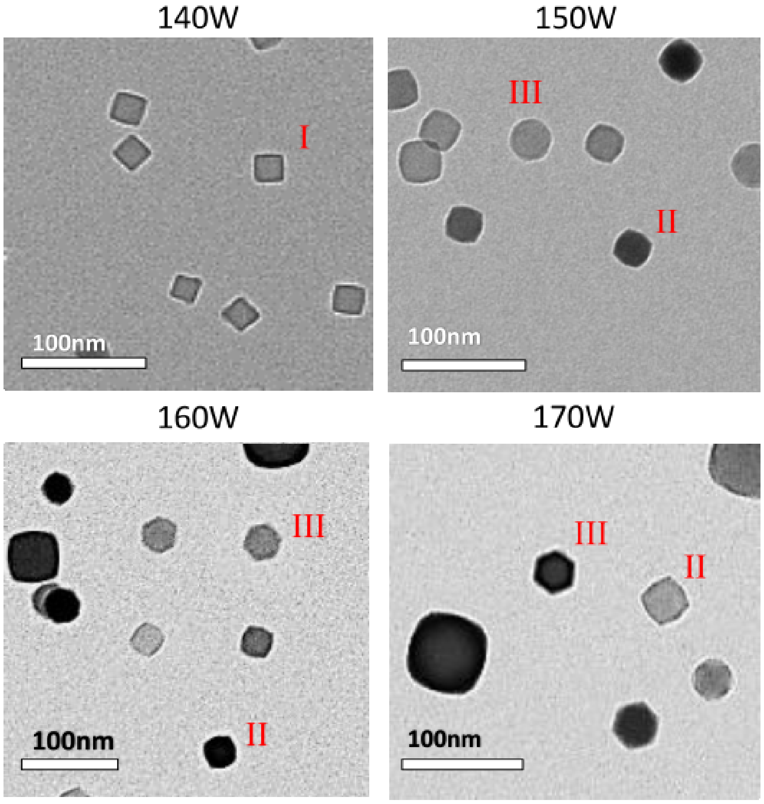

Figure 6.5: TEM images of seed crystals grown using the procedure outlined in section 3.1.3, with varying RF powers. Profile shapes were observed to transform from cubic (type I) at 140 W, to either a rounded cube (type II) or hexagonal (type III) profile of a cuboctahedral structure.

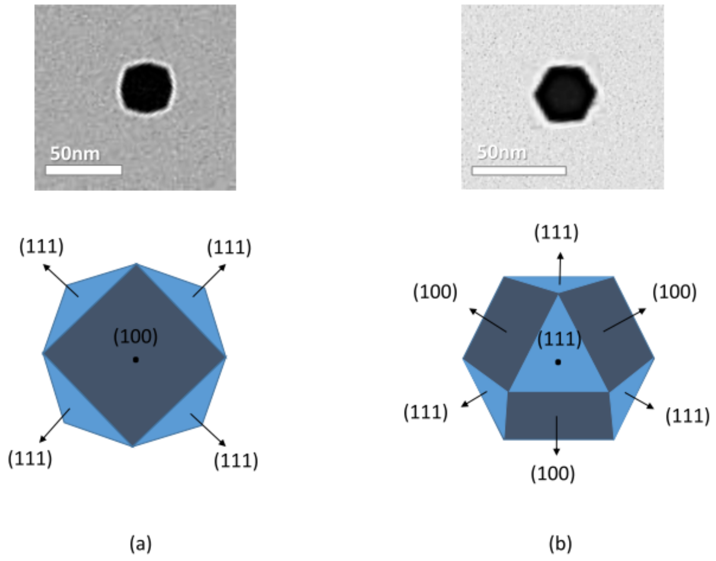

Figure 6.6: Schematic of the two primary shape outlines of the cuboctahedron shape with corresponding silicon lattice orientations and observed TEM equivalents. Figure a) depicts the (100) orientation resulting in the rounded cube outline visible in the above TEM image of a seed crystal grown at 150 W, also marked as type "II" in figure 6.5. Figure (b) depicts the (111) orientation resulting in the hexagonal outline visible in the above TEM image of a seed crystal grown at 170 W, also marked as type "III" in figure 6.5.

As figure 6.6 illustrates, a single "cuboctahedron" geometry is capable of producing profile shapes of both type II and III, when oriented relative to it's surface normals. This is interesting, considering tight-binding models, by See et al. [138], of silicon particle formation have predicted the cuboctahedral geometry to be a stable configuration for hydrogen terminated nano-crystals. Moreover, these studies determined that square (dark blue) and triangular (light blue) faces correspond to (100) and (111) orientations, respectively. Comparing the primary cuboctahedron shape profiles to high-resolution TEM images of particles grown at elevated powers, Figure 6.6(a) demonstrates the profile of a normal to the (100) cuboctahedron surface closely approximates the type II profiles seen in figure 6.5. Similarly, Figure 6.6(a) demonstrates that the profile normal to the (111) cuboctahedron surface can be seen to approximate type III profiles.

Consequently, it is believed that a majority of the shape profiles observed at powers above 140 W are a result of different orientations (either (111) or (100) oriented) of the same cuboctahedral geometry.

The precise mechanisms linking this shape transformation to plasma synthesis parameters is unknown. However, insights can potentially be drawn from earlier studies on the synthesis of cubic seed crystals in this particular reactor. For instance, studies by Bapat et al. [95] observed interesting transformations in particle structure at several locations, with respect to the nano-crystal plasma discharge region. Specifically, it was observed that particles exhibited more spherical, amorphous-like structures, approximately 300 nm in diameter, in regions upstream of the plasma discharge. These particles densified into $\sim$100 nm poly-Si particles near the upstream edge of the discharge, eventually becoming 30-50 nmm single crystals of cubic shape.

It has been suggested that this transformation is a result of etching, occurring from an increased bombardment of hydrogen ions upon entering of the discharge region [99]. Experiments by Sasaki and Takada [139] demonstrated hydrogen etching rates of wafers to be 1.5 times higher in (100) orientations relative to (111) orientations. This was argued to explain how cubic, (100) faceted structures could emerge downstream from relatively larger spherical, (111) faceted structures [99]. In the context of higher-faceted geometries, it is conceivable that either an over-etching of cubic (111) corner regions, or an under-etching of (100) faces could potentially result in the cuboctahedron shapes observed here. However, etching alone is unlikely to explain the transformations observed, as the transition from amorphous to single-crystal particles requires significant thermal input, as is typically supplied by ion and radical surface reactions.

It has also been suggested that hydrogen termination plays critical role in the stability of different particle geometries. For instance, simulations by Hawa *et al.* have shown that the cubic shape is more energetically favorable for silicon nano-crystals having full hydrogen surface termination. In the instance of a bare particle surface, however, a higher-faceted shape was determined be more stable. Subsequently, the stability of the cuboctahedral shapes observed at higher powers can potentially be rationalized by a lower hydrogen coverage. Lower hydrogen coverage could potentially occur at higher powers due to an increased plasma density and subsequently increased ion flux, leading to hydrogen abstraction, and/or hydrogen desorption from surface heating.

6.3.2 Microstructure

FTIR spectra were compared for each film prior to annealing to compare relative degrees of microstructure. As Figure 6.7 displays, a significant shoulder region near 2100 cm^{-1} emerges for films containing seed crystals synthesized at powers above 140 W, indicative of a larger degree of clustered silicon-hydrogen bonds associated with film porosity. It is interesting to note the strong overlap in spectra for 150 W, 160 W and 170 W samples. This suggests a similar degree of shadowing is present for each film, regardless of the presence of the larger particles observed in 160 W and 170 W films. Furthermore, due to the cubic-like shape of the larger particles observed in 160 W and 170 W, this suggests particle shape to play a more significant role than particle size in affecting film disorder on the medium-range scale.

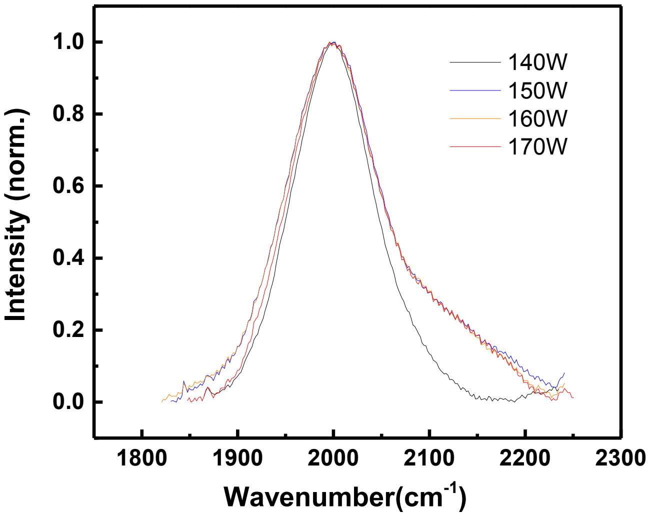

Figure 6.7: Normalized FTIR spectra of 100 nm films containing seed crystals grown at RF powers of 140 W, 150 W, 160 W, and 170 W. The emergence of a shoulder near 2100 cm^{-1} for 150 W to 170 W samples indicates an increase in microstructure. The increased microsturcture is likely due to an increased shadowing effect during top layer deposition, as a result of the higher-faceted shapes exhibited in seed crystals grown at higher powers.

6.3.3 Size Distribution

Prior to annealing, it was desired to ensure that average seed crystal density and size were relatively similar for each synthesis power. Due to the findings of chapter 4, in which crystallization rate was observed to have a nonlinear dependence on seed density, it was desired to compare samples with seed densities similar to within 1 $/\mu m^2$, in order to avoid the potentially confounding effects of seed shape and seed density. Subsequently, size distributions were compared for each synthesis power, acquired from AFM topography scans of 100 μm^2 film surface areas. Figure 6.8 a) shows seed crystal size distributions for each power, with dashed baselines added for a zero-count reference. Distributions are similar for 140 W and 150 W seed crystals, with an average diameter of 32 nm ± 2.5 nm and 31.7 nm ± 3 nm, respectively. Both 160 W and 170 W size distributions exhibit an asymmetrical broadening toward slightly larger average

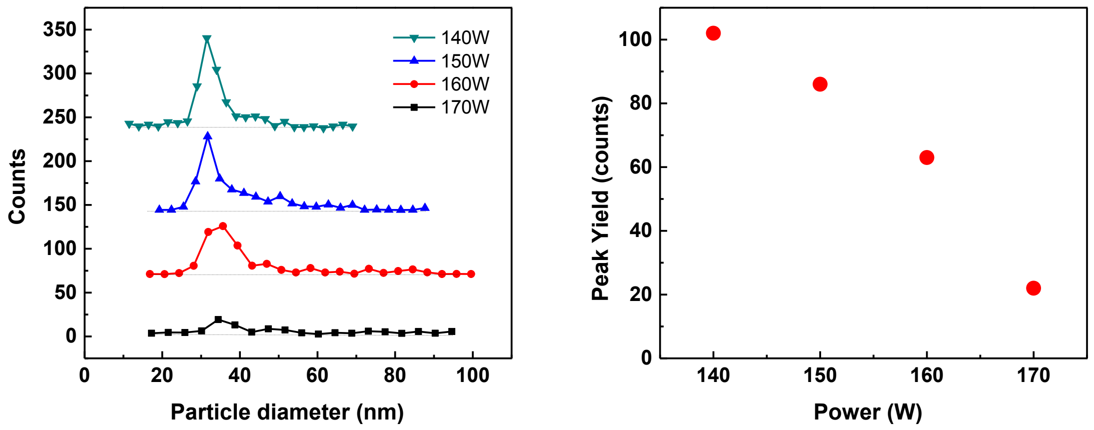

(a)

(b)

Figure 6.8: (a) Seed crystal size distributions adapted from AFM topography data for each 100 nm film, over a 10 μm x 10 μm area. (b) Seed crystal counts corresponding to the peak of each distribution from (a).

Interestingly, this broadening is accompanied by a decrease in peak yield with increasing power, with the most significant decrease occurring between 160 W and 170 W. This is potentially due to the presence of larger particles growing at the expense of smaller particles within the plasma discharge. The resulting aerial seed densities from each sample were calculated by integrating each distribution from 20 nm to 100 nm, and dividing by the AFM measurement area. This resulted in aerial seed densities of approximately 3.4 $/\mu m^2$, 2.6 $/\mu m^2$, 2.9 $/\mu m^2$, and, 1.1 $/\mu m^2$ for 140 W, 150 W, 160 W, and 170 W samples, respectively.

6.3.4 Crystallization Kinetics

Due to the relatively lower aerial seed density of 1.1 for the 170 W sample, only films containing 140 W, 150 W, and 160 W seed crystals were compared in annealing studies, to avoid confounding effects from seed density differences. Subsequently, 100 nm films containing seed crystals grown at 140 W, 150 W, and 160 W were prepared and annealed at regular intervals. The progression of crystal fraction was monitored by Raman spectroscopy following the techniques outlined in section 4.2. This was repeated for three different temperatures of 600 °C, 625 °C, and 650 °C. Figure 6.9 (a) shows the resulting progression of crystal fraction with anneal time for each sample. Figure 6.9 (b) shows Avrami, log-scale plots of each crystallization curve, similar to those utilized in Figure 4.6, demonstrating the time dependence of each samples grain growth.

It is clear from the results of figure 6.9 (a) that films containing seed crystals grown at 150 W and 160 W exhibit faster rates of crystallization relative to 140 W samples. It is interesting that crystallization curves overlap strongly for 150 W and 160 W samples despite the greater presence of relatively larger seed crystals evident in the 160 W sample. This suggests particle shape to have a more significant effect on increasing crystallization kinetics then size. The increased microstructure evident in figure 6.7, along with TEM observations suggest this enhancement of crystallization rate to be a due to an increased presence of void-induced-crystallization in both 150 W and 160 W samples.

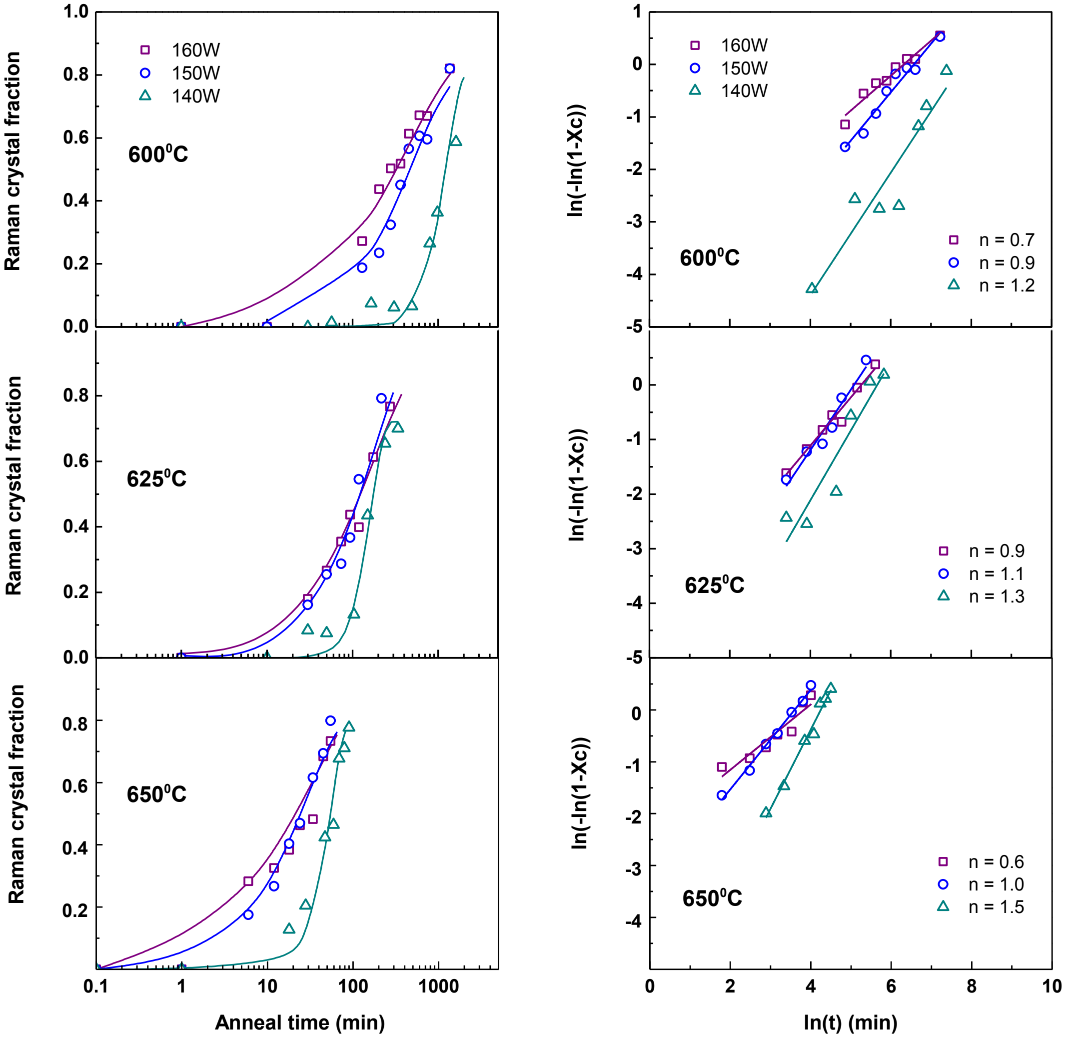

(a)

(b)

Figure 6.9: (a) Raman crystal fraction with anneal time for 100 nm films containing a monolayer of seed crystals deposited at seed densities of $\sim 3/\mu m^2$. Seed crystals were synthesized at powers of 140 W, 150 W, and 160 W, resulting in cubic and cuboctahedral shapes, respectively. (b) Avrami plots of the crystal fraction curves from (a). The resulting slope "n" indicates the time dependence of the crystallization behavior, after equation 4.2.

It is also interesting to note the monotonic decrease in Avrami slope “n”, with increasing power, shown in figure 6.9 (b). Values for “n” range between 1.2 to 1.5 for 140 *W* samples, decreasing to 0.9 to 1.1 for 150 *W* samples and 0.6 to 0.9 for 160 *W* samples. Since “n” has been suggested to be linked to the dimensionality of grain growth [107, 108, 140], this trend suggests a different, more constrained, growth geometry to be present for higher-faceted crystals, relative to cubic seed crystals. For instance, in-situ TEM studies of VIC observe void motion to cease once a competing void-wake or crystalline region is encountered. Due to the relatively rapid rate of void propagation, it is also conceivable that grain growth dominated by VIC involves a greater degree of interaction between adjacent grains at earlier annealing stages. The subsequent restrictions associated with void interactions could potentially translate into a perceived reduction in time dependence. It should also be noted that the reduction in “n” for 140 *W* samples relative to the values observed in Chapter 4 is likely due to a reduction in film thickness from 200 *nm* to 100 *nm*, as grain growth is expected to be interrupted by the film surface and substrate interfaces at much earlier annealing stages.

6.4 Conclusions

A modification of seed crystal shape from a cubic to a higher-faceted cuboctahedron geometry was demonstrated to occur with increasing RF synthesis power. The precise mechanism behind the observed shape transformation is unknown, however hydrogen is believed to play a central role through etching and/or particle heating. It is clear from the above observations that seeding films with cuboctahedral crystals leads to an enhanced crystallization rate and reduced Avrami slope relative to seeding with cubic crystals. This increase crystallization rate is likely due to the presence of a unique crystallization mechanism, involving the propagation of nano-scale cavity regions or “voids” within the film. It is believed that these voids result from the coalescence of cavities formed during the top-layer of a-Si:H film deposition, due to an enhanced shadowing from the higher-faceted seed crystal shapes. At the time of this study, it is unclear whether the grain structures formed from void-induced crystallization have properties more suitable for device structures. Additional studies are required to understand and exploit the potentially novel grain structures available through this mechanism.

Chapter 7

The Effect of Varying Film Properties on Crystallization Kinetics

7.1 Introduction: The Motivation for Varying Film Properties

The absorber layer of a competitive poly-Si solar cell consists of grains extending through the device thickness, with viable device thicknesses considered to be 1 μm or more. Producing devices in this thickness range requires significantly increased deposition rates relative to those used in the experiments discussed in previous chapters. In the studies outlined in this chapter, film deposition conditions were varied relative to those used previously, to study the crystallization times of seeded films, and incubation times of similar, unseeded films, grown at relatively higher deposition rates.

7.1.1 The Relevance of Increasing Film Deposition Rate

Deposition rates of seeded films studied thus far have been near 2 nm/min using the procedure and parameters outlined in section 3.1.2. At this deposition rate, synthesizing a μm thick film would require a 9 hour deposition. Current industry efforts aim to achieve deposition rates near 100 nm/min or more, however this typically involves RF frequencies greater than 100 MHz, which typically leads to difficulty in film quality, uniformity, and process scaling [25]. For the studies outlined in this chapter, it was desired to achieve deposition rates that would allow for growth of a μm thick film within a two hour deposition window, using an RF frequency of 13.56 MHz. This required achieving deposition rates of 10 nm/min or more.

7.1.2 The Relevance of Through-thickness Grain Penetration

As discussed in section 2.5.3, the solar cell device measurement most commonly associated with grain structure quality in poly-crystalline devices is open circuit voltage (V_{oc}). V_{oc} is defined as the maximum potential voltage that can be accumulated across the thickness of a photo-voltaic device, operating under standard AM 1.5 illumination. It is in the film thickness dimension that photo-excited carriers must be able to easily travel in order to generate a voltage difference between the top and bottom contacts connecting the device to an external circuit. For this reason, V_{oc} is heavily dependent on the electronic transport quality in the film-thickness dimension, decreasing with inter-grain defects such as grain boundaries, and intra-grain defects such as dislocations [56,73,141]. Specifically, studies such as those shown in figure 2.4 have demonstrated device performance to be more heavily dependent on grain structure in the thickness dimension, rather than in the plane of the film.

Conversely, the maximum current achievable by a particular photo-voltaic device is more heavily dependent on the optical absorption properties of the device. Due to the indirect band-gap of crystalline silicon, poly-Si absorber layers typically require thicknesses greater than a micron in order to generate sufficient current [26,40]. Subsequently, a competitive, device-grade poly-Si film would have a thickness in the micron range, and consist of single grains extending from substrate to film surface, or"through-thickness".

The layer-by-layer structure of seeded film deposition, by the dual-plasma system, is amenable to creating grain structures of this nature. However, this requires film conditions in which seeded grains grow to the extent of the film thickness, before the emergence of natively nucleated grain clusters at the conclusion of the host film incubation period. Due to the relatively random, high density growth of native clusters, the presence of native grains is undesirable in this context. Subsequently, the following studies of deposition rate include investigations of the corresponding effects of relatively higher deposition rate films on grain growth rate of seeded films and the incubation time of unseeded films.

7.2 The Effect of Varying Pressure and Power

7.2.1 Deposition Rate

Two plasma parameters commonly linked to deposition rate are deposition pressure [142, 143] and RF power [7, 25]. Higher pressures lead to increased radical fluxes to the substrate surface, while higher RF powers result in increased plasma density [83]. The studies conducted in previous chapters involved depositions carried out at a pressure of 100 $mTorr$ and a nominal RF power of 5 W. Figure 7.1 (a) below shows deposition rates measured for nominal powers ranging from 5 W to 15 W, at deposition pressures of 100, 200, and 400 $mTorr$. Films were deposited on silicon wafer substrates and thicknesses were measured using scanning electron microscopy (SEM).

For 100 and 200 $mTorr$ parameter spaces, deposition rates showed negligible difference, with very mild increases across the range of powers studied. At 400 $mTorr$, however, deposition rate increases significantly with power, approaching 8 nm/min at 15 W.

This trend is consistent with literature observations on similar systems, where deposition rate has been shown to increase sharply at specific pressures, due to a transition between α and γ discharge modes. The low pressure α regime is characterized by lower deposition rates due to a lower frequency of electron-neutral collisions primarily occurring far from the electrodes, and film densification from relatively large ion-bombardment energies. Conversely, the higher pressure γ regime is characterized by much larger deposition rates due to a greater frequency of collisions concentrated in the sheath regions, closer to the substrate [83, 143–146].

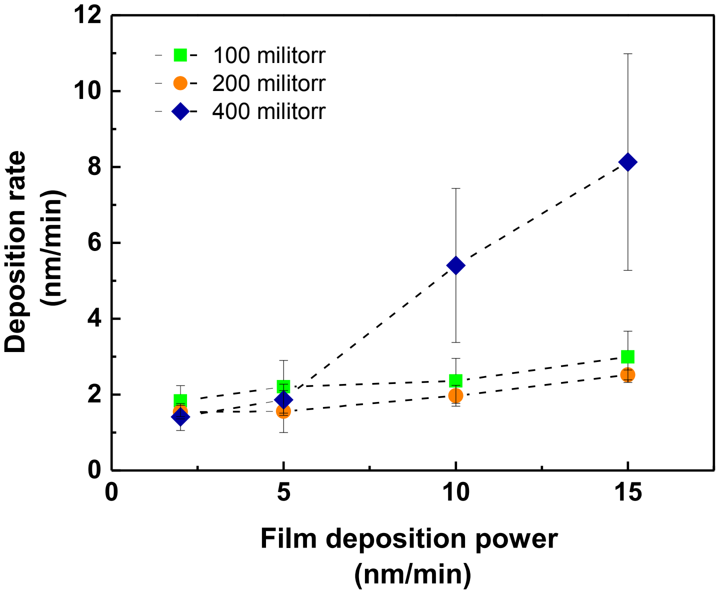

Figure 7.1: a-Si:H film deposition rate vs. pressure and nominal RF power. Measurements were taken over two sets of samples. Each sample set was deposited at separate deposition times with thicknesses measured by SEM and scanning ellipsometry.

Film deposition pressures could not be increased beyond 400 $mTorr$ due to limitations on the capacity of the turbo-molecular pump used in the current chamber configuration. Subsequently, in order to achieve further increases in deposition rate, the 400 $mTorr$ parameter space was expanded to include deposition powers of 20 W and 25 W. Powers much higher than 25 W risk approaching growth regimes favorable for particle formation within the plasma, and result in extremely low quality film and even unintended crystallite formation. Subsequently, the resulting parameter space of interest for the deposition rate studies in this chapter consisted of a pressure of 400 $mTorr$, with nominal RF powers ranging between 2 W to 25 W. Figure 7.2 shows the resulting average deposition rates for each film condition. For RF powers above 5 W, deposition rate increases significantly, approaching 13 nm/min at 25 W. This parameter space was reproduced over three sample sets, with deposition rates measured by both SEM and spectroscopic ellipsometry.

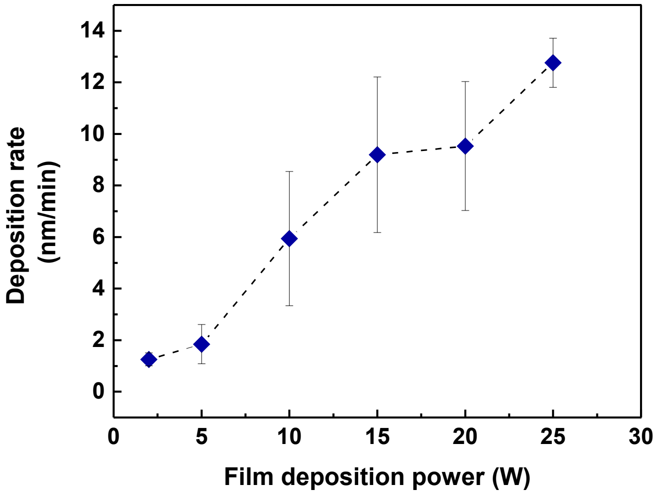

Figure 7.2: a-Si:H film deposition rate vs. nominal RF power for films grown at 400 $mTorr$. Film thickness measurements were taken by SEM and spectroscopic ellipsometry. The resulting error bars represent the standard deviation of thickness measurements taken over three sample sets.

7.2.2 Film Properties

Several film properties of interest are expected to change concurrently with deposition rate. Specifically, the variation of film microstructure (R*) and hydrogen content (H%) with film deposition power are shown in figure 7.3, for the 400 $mTorr$ parameter space of interest. Both properties show similar increases, a majority of which occurs between powers of 5 W to 15 W. These observations show a relatively abrupt transition between film conditions to accompany the transition between low and high deposition rate regimes. Both microstructure and hydrogen content increase significantly between these regimes, but plateau at relatively higher powers.

This observed trend can be more specifically linked to an increase ion density and ion bombardment energy with increasing RF power. In the context of a-Si:H film deposition, increasing RF power can result in two primary influences on the depositing film, depending on deposition pressure. At low pressures, ion bombardment energies are relatively high due to a lower frequency of collisions within the plasma bulk. This can result in defect generation with the growing film surface, and subsequent increases in microstructure and hydrogen content.

At relatively high pressures such as the 400 $mTorr$ parameter space of study here increased collisions within the plasma lead to a reduction in ion bombardment energy, however similar disordering effects can occur due to silane polymerization, and the incorporation of higher order silicon-hydride radicals in the depositing film [146, 147]. Increasing power at elevated pressures enhances this effect, but in a limited capacity. Above a certain threshold power, the effects of plasma polymerization and ion bombardment become counteracting. Specifically, the porous regions formed from plasma polymerization are collapsed by ion bombardment, and surface roughness can be diminished by momentum transfer to the film growth surface by ion surface collisions, causing the plateau observed in the trends of Figure 7.3 [146,148,149].

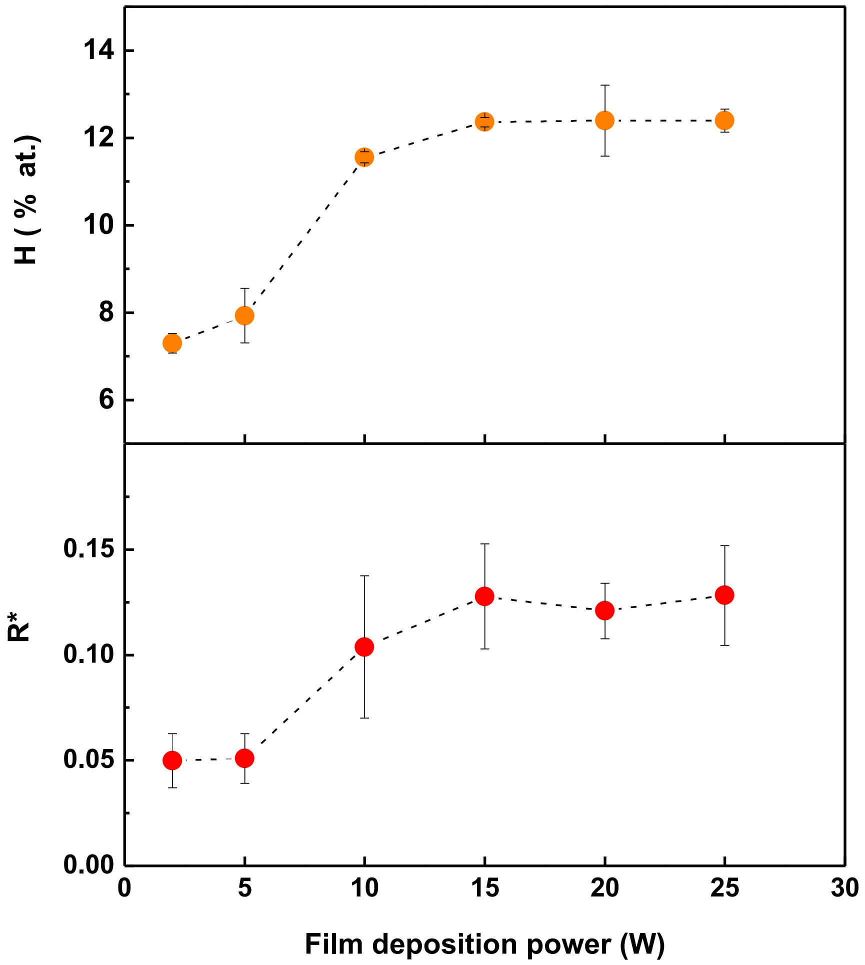

Figure 7.3: Microstructure parameter (R*) and Hydrogen content of unseeded a-Si:H films deposited at 400 $mTorr$, for various RF powers. Microstructure measurements were taken using the methods outlined in section 3.1.2.

7.2.3 Seeded Crystallization Kinetics

Due to the diverse range of film conditions observed in figures 7.2 and 7.3, the deposition parameter space of 400 $mTorr$, with RF powers ranging from 2 W to 25 W was the focus of study for the effect of film properties on crystallization kinetics. Subsequently, seeded and unseeded films were deposited at 400 $mTorr$, at RF powers varying between 2 W to 25 W. Films were grown at equal thicknesses of 100 nm, with seeded films consisting of a single seed layer 50 nm below the film surface, deposited at an aerial density of approximately $6/\mu m^2$. Seed crystals were cubic in shape, and grown using the procedure outlined in chapter 3. Annealing studies were carried out for several temperatures in a quartz furnace under nitrogen ambient. Crystal fractions were measured at regular time intervals with Raman spectroscopy, using the techniques outlined in section 4.2. Due to the relatively high microsturucture and hydrogen fraction values measured, films were "pre-annealed" at 500 °C for 30 min to prevent peeling from rapid formation of molecular hydrogen bubbles.

Figure 7.4 shows the crystallization times for seeded films annealed at 600 °C, 625 °C, and 650 °C. Crystallization time decreases with film deposition power over this parameter space, with the most significant decreases occurring in the same power regime that film microstructure and hydrogen content were observed to increase in Figure 7.3. Figure 7.5 shows corresponding grain growth rates for each film displayed in a similar fashion, above microstructure and hydrogen content trends. Grain growth rates were found by fitting the crystallization curves with equation 4.2.

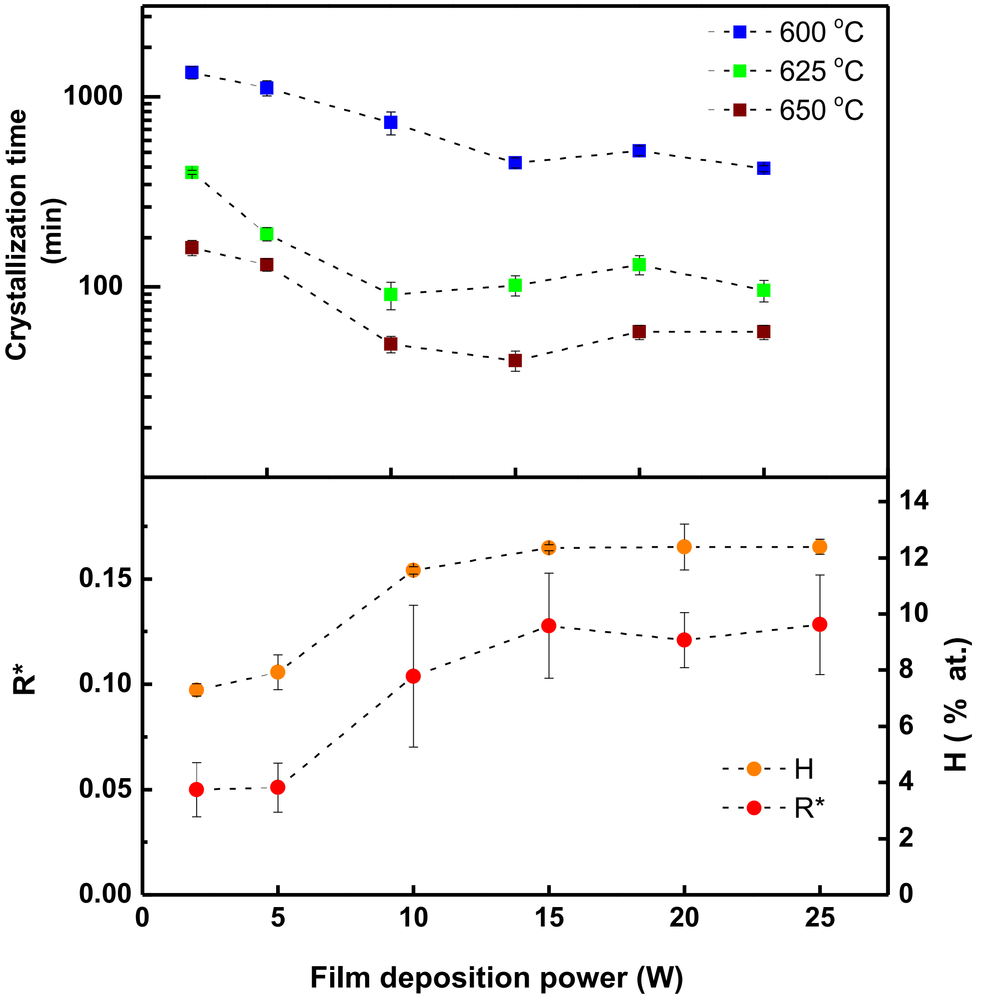

Figure 7.4: Crystallization times (top) for 100 nm seeded films, deposited under various a-Si:H film deposition powers and annealed at 600 °C, 625 °C, and 650 °C. The observed decrease in crystallization time with power coincides closely with measured changes in film properties such as microstructure and hydrogen content (bottom).

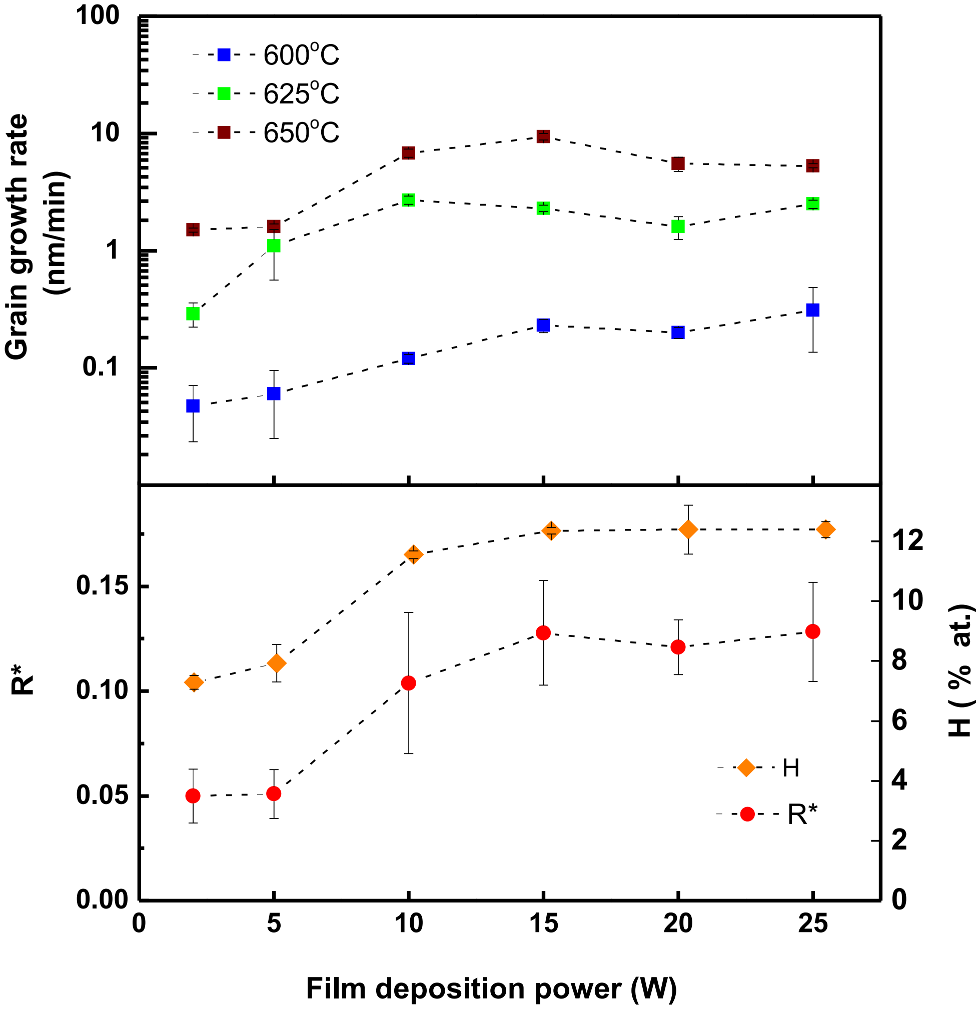

Figure 7.5: Seeded grain-growth rates (top) for 100 *nm* seeded films, deposited under various a-Si:H film deposition powers and annealed at 600 °C, 625 °C, and 650 °C. The observed decrease in crystallization time with power coincides closely with measured changes in film properties such as microstructure and hydrogen content (bottom).

The Role of Microstructure

It is interesting that the observed increases in seeded crystallization rate correlate strongly with both microstructure and hydrogen content trends. It is reasonable to suggest that this behavior may be due to an increased presence of the void crystallization mechanism discussed in chapter 6, due to the observed increase in microstructure with deposition rate. Furthermore, it is anticipated that films grown at higher deposition rates should experience a greater degree of shadowing at the seed plane. It is well documented in thin film deposition literature that conformal coating over step-like features is more difficult to achieve at elevated deposition rates [82].

To investigate this hypothesis further, numerous seeded films deposited at 5 W and 25 W were compared via heated-stage TEM to determine the relative contribution of void-induced-crystallization, if any, to the observed crystallization. Figure 7.6 compares TEM images taken *in-situ*, during annealing of 100 nm, seeded films grown at 5 W and 25 W. The images shown were taken during annealing at 610 °C, and 625 °C for 5 W and 25 W films respectively. Each film contained roughly equivalent seed mono-layers, having aerial densities of approximately $6/\mu m^2$.

After 10 min at 625 °C, numerous voids are seen to form in the 25 W films (marked by red arrows) near the perimeters of seed crystals. However, of the voids observed formed, only a small number (bottom left) proceed to propagate through the film. By 60 min, most of the observable film crystallization was governed by grain growth from the seed crystals themselves, with a majority of the void population becoming engulfed by the surrounding grain growth. Red arrows track the diminishing population of propagating voids with anneal time, decreasing from $\sim$15 to $\sim$5 from 10 min to 60 min for the 25 W film. No void formation was observed for the 5 W film, likely due to the lower deposition rate, and subsequently lower degree of shadowing. Similar results were reproduced across several samples deposited at 5 W and 25 W.

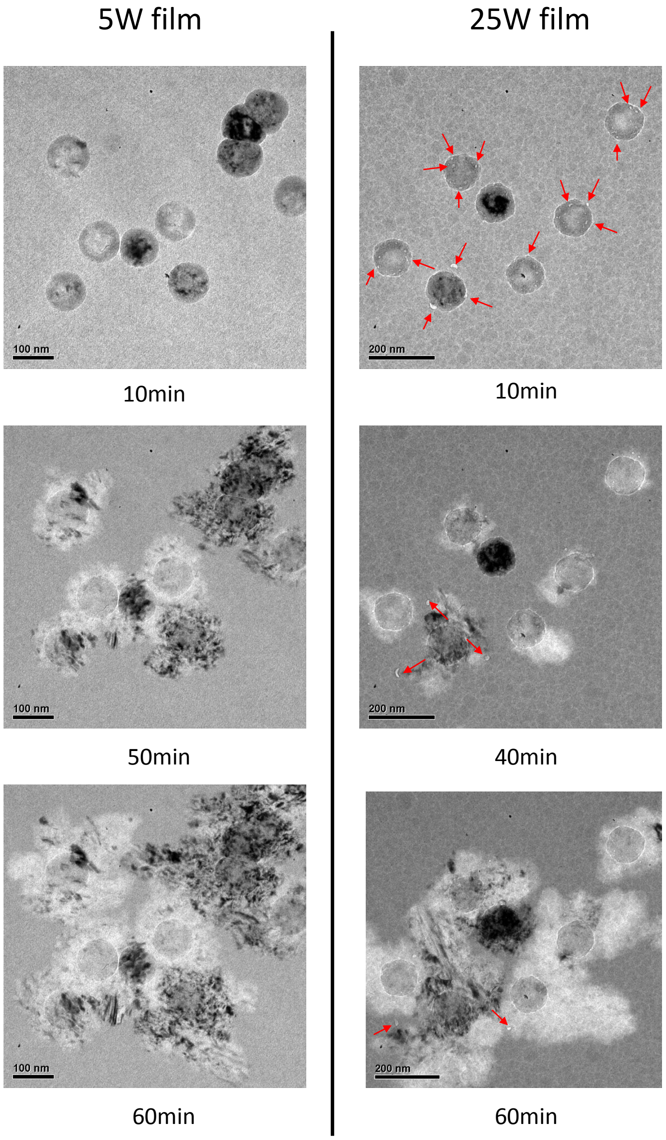
5W film
25W film

10min
10min
50min
40min
60min
60min

Figure 7.6: TEM images taken *in-situ*, during annealing of 100 nm seeded films, with a-Si:H film deposited at 400 $mTorr$ and powers of 5 W (left) and 25 W (right), and annealed at 625 °C and 610 °C, respectively. Red arrows track the population of propagating voids in the 25 W film, indicating the diminishing role of void-induced crystallization with time, due to entrapment by rapid seed growth fronts. No voids were seen to form in the 5 W film.

Measuring Microstructure at the Seed Plane

In order to draw conclusions about film porosity in seeded films, specifically in the region of the seed plane, FTIR was performed on several samples of varying a-Si:H top layer film thickness. This effectively results in a virtual depth profiling of film microstructure, as films with larger top layers "dilute" the contribution of the seed plane to the overall FTIR signal. For films deposited at 2 W and 25 W, four seeded samples were deposited with 50nm base layer, a seed layer of approximately $6/\mu m^2$, and one of four top layer thicknesses varying between 50 nm to 200 nm. FTIR spectra were taken for each sample and used to calculate microstructure (R*), using the techniques outlined in [90, 91].

Figure 7.7 shows the resulting microstructure values for each film, with respect to overall film thickness. For seeded films, smaller film thicknesses correspond to samples with a greater signal contribution from the seed plane, which is reflected in the relatively larger microstructure values. It is clear that both 2 W and 25 W films exhibit measurably higher microstructure near the seed plane. Films deposited at 25 W appear to exhibit slightly higher microstructure values over the range of thicknesses measured, however, this increase is relatively small with respect to the increases measured in chapter 6, in which films with a consistent void presence were measured to have roughly twice the microstructure of similar films with little or no void presence.

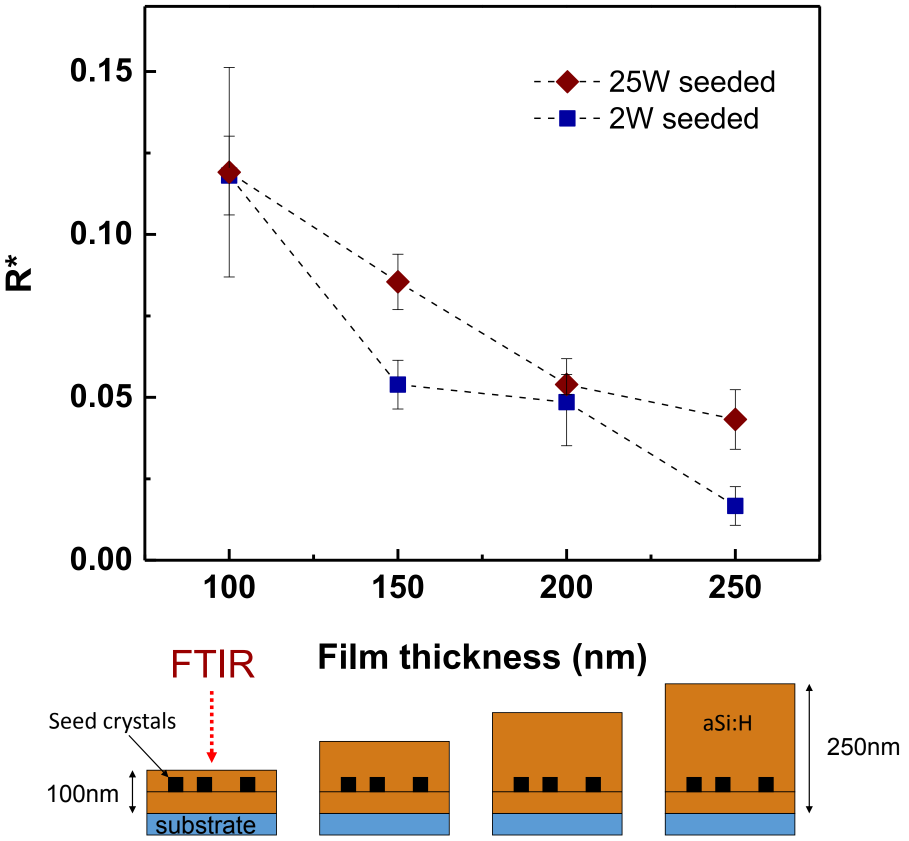

Figure 7.7: Microstructure vs. film thickness for seeded and films grown at 400 $mTorr$ and RF power of 2 W and 25 W. Seeded films were deposited with a 50 nm base layer and seed layer density of approximately 6 $/\mu m^2$. Top layer thicknesses of seeded films were varied to provide an indication of the effect of the seed plane on microstructure for each deposition power. Unseeded films grown at 2 W are overlaid as a baseline for comparison.

The Role of Hydrogen

The appearance of voids without void propagation in films grown at higher powers, can possibly be explained by an enhanced gettering of smaller porous regions in the presence of increased hydrogen content. For instance, the cavity coalescence discussed in chapter 6, has been shown to be more significant in the presence of hydrogen [134,135,150]. This is argued to be due to the ability of hydrogen atoms to mobilize within the amorphous bond matrix at temperatures as low as 400 °C, and diffuse through interstitial locations at Si-Si weak bonds. This motion is inhibited when a hydrogen atom diffuses to a mono-vacancy in which one or more stable Si-H bonds are present. The mobile hydrogen atom becomes trapped, and the once temporary interstitial position becomes an additional, stabilized dangling bond, following the reaction outlined in equation 7.1 below [135]. This proceeds with the trapping of additional, mobile hydrogen to eventually form larger nano- and micro-scale cavities.

$$SiHSi + SiH \longrightarrow Si^{o} + SiH + SiH \tag{7.1}$$

Subsequently, although films grown at 2 W and 25 W may show similar degrees porosity at the seed plane, the porous regions in the 25 W films may coalesce more effectively into larger, more visible sizes due to a larger presence of hydrogen. However, these voids fail to propagate due to their encapsulation by the rapid motion of the seeded grain-growth front.

Preliminary Conclusions on Enhanced Seeded Crystallization

This suggests that the measured increase in crystallization rate for 25 W seeded films originates primarily from an increase in the radial grain growth or solid-phase epitaxial growth (SPEG) of the seed crystals themselves. At the time of this report, it is not certain what the mechanism behind the observed enhancement of SPEG in films deposited at higher powers films is. However, it is likely due to the effect of both additional hydrogen as well as increased microstructure. In addition to coalescing vacancies, mobile hydrogen has been demonstrated to restructure strained or weak bonds during the effusion process in the early stages of annealing [151]. Subsequently, hydrogen effusion has been shown to serve as a catalyst for crystallization at amorphous/crystalline interfaces [65, 135, 151].

In the context of microstructure, it is possible that the additional defects associated with the more disordered network result in a relatively metastable interface between grains and amorphous tissue. Interfaces of this nature have been observed to demonstrate enhanced crystallization rates. For instance, work by Wagner *et al.* has shown that the interfacial energy between crystallite nuclei and the surrounding amorphous film is reduced when the interface is rendered less “coherent” by dangling bonds [152].

7.2.4 Unseeded Incubation Times

The exact mechanism for the enhanced grain growth rate seeded at relatively higher powers is unknown at this time. However, the positive correlation between deposition rate and crystallization rate in seeded films shown in Figure 7.5 is advantageous to the ultimate processing objective of achieving thick-grain devices. As discussed in section 7.1.2, the primary limitation to the size of grains originating from a seed crystal is the incubation time of the surrounding film. The radial growth front from each seed crystal must expand to the extent of the film thickness before the onset of native nucleation in the surrounding film. Therefore, the incubation time of the unseeded film is an approximation of the growth window available to each seed crystal.

Figure 7.8 shows a comparison of unseeded incubation times for films deposited in the same pressure and power regimes discussed in the previous section. Specifically, 100 nm films deposited at a pressure of 400 $mTorr$, at nominal RF powers ranging from 2 W to 25 W. Incubation times were defined as the approximate time of crystallization onset, taken as the anneal time at which the first measurable crystal fraction below 0.10 was observed by Raman spectroscopy. This is comparable with X-ray diffraction characterization techniques used in literature, where incubation times are taken to be the time at which 10% of the saturated crystal fraction occurs [136, 153]. Seeded crystallization times (from figure 7.4) are overlaid for comparison. Films in which unseeded incubation times exceed crystallization times in corresponding seeded films, exhibit the potential for larger grain sizes.

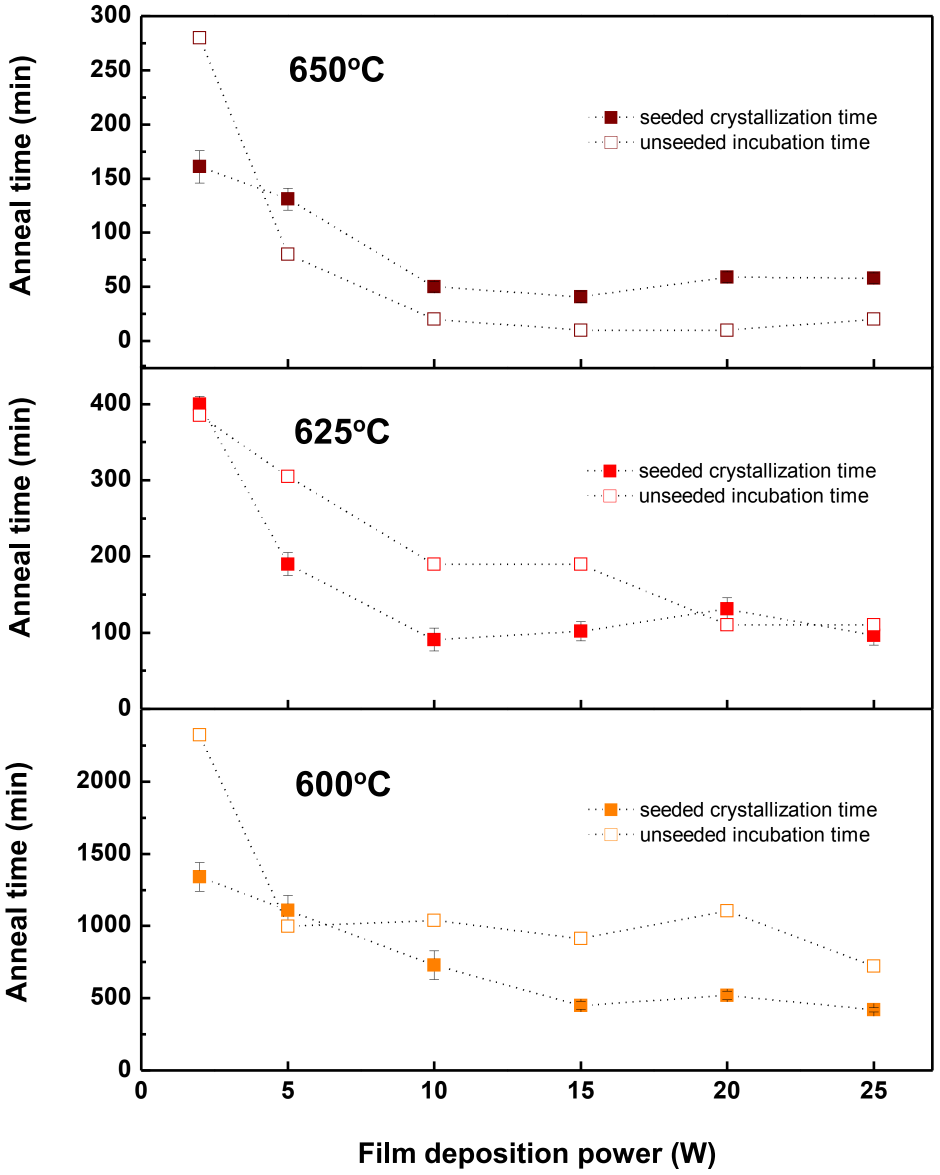

Figure 7.8: Incubation times of unseeded films (open symbols) compared to crystallization times of commensurate seeded films (closed symbols) grown at 400 $mTorr$ and a nominal RF power of 2 W to 25 W. Samples with larger positive time differences between unseeded incubation times and seeded crystallization times exhibit potential for the largest grain sizes.

It is interesting that incubation times of unseeded films decrease with deposition power in the same manner as seeded crystallization times. For the outlined objective of achieving large grain sizes from seeded films, ideally, incubation times would increase with deposition rate, thus allowing a larger window of growth for seeded crystallization. It is possible this trend is a result of the same mechanisms likely responsible for enhanced seeded grain growth, mainly, hydrogen restructuring during early annealing stages. However, consensus still remains to be achieved, in literature reports, regarding the precise individual roles of hydrogen content and microstructure in controlling incubation times. This is mainly due to the fact that microstructure and hydrogen content are strongly coupled parameters; with increases hydrogen content tending to accompany any increases in microstructure.

The few studies that have been able to decouple these properties suggest that microstructure tends to increase incubation time only if there is a lack of available hydrogen (typically below 8-10%) to restructure the disordered bond matrix [61,65]. Conversely, if sufficient hydrogen is available the hydrogen effusion process in early anneal stages acts to restructure defected regions, leaving denser, more ordered regions behind [65,136]. It is argued that these resulting restructured regions are capable of forming stable nuclei in less time than un-restructured material.

Work by Sharma *et al.* specifically showed incubation times to increase with increasing microstructure for films with hydrogen concentrations below 8%. In the same study, a similar set of films was shown to have increasing incubation times with increasing microstructure, and hydrogen contents above 8% [136]. It is believed that this is the mechanism behind the trend of decreasing incubation times with deposition power observed here. Specifically, higher deposition rate films experience lower incubation times due to a combination of meta-stable microstructured film, and a sufficient enough hydrogen content to catalyze its rapid restructuring into denser, native-nucleation conducive material. It is interesting to note in figure 7.8 that incubation times decrease significantly for powers above 10 W, which is also the power at which hydrogen content increases from below 8% to above 11%.

7.2.5 Argon dilution

In isolating the effect of hydrogen content on incubation time, it was desired to study a similar parameter space of films exhibiting increasing deposition rate and microstructure, but without varying hydrogen content. This was accomplished by depositing films grown with the silane precursor diluted 50% in argon. Films were grown at 100 $mTorr$ and 250 °C using 40 *sccm* of argon with 40 *sccm* of 5% SiH_4 diluted in helium. For powers ranging from 2 W to 15 W, deposition rate increased by a factor of 3, microstructure increased by a factor of 2, and as-deposited hydrogen content remained near 10%, which is above the cited threshold concentration for enhanced reconstruction [65, 136].

Figure 7.9 shows the incubation times and film properties of 100 nm unseeded films grown in argon dilution and annealed at 600 °C. Incubation time decreases significantly with increasing power from 2 W to 5 W, despite the invariance of hydrogen content. It is interesting that this trend correlates with the observed increase in microstructure. This is consistent with the findings of Budini *et al.* [65] and Sharma *et al.* [61], and the hypothesis that microstructure is capable of generating dense, ordered regions in the presence of sufficient hydrogen concentrations.

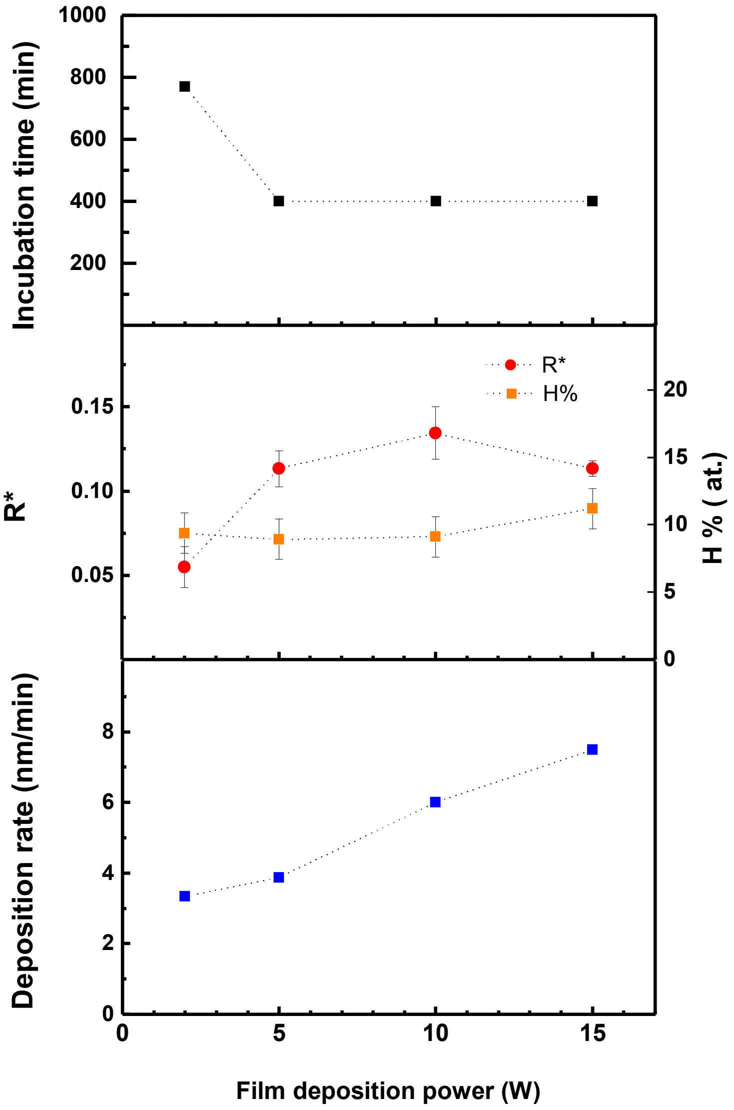

Figure 7.9: Top: Incubation times of 100 nm unseeded films grown in argon dilution and annealed at 600 °C. Films were grown at 100 $mTorr$ and 250 °C using 40 $sccm$ of argon with 40 $sccm$ of 5% SiH4 diluted in helium. Deposition power was varied to produce a parameter space of increasing microstructure without varying hydrogen content. Middle: corresponding microstructure and hydrogen content. Bottom: corresponding deposition rates.

7.2.6 Theoretical Grain Size of High Deposition Rate Seeded Films

Despite an incomplete understanding of the mechanisms behind the increased seeded crystallization rate and decreased incubation observed at elevated deposition rates, an optimal process window for achieving micron-scale grains at relatively higher deposition rates can still be identified using the information gathered from Figures 7.5 and 7.8. Using incubation times from Figure 7.8 and growth rates from figure 7.5, a theoretical seeded grain diameter d_g can be approximated for the relatively higher deposition rate, 400 $mTorr$ parameter space studied in this chapter. Grain size was estimated for each of the deposition power, using equation 7.2

$$d_g = 2 * v_g * \tau_o \tag{7.2}$$

where v_g is the radial, seeded grain growth rate (from figure 7.5) and τ_o is the incubation time of the surrounding film. Note should be made that unseeded incubation times were assumed to be equivalent to the incubation times of the amorphous component of seeded films. This is likely a conservative assumption, as the short range film disorder imposed by seed inclusions may lead to longer incubation times, as demonstrated in Chapter 5. It follows that the grain size estimates shown in figure 7.2 are likely conservative estimates.

Figure 7.10 shows the resulting estimated grain sizes for films grown at 400 $mTorr$ at the deposition powers and annealing temperatures studied. Deposition rates (from Figure 7.2) are included as well to provide an overall comparison of process. Based on these results, the most optimal processing conditions for achieving large-grained devices appears to be for films grown at deposition powers between 10 W to 15 W, and annealed at temperatures near 625 °C. This parameter space predicts grain sizes approaching 1 μm, with film deposition rates of approximately 6 nm/min to 9 nm/min.

It is not surprising that an intermediate temperature of 625 °C appears to facilitate the largest relative grain sizes for films grown under these conditions. This reflects the trade-off between relatively higher seed growth rates observed at higher temperatures and longer incubation times observed at lower temperatures. It is likely that a more optimal anneal temperature exists at intermediate values. Further investigation is required over intermediate temperatures to determine if such an optimum exists.

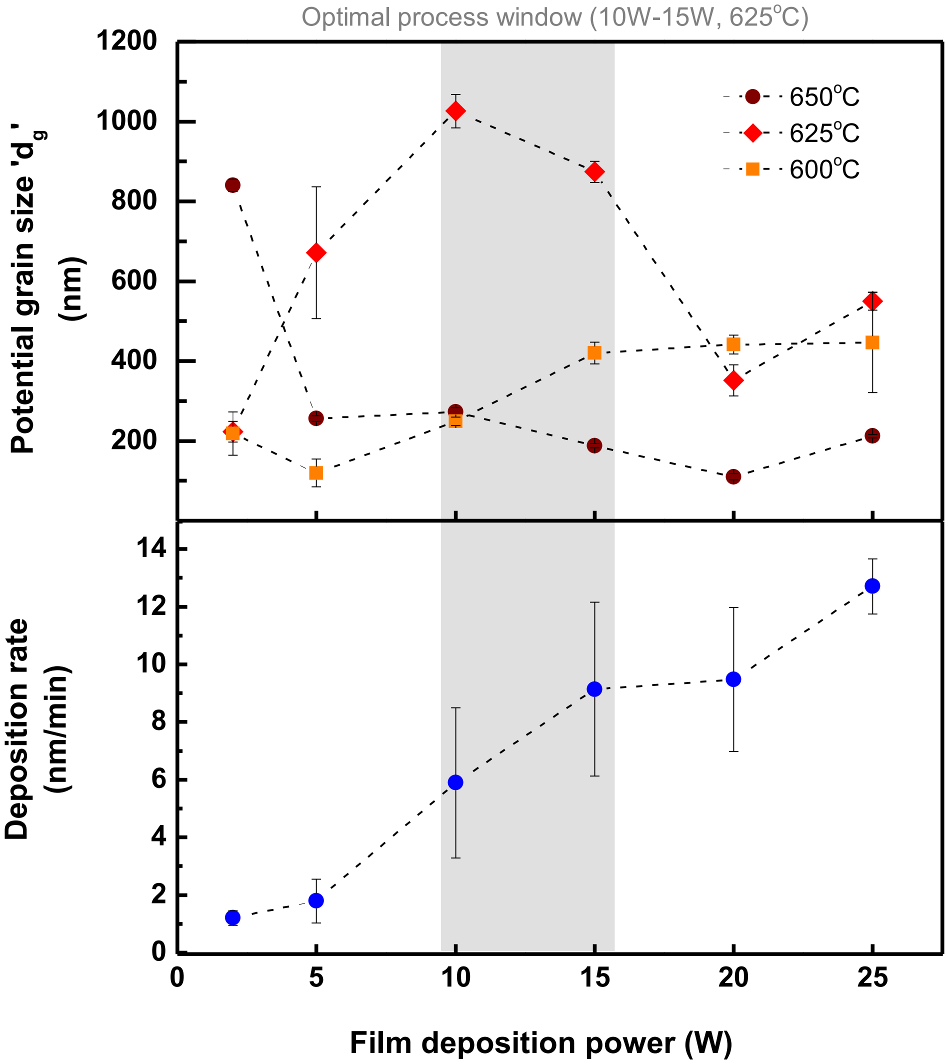

Figure 7.10: Top: Potential grain sizes achievable by seeding films grown at 400 $mTorr$, for several RF deposition powers, and annealing temperatures. Bottom: Corresponding deposition rates for each deposition power. Results indicate an optimal process for large grain films to exist for films deposited between RF powers of 10 W to 15 W, and annealed near 625 °C.

7.3 Conclusions and Recommendations

The effect of varying film properties on seeded crystallization kinetics and unseeded incubation time has been demonstrated. Specifically, a parameter space consisting of films grown at 400 $mtorr$ with RF powers varying from 2 W to 25 W was studied, in which deposition rates increased toward more industrially viable levels, relative to film deposition processes utilized in previous chapters. Corresponding increases in basic film properties such as microstructure and hydrogen content were also measured in this parameter space, and their effects on seeded crystallization were observed. Most notably, an increase in seeded crystallization rate was observed to occur with increasing deposition rate.

Although an increase in void appearance also occurred in these higher deposition rate films, void-induced crystallization was observed to play a minimal role in the crystallization rate enhancement. This enhancement is believed to be due primarily to an increase in the radial, epitaxial grain growth rate from each seed crystal, and is possibly a result of a meta-stable, defect-rich film matrix catalyzed to restructure more rapidly by hydrogen. A similar enhancement in native nucleation was observed for unseeded films, believed to be due to similar restructuring effects.

Seeded grain growth rates were combined with observed incubation times of unseeded films to estimate potential grain sizes achievable by seeding films grown in a relatively higher deposition-rate parameter space. Viable deposition and annealing conditions have been identified with the potential of resulting in through-thickness grains, of micron-scale, grown at relatively higher deposition rates, at an RF frequency of 13.56 MHz. For the outlined objective, of through-thickness grain growth, a more ideal parameter space would exhibit increasing incubation times with deposition rate, thus allowing for a larger window of time for seeded grain growth. However, a precise understanding of the effects of plasma deposition conditions on incubation time is still lacking. Based on preliminary observations of incubation behavior in this chapter, it is believed that a more ideal parameter space would involve films with relatively large microstructure (≥ 0.15), having relatively low hydrogen concentration ($< \%7$). This may potentially be achieved by re-producing the above parameter spaces at higher deposition temperatures.

Chapter 8

Conclusions

8.1 Summary of Processing Advantages

This thesis has demonstrated the potential advantages of a novel process for synthesizing poly-crystalline silicon thin films. The processing advantages of annealing films containing an embedded population of grain growth sites has been demonstrated through several *ex-situ* studies of crystallization kinetics. Measurable reductions in crystallization time were observed for films containing seed crystals, relative to traditional, unseeded films.

Thermal Budget Reduction

The reduction in thermal budget provided by this technique can be quantified relative to other techniques using a metric referred to in literature as an "annealing factor". The annealing factor is calculated as the product of annealing temperature (in celcius) and annealing time to complete crystallization (in minutes), normalized to film thickness (in nm). When plotted against deposition temperature, a complete picture of the thermal budget associated with the overall film deposition and annealing process can be quantified. Figure 8.1 shows annealing factor plotted with respect to deposition temperature for several films reported in literature pertaining to the most successfully performing solar cell absorber layers.

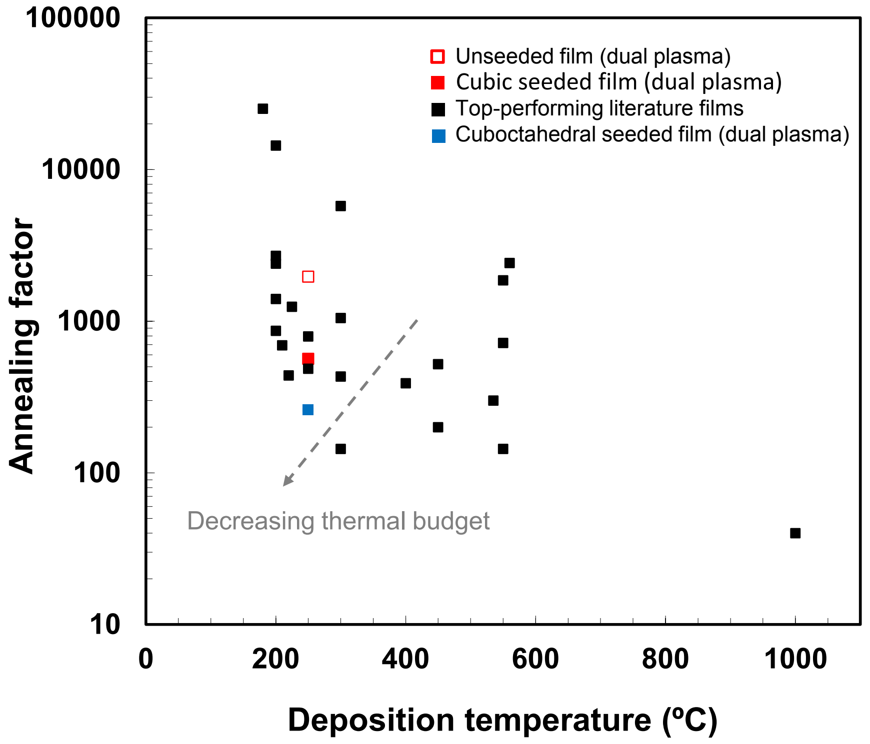

Figure 8.1: Comparison of the overall thermal budgets associated with several different film synthesis and annealing processes. Annealing factor is defined as the product of annealing temperature and annealing time, normalized to film thickness. Black symbols represent several selected processes from literature; including the top-ten highest performing poly-Si solar cell absorber layers as of 2010 [22, 23, 49, 53, 58, 60, 62, 63, 68, 71, 79, 80, 92, 136, 154, 154–159]. Red symbols represent 200 nm films grown from the dual-plasma reactor. The blue symbol represents a 100 nm film seeded with cuboctahedral seed crystals deposited at 150 W.

The annealing factors corresponding to films deposited in the dual plasma reactor are shown in red. The closed red symbol pertains to a 200 nm film containing a monolayer of seed crystals, $\sim 6/\mu m^2$, annealed at 650 °C. The open red symbol represents a commensurate 200 nm unseeded film. The overall trend depicts the ostensibly inherent process trade-off, in which a reduction in thermal budget during deposition (by decreasing deposition temperature) results in an increase in thermal budget during post-deposition annealing, as reflected in by an increase in anneal factor. Subsequently, the lower left corner of Figure 8.1 represents a region of relatively lower thermal budget. It is clear from this figure that seeded films grown from the dual plasma technique exhibit relatively low thermal processing budgets, with a significant reduction relative to the commensurate unseeded film shown.

Final Film Performance

Studies on the effects of a varying initial seed crystal population have demonstrated the ability of the resulting poly-Si film structure to be controlled. Specifically, the initial seed crystal population has been demonstrated to dictate the final grain structure in a way that translates into measurable modifications of grain size, and electronic transport properties.

New Insights on Crystallization Kinetics

As was outlined in chapter 2, several similar, mixed-phase material systems have been studied for their unique properties in the as-grown state. However, at the time of this report, little has been to characterize the basic parameter spaces associated with annealing films containing an initial population of seed material. This is mainly due to a lack of reproducible control over the basic properties of the seed material. The independent processing of seed and film components, provided by the dual-plasma approach, has facilitated studies of interesting new phase transformation behavior. Successful modification of seed crystal shape was demonstrated in chapter 6, with relatively high yield and narrow size distribution. Such controllable modifications are rare for gas-phase processing in group IV materials; and are typically exhibited in colloidal, liquid-phase processing. It was demonstrated that modification of seed crystal shape leads to further enhancements in seeded crystallization kinetics, due to the presence of an interesting “void-induced crystallization” mechanism. Further studies are required to determine the potential benefits of the grain structures possible with this mechanism, as well as processing conditions that could potentially enhance crystallization rate even further.

Chapter 7 demonstrated the effects of modifying basic film properties on seeded grain growth, specifically in relatively higher deposition-rate parameter spaces. Since crystallization in traditional, unseeded, amorphous films is a result of both the nucleation and growth of native grains, the effects of film properties on the growth rate, alone, of individual grains is relatively un-documented. Seeded films grown from the dual plasma reactor described in this work allow for a fixed number of growth sites to be studied under variable film conditions. It was subsequently demonstrated that film parameters commonly associated with relatively higher deposition rates were seen to enhance the growth rate of individual grains. Furthermore, an optimal processing window was identified for producing potentially through-thickness grains of micron-scale thickness, under relatively higher deposition rates.

8.2 Future Work and Recommendations

Seeded films grown from the outlined dual-plasma technique exhibit potential for high-performing solar cell absorber layers, with low thermal budget requirements relative to similar, currently implemented standards. The layer-by-layer approach is amenable to through-thickness grain structures, optimal for solar cell abosrber layers. However the studies outlined here provide a basic proof of concept. Now that a processing window has been identified for deposition of potentially useful, thicker grain structures, more extensive characterization of such thicker films is required. Specifically, the complete crystallization of μm-thick films by a single mono-layer of seed crystals should be demonstrated. The electronic transport properties associated with grain quality in the thickness dimension must also be characterized. Specifically, transverse contact scheme must be implemented in characterization, similar to the device structures implemented in photo-voltaic junctions. This requires successfully annealing films on a conductive substrate. Glass substrates coated in aluminum doped zinc-oxide are a viable candidate due to high temperature stability and electrical properties. Furthermore, since solar cells consist of doped “p-i-n” diode structures, the effects of dopant impurity concentration on crystallization kinetics present entirely new parameter spaces of importance as well.

References

[1] International Energy Outlook. `http://www.eia.gov/oiaf/ieo/index.html`. United States Depatrment of Energy, Washington GPO, 2010.

[2] Worldwide Energy Demand Set to Rise. `http://energybusinessdaily.com/renewables/worldwide-energy-demand-set-to-rise/`. August, 2010.

[3] B.P. Nelson. The Potential of Photovoltaics: introduction and basics. *Vacuum Technology and Coating*, April, 2009.

[4] Renewable Energy Consumption and Electricity Preliminary Statistics 2008. `http://www.eia.doe.gov/cneaf/alternate/page/renew_energy_consump/rea_prereport.html`. United States Depatrment of Energy, Washington GPO, 2009.

[5] H.S. Ullal and V.B. Rodern. Thin Film CIGS and CdTe Photovoltaic Technologies: commercialization, critical issues, and applications. *The Proceedings of the 22nd PVSEC*, 2007.

[6] Yingli Gains Crown as Top Producer in a 36GW Global PV Market. `http://www.greentechmedia.com/articles/read`. GreenTech Media Research, May, 2013.

[7] K. Emery and A. Luque. *Handbook of Photovoltaic Science and Engineering, 2nd edition.* Wiley, Chichester, West Sussex, United Kingdom, 2011.

[8] Semiconductor Physics. `http://www.tf.uni-kiel.de/matwis/amat/semi_en/index.html`. hyperscript last modified: 2004.

[9] P.M. Martin. Thin Film Photovoltaic Basics II. *Vacuum Technology and Coating*, October, 2006.

[10] C.R. Wronski, B. Von Roedern, and A. Kolodziej. Thin-film Si:H-based solar cells. *Vacuum*, 82(10):1145–1150, June 2008.

[11] O. Vetterl, F. Finger, R. Carius, P. Hapke, L. Houben, O. Kluth, A. Lambertz, A. Mu, B. Rech, and H. Wagner. Intrinsic microcrystalline silicon : A new material for photovoltaics. *Solar Energy Materials and Solar Cells*, 62:97–108, 2000.

[12] R. Buitrago, G. Risso, M. Cutrera, M. Battioni, L. Debernardez, J. Schmidt, R. Arce, and R. Koropecki. Polycrystalline silicon thin film solar cells prepared by PECVD-SPC. *International Journal of Hydrogen Energy*, 33(13):3522–3525, July 2008.

[13] Thin Film Solar Technology Market Shares, Strategies, and Forecasts, Worldwide, 2011 to 2017. `http://www.wintergreenresearch.com/reports/thin%20film%20solar%202011%20press%20release.pdf`. press realease Sept., 2011.

[14] B. Roedern, H. Ullal, and K. Zweibel. Polycrystalline Thin-Film Photovoltaics: From the Laboratory to Solar Fields. *2006 IEEE 4th World Conference on Photovoltaic Energy Conference*, pages 384–387, 2006.

[15] CIGS Thin-Film Manufacturing Players and Cost Models. `http://www.greentechmedia.com/research/report/the-greentech-innovations-report-1/`. GreenTech Media Research, February 2009.

[16] V. Fthenakis. Sustainability of photovoltaics: The case for thin-film solar cells. *Renewable and Sustainable Energy Reviews*, 13(9):2746–2750, December 2009.

[17] H.F. Sterling and R.C.G. Swann. Chemical vapour deposition promoted by r.f. discharge. *Solid-State Electronics*, 8:653–654, 1965.

[18] W.E. Spear and P.G. Lecomber. Substitutional doping of amorphous silicon. *Journal of Non-crystalline Solids*, 17:1193–1196, 1975.

[19] W.E. Spear and P.G Lecomber. Electronic properties of substitutionally doped amorphous Si and Ge. *Journal of Non-crystalline Solids*, 33:935–949, 1976.

[20] H. Mahan, S.P. Ahrenkiel, R.E.I. Schropp, H. Li, and D.S. Ginley. A comparison of grain nucleation and grain growth during crystallization of HWCVD and PECVD a-Si:H films. *Thin Solid Films*, 516(5):529–532, January 2008.

[21] H. Mahan, T. Su, D. L. Williamson, L. M. Gedvilas, S. P. Ahrenkiel, P. Parilla, Y. Xu, and D. Ginley. Identification of nucleation center sites in thermally annealed hydrogenated amorphous silicon. *Advanced Functional Materials*, 19(14):2338–2344, July 2009.

[22] F. Liu, M. J. Romero, K. M. Jones, M. M. Al-Jassim, O. Kunz, J. Wong, and A.G. Aberle. Solid-phase crystallization of evaporated silicon thin films on glass for photovoltaics: A combined SEM and TEM study. *SPIE proceedings*, 7409:740906–740906–8, August 2009.

[23] C. Becker, E. Conrad, P. Dogan, F. Fenske, B. Gorka, T. Hänel, K.Y. Lee, B. Rau, F. Ruske, and T. Weber. Solid-phase crystallization of amorphous silicon on ZnO:Al for thin-film solar cells. *Solar Energy Materials and Solar Cells*, 93(6-7):855–858, June 2009.

[24] T. Sontheimer, C. Becker, S. Gall, and B. Rech. Crystal nucleation in electron-beam evaporated amorphous silicon on aluminum doped zinc oxide and silicon nitride coated glass for thin film solar cells. *Physica Status Solidi (C)*, 528(3):525–528, February 2010.

[25] R.E.I. Schropp and M. Zema. *Amorphous and Microcrystalline Silicon Solar Cells: modeling, materials and device technology.* Kluwer Academic Publishing, Norwell, Massachusettes, 1998.

[26] J. Poortmans and V. Arkhipov. *Thin Film Solar Cells: fabrication, characterization, and applications.* Wiley, Chichester, West Sussex, United Kingdom, 2006.

[27] K. Bhattacharya and D. Das. Effect of deposition temperature on the growth of nanocrystalline silicon network from helium diluted silane plasma. *Journal of Physics D: Applied Physics*, 41(15):155420, August 2008.

[28] D. Gracin, B. Etlinger, K. Juraić, A. Gajović, P. Dubček, and S. Bernstorff. The DC conductivity and structural ordering of thin silicon films at the amorphous to nano-crystalline phase transition. *Vacuum*, 82(2):205–208, October 2007.

[29] D. L. Staebler and C. R. Wronski. Reversible conductivity changes in discharge-produced amorphous Si. *Applied Physics Letters*, 31(4):292, 1977.

[30] A Kolodziej. Staebler-Wronski effect in amorphous silicon and its alloys. *Opto-electronics review*, 12(1):21–32, 2004.

[31] P. Roca i Cabarrocas, Y. Djeridane, T. Nguyen-Tran, E. V. Johnson, A. Abramov, and Q. Zhang. Low temperature plasma synthesis of silicon nanocrystals: a strategy for high deposition rate and efficient polymorphous and microcrystalline solar cells. *Plasma Physics and Controlled Fusion*, 50(12):124037, December 2008.

[32] M. Fontcuberta and P. Roca i Cabarrocas. Shedding light on the growth of amorphous, polymorphous, protocrystalline and microcrystalline silicon thin films. *Thin Solid Films*, 383(1-2):161–164, February 2001.

[33] Y. Adjallah, C. Anderson, U. Kortshagen, and J. Kakalios. Structural and electronic properties of dual plasma codeposited mixed-phase amorphous/nanocrystalline thin films. *Journal of Applied Physics*, 107(4):043704, 2010.

[34] V. G. Golubev, V. Y. Davydov, V. Medvedev, B. Pevtsov, and N. Feoktistov. Raman scattering spectra and electrical conductivity of thin silicon films with a mixed amorphous-nanocrystalline phase composition: Determination of the nanocrystalline volume fraction. *Physics of the Solid State*, 39(8):1197–1201, August 1997.

[35] X. Liao, W. Du, X. Yang, H. Povolny, X. Xiang, X. Deng, and K. Sun. Nanostructure in the p-layer and its impacts on amorphous silicon solar cells. *Journal of Non-Crystalline Solids*, 352(9-20):1841–1846, June 2006.

[36] S. K. Ram, K. Satyendra, and P. Roca i Cabarrocas. Influence of fractional composition of crystallite grains on the dark conductivity in fully crystallized undoped microcrystalline silicon. *condensed matter*, pages 1–4, 2007.

[37] U.K. Das, P. Chaudhuri, and S.T. Kshirsagar. Effect of argon dilution on the structure of microcrystalline silicon deposited from silane. *Journal of Applied Physics*, 80(November):5389–5397, 1996.

[38] L. Li, Y.M. Li, J.A. Anna Selvan, A.E. Delahoy, and R.A. Levy. Correlations between structural properties and performance of microcrystalline silicon solar cells fabricated by conventional RF-PECVD. *Journal of Non-Crystalline Solids*, 347(1-3):106–113, November 2004.

[39] B. Yan, G. Yue, J. Yang, S. Guha, D. L. Williamson, D. Han, and C.S. Jiang. Hydrogen dilution profiling for hydrogenated microcrystalline silicon solar cells. *Applied Physics Letters*, 85(11):1955, 2004.

[40] A.G. Aberle. Thin-film solar cells. *Thin Solid Films*, 517(17):4706–4710, July 2009.

[41] Microcrystalline Silicon for Solar Cells. `http://www.tue.nl/typo3temp/pics/f5afa92290.png`. Eindhoven University of Technology Plasma and Materials Processing Lab, last updated 2012.

[42] K. Yamamoto. Very thin film crystalline silicon solar cells on glass substrate fabricated at low temperature. *IEEE Transactions on Electron Devices*, 46(10):2041–2047, 1999.

[43] F. Meillaud, A. Feltrin, D. Dominé, P. Buehlmann, M. Python, G. Bugnon, A. Billet, G. Parascandolo, J. Bailat, S. Fay, N. Wyrsch, C. Ballif, and A. Shah. Limiting factors in the fabrication of microcrystalline silicon solar cells and micromorph tandems. *Philosophical Magazine*, 89(28-30):2599–2621, October 2009.

[44] D. Azulay, I. Balberg, V. Chu, J. Conde, and O. Millo. Current routes in hydrogenated microcrystalline silicon. *Physical Review B*, 71(11):113304, March 2005.

[45] R.B. Iverson and R. Reif. Recrystallization of amorphized polycrystalline silicon films on SiO2: temperature dependence of the crystallization parameters. *Journal of Applied Physics*, 62(5):1675–1681, 1987.

[46] C. Spinella, S. Lombardo, and F. Priolo. Crystal grain nucleation in amorphous silicon. *Journal of Applied Physics*, 84(10):5383, 1998.

[47] T. Mohammed-Brahim, K. Kis-Sion, D. Briand, M. Sarret, O. Bonnaud, J.P. Kleider, C. Longeaud, and B. Lambert. From amorphous to polycrystalline thin films: dependence on annealing time of structural and electronic properties. *Journal of Non-Crystalline Solids*, 227-230:962–966, May 1998.

[48] R.B. Bergmann. Crystalline Si thin-film solar cells: a review. *Applied Physics A: Materials Science & Processing*, 69(2):187–194, August 1999.

[49] A.G. Aberle. Progress with polycrystalline silicon thin-film solar cells on glass at UNSW. *Journal of Crystal Growth*, 287(2):386–390, January 2006.

[50] M.A. Green, P.A. Basore, N. Chang, D. Clugston, R. Egan, R. Evans, D. Hogg, S. Jarnason, M. Keevers, P. Lasswell, J. OSullivan, U. Schubert, A. Turner, S.R. Wenham, and T. Young. Crystalline silicon on glass (CSG) thin-film solar cell modules. *Solar Energy*, 77(6):857–863, December 2004.

[51] M.A. Green. Recent developments in photovoltaics. *Solar Energy*, 76(1-3):3–8, January 2004.

[52] G. Harbeke and L. Krausbauer. High quality polysilicon by amorphous low pressure chemical vapor deposition. *Applied Physics Letters*, 42:30249–30251, 1983.

[53] L. Haji, M. Guendouz, N. Duhamel, and B. Loisel. Substrate effects on the kinetics of solid phase crystallization in aSi. *Materials Research Society Symposium Proceedings*, 230:177–182, 1992.

[54] S. Roorda, J.S. Custer, W.C. Sinke, J.M. Poate, D.C. Jacobson, A. Polman, and F. Spaepen. Structural relaxation in amorphous silicon and the role of network defects. *Nuclear Instruments and Methods in Physics Research Section B: Beam Interactions with Materials and Atoms*, 59-60:344–352, July 1991.

[55] M.J. Romero, F. Liu, and O. Kunz. Imaging electron transport across grain boundaries in an integrated electron and atomic force microscopy platform: application to polycrystalline silicon solar cells. *MRS Proceedings*, 1153:3–9, 2009.

[56] J. Wong, J. L. Huang, B. Eggleston, M. A. Green, O. Kunz, R. Evans, M. Keevers, and R. J. Egan. Lifetime limiting recombination pathway in thin-film polycrystalline silicon on glass solar cells. *Journal of Applied Physics*, 107(12):123705, 2010.

[57] N.H. Nickel, W.B. Jackson, and N.M. Johnson. Light-induced creation of metastable paramagnetic defects in hydrogenated polycrystalline silicon. *Physical review letters*, 71(17):2733–2735, 1993.

[58] R. Garcia, M. Estrada, and A. Cerdeira. Effects of impurity concentration, hydrogen plasma process and crystallization temperature on poly-crystalline films from PECVD aSi-:H layers. *microelectronics reliability*, 43:1281–1287, 2003.

[59] R.B Bergmann and J.H Werner. The future of crystalline silicon films on foreign substrates. *Thin Solid Films*, 403-404:162–169, February 2002.

[60] T. Matsuyama, N. Terada, T. Baba, T. Sawada, S. Tsuge, K. Wakisaka, and S. Tsuda. High quality polycrystalline silicon thin film prepared by a solid phase crystallization method. *Journal of Non-Crystalline Solids*, 200:940–944, 1996.

[61] K. Sharma, A. Branca, A. Illiberi, F.D. Tichelaar, M. Creatore, and M.C.M. van de Sanden. On the effect of the amorphous silicon microstructure on the grain size of solid phase rystallized polycrystalline silicon. *Advanced Energy Materials*, 1(3):401–406, May 2011.

[62] C.D. Park, H.Y. Kim, M.H. Cho, K.J. Jan, and J.Y. Lee. Solid-phase crystallization of hydrogenated amorphous silicon/hydrogenated microcrystalline silicon bilayers deposited by plasma-enhanced chemical vapor deposition. *Thin Solid Films*, 359(2):268–274, January 2000.

[63] H.Y. Kim, K.Y. Lee, and J.Y. Lee. The influence of hydrogen dilution ratio on the crystallization of hydrogenated amorphous silicon films prepared by plasma-enhanced chemical vapor deposition. *Thin Solid Films*, 302(1-2):17–24, June 1997.

[64] H.Y. Kim, J.B. Choi, and J.Y. Lee. Effects of silicon hydrogen bond characteristics on the crystallization of hydrogenated amorphous silicon films prepared by plasma

enhanced chemical vapor deposition. *Journal of Vacuum Science & Technology A: Vacuum, Surfaces, and Films*, 17(6):3240, 1999.

[65] N. Budini, P. Rinaldi, J. Schmidt, R.D. Arce, and R.H. Buitrago. Influence of microstructure and hydrogen concentration on amorphous silicon crystallization. *Thin Solid Films*, 518(18):5349–5354, July 2010.

[66] T. Matsuyama, M. Tanaka, and S. Tsuda. Improvement of n type poly Si film properties by solid phase crystallization method. *Japanese Journal of Applied Physics*, 32(9A):3720–3728, 1993.

[67] I.W. Wu, A. Chiang, M. Fuse, L. Ovecoglu, and T.Y. Huang. Retardation of nucleation rate for grain size enhancement by deep silicon ion implantation of low-pressure chemical vapor deposited amorphous silicon films. *Journal of Applied Physics*, 65(10):4036, 1989.

[68] D. Toet and B. Koopmans. Growth of polycrystalline silicon on glass by selective laser induced nucleation. *Applied Physics Letters*, 69:3719–3721, 1996.

[69] N.D. Sinh, G. Andrä, F. Falk, E. Ose, and J. Bergmann. Optimization of layered laser crystallization for thin-film crystalline silicon solar cells. *Solar Energy Materials and Solar Cells*, 74:295–303, 2002.

[70] J.S. Im, M. Chahal, P.C. van der Wilt, U.J. Chung, G.S. Ganot, A.M. Chitu, N. Kobayashi, K. Ohmori, and A.B. Limanov. Mixed phase solidification of thin Si films on silicon dioxide. *Journal of Crystal Growth*, 312(19):2775–2778, September 2010.

[71] Ö. Tüzün, J.M. Auger, I. Gordon, A. Focsa, P.C. Montgomery, C. Maurice, A. Slaoui, G. Beaucarne, and J. Poortmans. EBSD analysis of polysilicon films formed by aluminium induced crystallization of amorphous silicon. *Thin Solid Films*, 516(20):6882–6887, August 2008.

[72] Ö. Tüzün, A. Slaoui, S. Roques, A. Focsa, F. Jomard, and D. Ballutaud. Solid phase epitaxy on n type polysilicon films formed by aluminium induced crystallization of amorphous silicon. *Thin Solid Films*, 517(23):6358–6363, October 2009.

[73] S. Gall, J. Schneider, J. Klein, K. Hübener, M. Muske, B. Rau, E. Conrad, I. Sieber, K. Petter, K. Lips, M. Stöger-Pollach, P. Schattschneider, and W. Fuhs. Large-grained polycrystalline silicon on glass for thin-film solar cells. *Thin Solid Films*, 511-512:7–14, July 2006.

[74] M. Hossain and H.H. Abu-Safe. Effect of stress on the aluminum-induced crystallization of hydrogenated amorphous silicon films. *J. Mater. Res.*, 21(10):2582–2586, 2006.

[75] A. Illiberi, K. Sharma, M. Creatore, and M.C.M. van de Sanden. Novel approach to thin film polycrystalline silicon on glass. *Materials Letters*, 63(21):1817–1819, August 2009.

[76] D.N. Kouvatsos, A.T. Voutsas, and Miltiadis K. Hatalis. Polycrystalline silicon thin film transistors fabricated in various solid phase crystallized films deposited on glass substrates. *Journal of Electronic Materials*, 28(1):19–25, January 1999.

[77] J. R. Heath, S. M. Gates, and C. A. Chess. Nanocrystal seeding: A low temperature route to polycrystalline Si films. *Applied Physics Letters*, 64(26):3569, 1994.

[78] K. Pangal, J. C. Sturm, S. Wagner, and T. H. Buyuklimanli. Hydrogen plasma enhanced crystallization of hydrogenated amorphous silicon films. *Journal of Applied Physics*, 85(3):1900, 1999.

[79] A.T. Voutsas and M.K. Hatalis. Crystallized mixed-phase silicon films for thin film transistors on glass substrates. *Applied Physics Letters*, 63(11):1546–1548, 1993.

[80] T. Kim, P. Kumar, J.S. Lee, K. Siebein, and R.K. Singh. Solid phase crystallization of aSi thin film induced by a novel approach for photovoltaic devices. *ECS Transactions*, 16(6):79–85, 2008.

[81] C.M. Anderson. *Phd thesis.* University of Minnesota, 2008.

[82] S.A. Campbell. *Fabrication Engineering at the Nano and Micro scale.* Oxford, New York, 2008.

[83] M.A. Lieberman and A.J. Lichtenberg. *Principles of Plasma Discharges and Materials Processing.* Wiley, Hoboken, New Jersey, 2nd edition, 2005.

[84] R.A. Street. *Hydrogenated Amorphous Silicon.* Cambridge University Press, New York, 1991.

[85] G.D. Cody. The optical absorption edge of a-Si: H. *Semiconductors and Semimetals*, 21(B):11–79, 1984.

[86] H. M. Smets, W. M. M. Kessels, and M. C. M. van de Sanden. Vacancies and voids in hydrogenated amorphous silicon. *Applied Physics Letters*, 82(10):1547, 2003.

[87] H. M. Smets, W. M. M. Kessels, and M. C. M. van de Sanden. Temperature dependence of the surface roughness evolution during hydrogenated amorphous silicon film growth. *Applied Physics Letters*, 82(6):865, 2003.

[88] H. M. Smets, W. M. M. Kessels, and M. C. M. van de Sanden. Surface-diffusion-controlled incorporation of nanosized voids during hydrogenated amorphous silicon film growth. *Applied Physics Letters*, 86(4):041909, 2005.

[89] E. Bhattacharya and A.H. Mahan. Microstructure and the light-induced metastability in hydrogenated amorphous silicon. *Applied Physics Letters*, 52(19):1587, 1988.

[90] M.H. Brodsky, M. Cardona, and J.J. Cuomo. Infrared and Raman spectra of the silicon-hydrogen bonds in amorphous silicon prepared by glow discharge and sputtering. *Physical Review B*, 16(8):3556–3571, 1977.

[91] A. Langford, M.I. Fleet, B.P. Nelson, W.A. Lanford, and N. Maley. Infrared absorption strength and hydrogen content of hydrogenated amorphous silicon. *Physical review. B, Condensed matter*, 45(23):13367–13377, June 1992.

[92] T. Mohammed-Brahim, D. Briand, K. Kis-Sion, D. Guillet, A.C. Salaun, and O. Bonnaud. Thermal activation of the crystallization kinetics of amoprhous silicon. *Materials Letters*, 398:387–392, 1996.

[93] J. Tauc, A. Abraham, L. Pajasova, R. Grigorovici, and A. Vancu. Optical properties of non-crystalline semiconductors. *proceedings of the Delft conference on physics of non-crystalline solids*, pages 606–615, 1964.

[94] A. Bapat, C.R. Perrey, S.A. Campbell, C. Barry Carter, and U. Kortshagen. Synthesis of highly oriented, single-crystal silicon nanoparticles in a low-pressure, inductively coupled plasma. *Journal of Applied Physics*, 94(3):1969, 2003.

[95] A. Bapat, M. Gatti, Y.P. Ding, S.A. Campbell, and U. Kortshagen. A plasma process for the synthesis of cubic-shaped silicon nanocrystals for nanoelectronic devices. *Journal of Physics D: Applied Physics*, 40(8):2247–2257, April 2007.

[96] U. Kortshagen and U. Bhandarkar. Modeling of particulate coagulation in low pressure plasmas. *Physical review. E, Statistical physics, plasmas, fluids, and related interdisciplinary topics*, 60(1):887–98, July 1999.

[97] U. Kortshagen. Nonthermal plasma synthesis of semiconductor nanocrystals. *Journal of Physics D: Applied Physics*, 42(11):113001, June 2009.

[98] L. Mangolini and U. Kortshagen. Selective nanoparticle heating: Another form of nonequilibrium in dusty plasmas. *Physical Review E*, 79(2):026405, February 2009.

[99] T. Hawa and M. R. Zachariah. Understanding the effect of hydrogen surface passivation and etching on the shape of silicon nanocrystals. *Journal of Physical Chemistry C*, 112(38):14796–14800, September 2008.

[100] A.T. Voutsas, M. K. Hatalis, J. Boyce, and A. Chiang. Raman spectroscopy of amorphous and microcrystalline silicon films deposited by low-pressure chemical vapor deposition. *Journal of Applied Physics*, 78(12):6999, 1995.

[101] R. Tsu. Temperature dependence of silicon Raman lines. *Applied Physics Letters*, 41(11):1016, 1982.

[102] H. Kakinuma, M. Mohri, M. Sakamoto, and T. Tsuruoka. Structural properties of polycrystalline silicon films prepared at low temperature by plasma chemical vapor deposition. *Journal of Applied Physics*, 70(12):7374, 1991.

[103] C. Smit, R.A.C.M.M. van Swaaij, H. Donker, A. M. H. N. Petit, W. M. M. Kessels, and M. C. M. van de Sanden. Determining the material structure of microcrystalline silicon from Raman spectra. *Journal of Applied Physics*, 94(5):3582–3588, 2003.

[104] A. Kolmogorov. A statistical theory for the recrystallization of metals. *Akad. nauk SSSR, Izv., Ser. Matem*, 1(355):335–360, 1937.

[105] W. Anderson and R.H. Mehl. Recrystallization of aluminum in terms of the rate of nucleation and growth. *Trans. AIME*, 161:140–172, 1945.

[106] W. Johnson and R. Mehl. Reaction kinetics in processes of nucleation and growth. *Trans AIME*, 135:416–458, 1939.

[107] M. Avrami. Kinetics of Phase Change I: General theory. *Journal of Chemical Physics*, 7:1103–1112, 1939.

[108] M. Avrami. Kinetics of Phase Change II: Transformations and time relations for random distribution of nuclei. *Journal of Chemical Physics*, 8:212–224, 1940.

[109] A.Q. He, A.H. Heuer, and H. Kahn. Homogeneous nucleation during crystallization of amorphous silicon produced by low-pressure chemical vapour deposition. *Philosophical Magazine A*, 82(1):137–165, January 2002.

[110] F.G. Shi. Direct measurement of free-energy barrier to nucleation of crystallites in amorphous silicon thin films. *Journal of Applied Physics*, 76(9):5149, 1994.

[111] C. Spinella, F. Priolo, S. Lombard, S .U. Campisano, and E. Rimini. Ion-assisted crystallization in silicon : epitaxy and grain growth. *Nuclear Instruments and Methods in Physics Research Section B: Beam Interactions with Materials and Atoms*, 60:363–371, 1991.

[112] J.A. Venables, G.D.T. Spiller, and M. Hanbucken. Nucleation and growth of thin films. *Rep. Prog. Phys.*, 47:399–459, 1984.

[113] F. Law, B. Hoex, J. Wang, J. Luther, K. Sharma, M. Creatore, and M.C.M. Van de Sanden. Kinetic study of solid phase crystallisation of expanding thermal plasma deposited a-Si:H. *Thin Solid Films*, 520(17):5820–5825, June 2012.

[114] J. Fortner and J.S. Lannin. Radial distribution functions of amorphous silicon. *Physical Review B*, 39(8):1–4, 1989.

[115] N. Maley and J.S. Lannin. Influence of hydrogen on vibrational and optical properties of aSiH alloys. *Physical Review B*, 36(2):1146–1152, 1987.

[116] H. Shanks, C.J. Fang, and L. Ley. Infrared spectrum and structure of hydrogenated amorphous silicon. *Phys Status Solidi (b)*, 43:43–56, 1980.

[117] K. Sharma, M. V. Ponomarev, M.A. Verheijen, O. Kunz, F.D. Tichelaar, M.C.M. van de Sanden, and M. Creatore. Solid-phase crystallization of ultra high growth rate amorphous silicon films. *Journal of Applied Physics*, 111(10):103510, 2012.

[118] M. Nakamura and T. Ohno. Characterization of hydrogenation and dehydrogenation of post plasma treated low pressure chemical vapor deposition amorphous silicon. *Journal of Applied Physics*, 62(9):3740–3746, 1987.

[119] Z. Iqbal, S. Veprek, A.P. Webb, and P. Capezzuto. Raman scattering from small particle size polycrystalline silicon. *Solid State Communications*, 37(1980):993–996, 1981.

[120] P.G. LeComber, G. Willeke, and W.E. Spear. Some new results on transport and density of state distribution in glow discharge microcrystalline silicon. *Journal of Non-Crystalline Solids*, 60:795–798, 1983.

[121] H.C. Degraaff and M. Huybers. Grain boudary states and characteristics of lateral poly-silicon diodes. *solid-state electronics*, 25(I):67–71, 1982.

[122] G. Baccarani and B. Ricco. Transport properties of polycrystalline silicon films. *Journal of Applied Physics*, 49(11):5565–5570, 1978.

[123] R.J. Bennett and K.A. Thoma. Effect of annealing on the electrical behaviour of chromium contacts to silicon. *International Journal of Electronics*, 67(6):865–868, 1989.

[124] J.P. Smith, W. Eccleston, P.D. Brown, and C.J. Humphreys. Electronic and Structural Properties of Partially Crystallized Silicon Amorphous Silicon. *Journal of The Electrochemical Society*, 146(1):306–312, 1999.

[125] Y. He, Y. Wei, G. Zheng, M. Yu, and M. Liu. An exploratory study of the conduction mechanism of hydrogenated nanocrystalline silicon films. *Journal of Applied Physics*, 82(7):3408, 1997.

[126] J. Tauc. Optical properties of semiconductors. *Proceedings of the International School of Physics*, 34:63–89, 1966.

[127] N Beck, J. Meier, J. Fric, and Z. Remes. Enhanced optical absorption in microcrystalline silicon. *Journal of Non-Crystalline Solids*, 200(1996):903–906, 1996.

[128] N. H. Nickel, A. Yin, and S. J. Fonash. Influence of hydrogen and oxygen plasma treatments on grain-boundary defects in polycrystalline silicon. *Applied Physics Letters*, 65(24):3099–3101, 1994.

[129] N.H. Nickel, W.B. Jackson, and J. Walker. Influence of grain boundaries on hydrogen transport in polycrystalline silicon. *Journal of Non-Crystalline Solids*, 227-230:885–889, May 1998.

[130] K. Nishioka, T. Yagi, Y. Uraoka, and T. Fuyuki. Effect of hydrogen plasma treatment on grain boundaries in polycrystalline silicon solar cell evaluated by laser-beam-induced current. *Solar Energy Materials and Solar Cells*, 91(1):1–5, January 2007.

[131] S.J. Jones, Y. Chen, and D.L. Williamson. The effects of Ar and He dilution of silane plasmas on the microstructure of a-Si: H detected by small-angle X-ray scattering. *Journal of Non-Crystalline Solids*, 166:131–134, 1993.

[132] A. J. Wagner, C. M. Anderson, J. Trask, L. Cui, A. Chov, A. Mkhoyan, and U. R. Kortshagen. Crystallization kinetics of nano-crystallite inclusions in amorphous silicon thin films. *Nano letters*, 13(11):5735–5739, 2013.

[133] C. Spinella, S. Lombardo, and F. Priolo. Crystal grain nucleation in amorphous silicon. *Journal of Applied Physics*, 84(10):5383, 1998.

[134] Y. Hiroyama, R. Suzuki, and Y. Hirano. Raman spectroscopy and positron lifetime studies of structural relaxation and defect evolution in amorphous silicon. *Japanese Journal of Applied Physics*, 34(10):5515–5519, 1995.

[135] C. Godet, N. Layadi, and P. Roca i Cabarrocas. Role of mobile hydrogen in the amorphous silicon recrystallization. *Applied Physics Letters*, 66(February):3146–3148, 1995.

[136] K. Sharma, M.A. Verheijen, M. C. M. van de Sanden, and M. Creatore. Insitu crystallization kinetics studies of plasma-deposited, hydrogenated amorphous silicon layers. *Journal of Applied Physics*, 111(3):033508, 2012.

[137] M. Ohring. *Materials science of thin films: deposition and structure*. Academic Press, London, 2nd edition, 2002.

[138] J. Sée, P. Dollfus, and S. Galdin. Comparison between a sp3 d5 tight-binding and an effective-mass description of silicon quantum dots. *Physical Review B*, 66:193307, 2002.

[139] K. Sasaki and T. Takada. Etching effect of hydrogen plasma on electron cyclotron resonance-chemical vapor deposition and its application to low temperature Si selective epitaxial growth. *Japanese Journal of Applied Physics*, 37(2):402, 1998.

[140] M. Avrami. Kinetics of Phase Change III: Granulation, plots phase change and microstructures. *Journal of Chemical Physics*, 9:177–185, 1941.

[141] C. Becker, F. Ruske, T. Sontheimer, B. Gorka, U. Bloeck, S. Gall, and B. Rech. Microstructure and photovoltaic performance of polycrystalline silicon thin films on temperature-stable ZnO:Al layers. *Journal of Applied Physics*, 106(8):084506, 2009.

[142] J. Robertson. Growth mechanism of hydrogenated amorphous silicon. *Journal of Non-Crystalline Solids*, 266-269:79–83, May 2000.

[143] R. B. Wehrspohn, S. C. Deane, I. D. French, I. Gale, J. Hewett, M. J. Powell, and J. Robertson. Relative importance of the silicon silicon bond and silicon hydrogen bond for the stability of amorphous silicon thin film transistors. *Journal of Applied Physics*, 87(1):144, 2000.

[144] G. Bruno, P. Capezzuto, and A. Madan. *Plasma deposition of amorphous silicon-based materials*. Academic Press, San Diego, California, 1995.

[145] J. Robertson. Growth mechanism of hydrogenated amorphous silicon. *Journal of Non-Crystalline Solids*, 266-269:79–83, May 2000.

[146] J.L. Andujar, E. Bertran, A. Canillas, C. Roeh, and J.L. Morenza. Influence of pressure and radio frequency power on deposition rate and structural properties of hydrogenated amorphous silicon thin films prepared by plasma deposition. *Journal of Vacuum Science & Technology A: Vacuum, Surfaces, and Films*, 9(4):2216–2221, 1991.

[147] J.L. Andujar, J. Kasaneva, and J. Serra. Effects of rf power on optical and electrical properties of plasma-deposited hydrogenated amorphous silicon thin films. *Sensors and Actuators A*, 38:733–736, 1993.

[148] J. E. Potts. Effects of rf power and reactant gas pressure on plasma deposited amorphous hydrogenated silicon. *Journal of Applied Physics*, 52(11):6665, 1981.

[149] O. Saadane, S. Lebib, A. V. Kharchenko, C. Longeaud, and P.R. Cabarrocas. Structural, optical, and electronic properties of hydrogenated polymorphous silicon films deposited from silane hydrogen and silane helium mixtures. *Journal of Applied Physics*, 93(11):9371, 2003.

[150] H. Vach. How much hydrogen and voids are energetically stable in silicon thin films? *MRS Proceedings*, 813:61–65, 2004.

[151] S. Sriraman, S. Agarwal, and E.S. Aydil. Mechanism of hydrogen-induced crystallization of amorphous silicon. *Nature*, 418(July):62–65, 2002.

[152] S. Wagner, S.H. Wolff, and J.M. Gibson. The role of hydrogen in silicon microcrystallization. *MRS Proceedings*, 164, 1989.

[153] H. Mahan, T. Su, D.L. Williamson, L.M. Gedvilas, S. P. Ahrenkiel, P. Parilla, Y. Xu, and D. Ginley. Identification of Nucleation Center Sites in Thermally Annealed Hydrogenated Amorphous Silicon. *Advanced Functional Materials*, 19(14):2338–2344, July 2009.

[154] O. Kunz and Z. Ouyang. 5% Efficient evaporated solid phase crystallised polycrystalline silicon thin film solar cells. *Progress in photovolt: Res. Appl.*, 17:567–573, 2009.

[155] T. N. Nguyen, V. D. Nguyen, S. Jung, and J. Yi. Raman scattering analysis of the residual stress in metal-induced crystallized amorphous silicon thin films using nickel. *Applied Surface Science*, 255(19):8252–8256, July 2009.

[156] I. Brazil and M.A. Green. Measuring strain changes during production of thin film crystalline silicon on glass photovoltaic modules. *Journal of Materials Science: Materials in Electronics*, 21(11):1207–1212, December 2009.

[157] A. Illiberi, K. Sharma, M. Creatore, and M.C.M. van de Sanden. Novel approach to thin film polycrystalline silicon on glass. *Materials Letters*, 63(21):1817–1819, August 2009.

[158] J. Park, S. Kwon, S. Jun, I. N. Ivanov, J. Cao, J. L. Musfeldt, and P. D. Rack. Stress induced crystallization of hydrogenated amorphous silicon. *Thin Solid Films*, 517(11):3222–3226, April 2009.

[159] S. Gall, C. Becker, K.Y. Lee, T. Sontheimer, and B. Rech. Growth of polycrystalline silicon on glass for thin-film solar cells. *Journal of Crystal Growth*, 312(8):1277–1281, April 2010.